

# THE ADIABATIC AND NON-ADIABATIC BEHAVIOR OF A PARTICLE IN OPTICAL LATTICES

A DISSERTATION SUBMITTED TO  
THE GRADUATE SCHOOL OF ENGINEERING AND SCIENCE  
OF BILKENT UNIVERSITY  
IN PARTIAL FULFILLMENT OF THE REQUIREMENTS FOR  
THE DEGREE OF  
DOCTOR OF PHILOSOPHY  
IN  
DEPARTMENT OF PHYSICS

By  
Firat Yilmaz  
June 2018

THE ADIABATIC AND NON-ADIABATIC BEHAVIOR OF A  
PARTICLE IN OPTICAL LATTICES

By Fırat Yılmaz

June 2018

We certify that we have read this dissertation and that in our opinion it is fully adequate, in scope and in quality, as a dissertation for the degree of Doctor of Philosophy.

---

Mehmet Özgür Oktel(Advisor)

---

Mehmet Emre Taşgın

---

Azer Kerimov

---

Rıfat Onur Umucalılar

---

Ceyhun Bulutay

Approved for the Graduate School of Engineering and Science:

---

Ezhan Kardeşan  
Director of the Graduate School

# ABSTRACT

## THE ADIABATIC AND NON-ADIABATIC BEHAVIOR OF A PARTICLE IN OPTICAL LATTICES

Fırat Yılmaz

Ph.D. in Department of Physics

Advisor: Mehmet Özgür Oktel

June 2018

The cold atom experiments provide a clean and controlled environment for realizing many body systems. Recent realizations of artificial gauge fields and adjustable optical lattices paved the way for the study of effectively charged particles with neutral atoms in various lattice and continuum systems. Moreover, it is possible to precisely control the external system parameters, i.e. the artificial gauge fields much faster or slower than the time scales associated with atomic motion in the lattice. It still needs further analysis to fully understand how the adiabatic and non-adiabatic changes affect the stationary and dynamical behavior of the system.

We first investigate the effect of the adiabatic changes in the artificial gauge fields, and focus on the famous problem: A charged particle in a periodic potential under magnetic field. This simple system leads a complicated and involved self-similar energy spectrum, the Hofstadter butterfly. The whole structure of this energy spectrum is determined by the lattice geometry as well as the external field. In this regard, we consider all possible Bravais lattices in two dimensions and investigate the structure of the Hofstadter butterfly as the different point symmetry groups of the lattices are adiabatically deformed from one into another. We find that each 2D Bravais lattice is uniquely mapped to a fractal energy spectrum and it is possible to understand the interplay between the point symmetry groups and the energy spectrum. This beautiful spectrum, in addition, consists of infinitely many topologically distinct regions as a function of magnetic flux and gap number. The topological character of energy bands are determined through their Chern numbers. We calculate the Chern numbers of the major gaps and Chern number transfer between bands during the topological transitions.

In the second part, we investigate the dramatic effect of the non-adiabatic changes in the artificial gauge fields. In a synthetic lattice, the precise control over the hopping matrix elements makes it possible to change this artificial magnetic

field non-adiabatically even in the quench limit. We consider such a magnetic-flux quench scenario in synthetic dimensions. Sudden changes have not been considered for real magnetic fields as such changes in a conducting system would result in large induced currents. Hence we first study the difference between a time varying real magnetic field and an artificial magnetic field using a minimal six-site model which leads to gauge dependent results. This model proves the relation between the gauge dependant dynamics and the absence of scalar potential terms connecting different gauge potentials. In this context, we secondly search for clear indication of the gauge dependent dynamics through magnetic flux quenches of wave packets in two- and three-leg synthetic ladders. We show that the choice of gauge potentials have tremendous effect on the post-quench dynamics of wave packets. Even trivially distinct two vector potentials by an additive constant can produce observable effects, we investigate the effects on the Landau levels and the Laughlin wave function for a filling factor  $\nu = 1/q$ . We also show that edge solutions in a wide synthetic ladder are protected under a flux quench only if there is another edge state solution in the quenched Hamiltonian.

*Keywords:* optical lattice, gauge fields, gauge dependent, dynamics, Hofstadter, butterfly, artificial, synthetic lattice, ladder, magnetic flux, quench, Chern number, transfer, topological transition, cold atoms, Bravais lattices.

## ÖZET

# OPTİK ÖRGÜLERDE PARÇACIĞIN ADİYABATİK VE ADİYABATİK OLMAYAN DAVRANIŞI

Fırat Yılmaz

Fizik Bölümü, Doktora

Tez Danışmanı: Mehmet Özgür Oktel

Haziran 2018

Soğuk atomlar çok parçacıklı sistemlerin gerçekleştirilmesi için temiz ve kontrolü yüksek bir alan sağlar. Son dönemdeki yapay ayar alanlarının ve optik ağ örgülerinin de bu sistemlerde uygulanabilmesi, nötr atomlarla örgü sistemlerinde ve sürekli sistemlerde etkin yüklü parçacıkların çalışmasına öncülük etti. Buna ek olarak, yapay ayar alanları gibi sistem dış parametrelerinin hassas olarak, atomun ağ yapılarında tipik hareket zaman aralığından çok daha hızlı şekilde kontrol edilebilmesi mümkün oldu. Kastedilen sistemler bu nedenle, adiyabatik ve adiyabatik olmayan Hamiltonyan parametreleri altında daha detaylı incelenmeyi gerektirmektedir.

Bu düşünceyle ilk olarak yapay ayar alanlarındaki ayar alanlarının ve optik örgünün adiyabatik değişimini inceledik. Bu ünlü problem ağ yapılarındaki yüklü parçacığın düzgün manyetik alanlar altındaki davranışı olarak bilinmektedir. Bu görece basit sistem Hofstadter kelebeği adında kendiner ve karmaşık bir enerji dağılımı vermektedir ve bu yapının tamamı optik örgünün geometrisi ve dış alan etkisine bağlı olarak değişir. Buradan hareketle, iki boyutlu sistemlerdeki nokta simetrilerin adiyabatik olarak birbiri arasında şekil değiştirilmesiyle Hofstadter kelebeğinin yapısının nasıl değiştiğini araştırdık. Her iki boyutlu Bravais örgüsünün yekpare bir Hofstadter kelebeğine karşılık geldiğini ve nokta simetri gruplarıyla bu enerji diyagramları arasındaki ilişkinin anlaşılabilirliğini gösterdik. Bu enerji diyagramı, bunlara ek olarak, enerji boşluklarının ve manteyik akının fonksiyonları olarak, topolojik olarak birbirinden ayrı sonsuz sayıda bölgeden oluşmaktadır. Biz de ana enerji boşluklarının Chern sayılarını hesapladık ve adiyabatik geçişlerdeki Chern sayısı transferlerini inceledik. Bu Chern sayısı transferiyle oluşan topolojik geçişlerin ancak manyetik akının rasyonel değerlerinde hesaplanabileceğini ve bu Chern sayısının manyetik akı değerinin payda değeriyle gerçekleştiğini, gözledik.

İkinci bölümde, yapay ayar alanlarının adiyabatik olmayan değişimler altındaki

büyük etkilerini inceledik. Sentetik örgülerde ani deęişim limitinde(quench limit), zıplama matris elemanlarının hassas kontrol kabiliyeti, yapay ayar alanlarının adiyabatik olmayan hızlarda deęiştirilmesine olanak vermektedir, bu sebeple öngörülerimizi gözlemlememizde bizlere yüksek potansiyelli bir deney alanı sunmaktadır. Bu niyetle, biz manyetik akı ani deęişim senaryolarını senyetik boyutlarda inceledik. Buna benzer ani deęişimler, gerçek manyetik alanlı sistemlerde denenmiyordu, çünkü bu sistemi kurmak için kullanılan iletken bölümde yüksek mertebede indüklenmiş akımlar oluşturuyordu ve bu da sistemi ısıtıp  $nK$  seviyesinde hazırlanmış sistemlerin yapısını bozuyordu. Buradan hareketle biz ilk olarak zamanla deęişen gerçek manyetik alanlı sistem ile yapay manyetik alanlı sistemi; sade, altı bölmeli bir ağda karşılaştırmalı olarak çalıştık. Bu çalışma bizlere, yapay ağ alanlarındaki deneylerin ayar alanı seçimine baęlı sonuçlar verdiğini gösterdi. Ayrıca çalıştığımız sade model açıkça ayar baęlılığı-indüklenmiş skaler potansiyel terimlerin eksikliği arasındaki temel baęlantıyı gösterdi. Sonrasında, bu ayar seçimine baęlı dinamik sistemleri iki ve üç bacaklı yapay alanlarda dalga paket dinamiklerini manyetik akı ani deęişim dinamikleriyle inceledik ve ayar seçiminin paket dinamiğinde belirleyici etkiye sahip olduğunu bulduk. Ayar alanlarındaki (sabit ekleyip çıkarmak gibi) en basit farklılıklar bile gözlemlenebilir etkiler ürettiğini gözledik ve bu etkilerin sonuçlarını ağ gövde(bulk) fonksiyonlarında (Landau seviyelerinde) ve çok parçacıklı Laughlin dalga fonksiyonlarının  $\nu = 1/q$  doluluk faktörlerinde inceledik. Ayrıca, geniş bacaklı sistemlerde topolojik olarak koruma altındaki kenar çözümlerinin ancak ani-deęişime uğrayan Hamiltonyenin son halinde kenar çözümleri varsa hayatta kalıp gövdeye dağılmadığını keşfettik.

*Anahtar sözcükler:* yapay ayar alanları,optik örgüler, ani deęişim, soęuk atomlar, manyetik akı, Chern sayısı,Hofstadter, ayar dinamięi,ayara baęlılık.

## Acknowledgement

I acknowledge that people of the Republic of Turkey, whose taxes and generosity are valuable and the only source of the scientific activities in fundamental sciences in Turkey. The limited chance to acquire a world class education in the Middle East has increased the responsibilities of intellectuals not only in the scientific contributions but in the development of spreading critical thinking within the enlarged circles of various communities. Therefore, the long-term goal of limited intellectuals had better find several ways to make contributions in these ways.

I am thankful to my parents, Elif and Selahattin for their years of patient struggle and wait for my 'final' graduation which is postponed to the third degree. The independent environment in all aspects of life is totally prepared my brothers and me as conscious individuals. I thank my two brothers, Suat and Burak for their companionship as close friends.

My high school, undergraduate and graduate friends Dođuş Ural, Nisan Sarıaslan, Erdem Karagül, Cüneyt Yılmaz, Tarık Temiz, Alper Yođurt, Efe Onaran, Alper Özgürlük, Cem Emre Akbaş, Kemal Göğebakan, İsmail Can Ođuz, Enes Aybar, Akif Keskiner, Kübra Işık and Altuđ Baykal have help me to discover the existence of the rest of the life other than the fundamental sciences and primed thoughts. Especially, I am grateful to Adeel Shaharyar and his intellectual circle with whom we together developed our worldview.

I am personally in great depth and respect to my supervisor, Mehmet Özgür Oktel, who has devoted his life for the development of the new solid generation of physicists in Turkey. I also acknowledge great services of Ceyhun Bulutay and Tuđrul Hakioglu, they are my role models by their scientific and educational contributions.

As the new stage of my life, I am in great depth for my life-partner Tomris and dog Yoldaş. I love them and I am a lucky person to have them in my life during the desperate times to stay as a conscious and responsible individual for Middle-Eastern playground for the clash of power.

I also acknowledge the 'unprecedented' support of TÜBİTAK during my PhD studies. Without their invaluable efforts, I would not have successfully completed my thesis in such small amount of time.

Eppur si muove!

# Contents

|          |  |           |
|----------|--|-----------|
| <b>1</b> | <b>Introduction</b>  | <b>1</b>  |
| <b>2</b> | <b>Adiabatic and Non-Adiabatic Dynamics</b>  | <b>3</b>  |
| <b>3</b> | <b>Adiabatic Change in Lattice Geometry</b>  | <b>7</b>  |
| 3.1      | The Model . . . . .  | 13        |
| 3.2      | Calculation of the Energy Spectrum . . . . .   | 21        |
| 3.3      | Transitions between Bravais Lattices . . . . .                                       | 24        |
| 3.4      | Topological Characterization of the Bravais Lattice Phase Space . . . . .            | 32        |
| <b>4</b> | <b>Non-Adiabatic Change in Magnetic Flux</b>   | <b>37</b> |
| 4.1      | A minimal model . . . . .  | 40        |
| 4.2      | Two-Leg and Three-Leg Ladders . . . . .  | 46        |
| 4.3      | Wide ladders and the robustness of the edge states . . . . .                         | 59        |
| <b>5</b> | <b>Artificial Magnetic Flux Quench of the Laughlin State</b>                         | <b>69</b> |
| <b>6</b> | <b>Conclusion</b>  | <b>74</b> |
| 6.1      | Outlook . . . . .  | 78        |
| 6.2      | Self-Evaluation . . . . .  | 80        |
| <b>A</b> | <b>Numerical Schrödinger Equation for an Arbitrary Lattice</b>                       | <b>88</b> |
| <b>B</b> | <b>Calculation of the Wannier Functions and the Tight Binding Hopping Parameters</b> | <b>92</b> |
| <b>C</b> | <b>Calculation of General Peierls Hopping Phase</b>                                  | <b>97</b> |

**D N-Leg Ladder Packet Splitting After A Flux Quench**

# List of Figures

|     |   |    |
|-----|---|----|
| 3.1 | All 2D Bravais lattices can be generated by the spatial potential proposed in Eq.3.3. Starting from the left, there are five Bravais lattices, oblique, centered-rectangular(rhombic), triangular, rectangular, square lattices. The lattice depths are chosen as $V_x = V_y = 50$ (units of $E_R$ ) such that the tight binding limit is guaranteed, where $E_R = \hbar^2/2m\lambda_1^2$ is the recoil energy. The thick black lines show the primitive vectors of the Bravais lattice. The unit cell is enclosed with thick solid lines. . . . .  | 9  |
| 3.2 | The tight-binding model for the arbitrary potential. It must have at least eight neighbors shown on the blue contour plot of the spatial potential to capture all possible transitions. Two arrows show the primitive lattice vectors, and the transparent thick lines represent the tight binding hopping parameters, $t_0, t_1, t_2$ and $t_3$ . Note that the symmetric hoppings are found to have same hopping amplitude. . . . .   | 11 |
| 3.3 | The parameter space of all 2D Bravais lattices, shown as a function of the angle between the primitive vectors $\theta$ and the ratio of the lattice constants $\frac{ \vec{a}_2 }{ \vec{a}_1 }$ . As the number of simultaneous symmetries increase, lattices of high symmetry are shown by lines and points, there is a dimensional reduction. The triangular lattice and the square lattice are shown with yellow (T) and green (S) points. The rectangular lattice is denoted with blue (S to B, dashed) line and the centered rectangular lattice is denoted with two purple (T to C and T to S, thick solid) lines. . . . . | 17 |

3.4 The energy dispersion relation in Eq.3.8 is plotted for the square and triangular lattices. All possible energy bands of the 2D Bravais lattices projected onto the lowest band can be described by this function. In our two plots, the lattice parameters are,  $t_0 = t_1 = 1, t_2 = t_3 = 0.035$  for the square lattice,  $t_0 = t_1 = t_2 = 1, t_3 = 0.0$  for the triangular lattice. . . . . 19

3.5 The energy spectrum evolves from the triangle lattice to the square lattice. The spectrum is shown with four representative points of  $\theta$ , as shown in  $a, b, c, d$ . The transition between the lattice geometries is non-trivial. One of the major energy gaps of the square lattice butterfly disappears along the triangular lattice transition. This closing procedure is achieved by infinitely many closures and reopenings of the smaller gaps. The results for this special case is in agreement with those in [1], and additionally show that in a spatial realistic potential, the square to triangular lattice transition qualitatively takes place near the triangular lattice limit,  $\theta \approx 62$  degrees. It means that the major energy gap disappears around  $\theta \approx 62$  . . . . . 22

3.6 The hopping parameters during the transition from the triangular to the square lattice are calculated as a function of angle  $\theta$ . For this purpose, the real space potential parameters are  $V_X = V_Y = 20(\text{units of } E_R)$ . The NN hopping parameters,  $t_0, t_1$  follows the same magnitude and decrease down to  $t_2 = 0.43(\text{units of } E_R)$  in the triangular lattice limit due to the increase in the strength of the interference term in Eq.3.3. The NNN hopping,  $t_3$  starts almost from zero and increases up to an order of magnitude smaller amplitude,  $t_3 \approx 0.025$ . . . . . 25

3.7 The energy spectrum of the oblique lattice. The spectrum is plotted for  $\phi = [-1, 1]$  to underline the doubling in the periodicity of energy. It is also clear that the energy is symmetric under  $\phi \rightarrow -\phi$ . Note that this symmetry is followed by the beloved inversion symmetry that all two dimensional Bravais lattices have. . . . . 27

3.8 The energy spectrum in the rectangular lattice limit is compared with the weak interaction limit of one dimensional infinite chains under magnetic flux  $\phi = p/q$ . The dominant energy gaps are calculated from 1D chains perturbatively. First order calculation yields two large and robust energy gaps even in the far rectangular limit which are shown with thick blue curves. Smaller gaps or the whole energy spectrum can be calculated by higher order perturbative corrections. . . . . 28

3.9 Energy spectrum evolution for two scenarios. From the square lattice to the rectangular lattice and from the triangular lattice to the centered rectangular lattice. The first transition is along the straight line along the  $\theta = \pi/2$  line in Fig.3.3. The second transition is along the centered rectangular lattice curve in the same phase diagram. The gaps close as the ratio of the lattice constants increase (see Fig.3.8), and the lowest band splitting gets smaller and smaller. . . . . 29

3.10 In analogy to Bravais lattice phase diagram in Fig.3.3, the Hofstadter butterfly phase diagram in the phase space of two dimensional Bravais lattices. . . . . 31

3.11 The energy band evolution for  $\phi = \frac{1}{3}$  and  $\phi = \frac{1}{5}$  along the closed path  $\overline{ATSBA}$  denoted in Fig.3.3. The Chern numbers of the gaps are shown explicitly. For  $\phi = 1/3$ , there are two topologically disconnected regimes in the Bravais lattice space and characterized by the Chern numbers 1, -1 and 1, 2. For the case of  $\phi = 1/5$ , there are four topologically distinct regimes with the Chern numbers labeled on the evolution graph. . . . . 34

3.12 Two different topological phases in the two dimensional Bravais lattice phase space for the magnetic flux,  $\phi = 1/3$ . All possible lattices are either classified by Chern numbers -1, 1 including the square lattice or with 2, 1 including the triangular lattice. Observe that the triangular lattice topological phase class roughly follows the centered rectangular lattice curve. . . . . 35

- 4.1 The minimal model, made of a six site tight binding lattice as two stacked squares. Two different set of gauge potentials  $\vec{A}_1(\vec{r}, t)$ ,  $\Phi_1(\vec{r}, t)$  and  $\vec{A}_2(\vec{r}, t)$ ,  $\Phi_2(\vec{r}, t)$  yields Hamiltonians in Eq.4.4 and Eq.4.6. The magnetic field modifies the hopping parameters with Peierls phase. The origin is as the left bottom corner. . . . . 42
- 4.2 The total difference in the site densities of two wavefunctions separately evolved with  $H_1$  and  $H_2$  as a function of time. The initial wavefunctions are identical,  $\Psi_j^1(t=0)\Psi_j^2(t=0)$ , where  $j \in 1, \dots, 6$ . The magnetic flux is ramped from  $\phi = 0$  to  $\phi = 1/3$  within the time interval  $0 \leq t \leq \tau$  for two ramping parameters,  $\gamma = \{0.01, 2\}$ . For  $\gamma = 0.01$ , the ramping is almost adiabatic, as a result, the total difference in each site density is less than 0.01%. It is within our numerical accuracy. For  $\gamma = 2$ , the ramping is non-adiabatic and the evolutions of the same initial wavefunction for two Hamiltonians,  $|\psi_1(t)|^2$  and  $|\psi_2(t)|^2$  are distinct as a function of time. . . . . 44
- 4.3 The non-adiabatic time evolutions of an arbitrary initial wavefunction in the minimal model, for  $\gamma = 2$ . Three plots show each site density  $\langle a_i^\dagger a_i \rangle$  for three Hamiltonians,  $H_i$  and  $i \in \{1, 2, 3\}$ . The evolution is carried out during the ramping of the magnetic flux from 0 to 1/3.  $H_1$  (see Eq.4.4) and  $H_3$  (see Eq.4.8) are equivalent with a dynamical gauge transformation, and lead to identical time evolution, as in plot (a) and (c). The second Hamiltonian,  $H_2$  (see Eq.4.6) lacks the on-site scalar potential in artificial magnetic fields of synthetic lattice. Therefore, site densities are clearly different from the two other cases, as shown in (b). . . . . 46
- 4.4 The two-leg ladder tight binding model illustration for Hamiltonians with two gauge potentials as in Eq.4.10 and Eq.4.17. . . . . 47

4.5 The post-quench dynamics of the initial wavepacket for the two gauge choices in Eq.4.3 and Eq.4.5 for  $\gamma \rightarrow \infty$ . The initial packet is prepared under zero magnetic flux at the lattice momentum  $k = 0.2\pi$ . The artificial magnetic flux is quenched as  $\phi = 0 \rightarrow 1/3$ . The upper plot shows the gauge in Eq.4.5, the initial wavepacket is divided into two packets moving in opposite directions, while in the gauge of Eq.4.3, in the lower plot, the initial wavepacket splits into four packets with different velocities. Note that the blue dashed curves are the pre-quench bands on the left and the initial wavepacket on the right. Similarly, the red curves are the post-quench bands on the left and the red filled curves are the final distribution of the wavefunction long after the quench. Lastly, the distribution of the initial and the final packets are sequentially shown with blue (dark grey) and red (grey) filled circles on the corresponding energy bands on the left lower and upper plots. . . . . 50

4.6 The weight of each packet after a quench between two arbitrary magnetic fluxes,  $\phi_1$  and  $\phi_2$ , see Eq.4.15. The initial packet is prepared around the lattice momentum  $k = \pi/2$  of the lowest band. The left plot shows the weight remaining in the first band,  $|C_{11}(k = \pi/2)|^2$  as a function of  $\phi_1$  and  $\phi_2$ . The right plot is the weight transferred to the upper band after the quench,  $|C_{12}(k = \pi/2)|^2$ . . . . . 51

- 4.7 The pre-quench and the post-quench energy band structures and the packet weights on each band after the quench. Plot *a* and *b* show the pre- ( $\phi = 0$ ) and post-quench ( $\phi = 1/4$ ) energy bands for two gauge choices with dashed blue lines and red solid lines. The plot *c* (*d*) shows the weight of the initial packet in each lattice momentum of the lowest band of zero field Hamiltonian on the new energy bands at  $\phi = 1/4$ . All initial wavepackets are in the lowest bands and the thickness of blue line is same at each  $k$ -point. After the quench, these wavepackets are re-distributed at each  $k$ -point into new bands with different thickness (weight) in the gauge choice 2 (1). Focusing the first gauge choice, (see Eq.4.3), the initial packet prepared within the reduced Brillouin zone at lattice momentum is distributed into nine bands. The connection (see Eq.4.25) between the two Hamiltonians, 4.23 and 4.24 constraints the largest number of packets that initial packets can divide into, which is the square of the number of legs  $3 \times 3 = 9$ . . . . . 55
- 4.8 Time evolution of the wavepacket sample extracted from Fig.4.7 at the lattice momentum  $k = 0.15\pi$ . The initial packet is a zero field Gaussian function which is localized around at  $k = 0.15\pi$ . (a) Flux quench  $\phi = 0 \rightarrow 1/4$  in the first gauge choice creates two packets independent of the denominator of magnetic flux  $q = 4$ , which is against common expectation. The blue and red dots on the left plot show the weights of packets before and after the quench. (b) The same flux quench in the second gauge choice: Creates eight packets with different weights and velocities. The amount of packets are in accordance with our upper limit,  $3 \times 3 = 9$ , as expected. . . . . 57
- 4.9 The time evolution of the density at each leg for the quench  $\phi = 1/2 \rightarrow 0$ . The initial packet is prepared around an eigenstate of  $H_{3L}^{(2)}$  under  $\phi = 1/2$  at  $k_0 = 0.15\pi$  and is quenched to  $H_{3L}^\Theta$  for the gauge angles,  $\Theta = 0$  and  $\Theta = \pi/3$ . The difference in each leg is because of the absence of an induced electric field  $\frac{\Theta}{a}\delta(t)$  needed for the dynamical gauge equivalence. Notice that the total density is same for both gauge angles. . . . . 58

- 4.10 The energy spectrum of the fifteen-leg ladder are shown with 51 points in the momentum space as a function of the magnetic flux,  $\phi$ . The number of lattice site is infinite and the gauge choice is the LAndau gauge parallel to the legs. This spectrum is reminiscent of the Hofstadter butterfly as the density of states are equivalent in the  $n \rightarrow \infty$  ladder limit. In our flux quench scenarios, we take three slice of energy bands at  $\phi = 1/5, 1/3, 5/12$  and create wavepackets at edge state modes. Corresponding edge modes live within the energy gaps. . . . . 61
- 4.11 Time evolution of the edge state packets which are extracted in Fig.4.10 for two different flux quenches. (a)  $\phi = 1/3 \rightarrow 1/5$  (b)  $\phi = 1/3 \rightarrow 5/12$ . The initial packet in both cases are created around the lattice momentum  $k = 0.07\pi$  at the magnetic flux  $\phi = 1/3$  and it is quenched to  $\phi = 1/5$  and  $\phi = 5/12$ . The plots on the left are the energy bands before (blue dashed lines) and after (red solid lines) the quench, and the initial and the final distribution of the packets are denoted on the band diagram with blue and red large dots, respectively. The same initial edge state is observed to survive and decay in two flux values. Two plots on the right are the snapshots of the packets for pre- and post-quench. As clearly seen, the magnetic flux quench for the case  $\phi = 1/3 \rightarrow 1/5$ , results in the survival of the edge state with its 88 percent. The same packet decays into the bulk for the case  $\phi = 1/3 \rightarrow 5/12$  as it is roughly uniformly distributed into all bulk states. . . . . 62
- 4.12 The single particle energy spectrum of a continuous strip under constant magnetic field. The particle is confined to  $0 < x < L = 10$ . There are two types of eigenstates in the system. The degenerate levels are the first type, the bulk Landau levels, and they consist of equally separated plateaus. The second type of eigenstates are the edge states, and their guiding center,  $x_g = k_y$  is our of the strip and consequently the matter waves are squeezed to the edges. The energy of the edge states change as a function of  $k_y$ . . . . . 64

4.13 The dynamical response of the initial edge state wavepacket during the magnetic field quench. The initial packet, in  $x$  direction, is initially prepared as the shifted waveform of the ground state of the guiding center  $k_0 = -2$  and in  $y$ -direction, the form is Gaussian as a superposition of momentum eigenstates localized around the guiding center  $k_0$ . The magnetic field is quenched as  $B = 90 \rightarrow 35$  in units of initial magnetic field  $B_0$ , and  $B_0$  also determines the typical length scale  $\ell_0 = \sqrt{\hbar/eB_0}$  and the energy scale  $E_0 = \hbar e B_0/m$  in the system. We also plot the center-of-mass coordinate as a function of time, the wavepacket clearly indicates the skipping orbits before and after the quench with different quantized radius of orbits. It is worth noting that the edge state in continuum case is always robust unlike its lattice counterpart since the number of available edge states are infinite in this limit. . . . . 67

A.1 Arbitrary unit cell is mapped into a rectangular zone in a curvilinear system. This mapping solves the complication coming from the boundary conditions for different lattice parameters and disconnects the possible contribution from both momentum variables. 91

B.1 Bloch-like density of the ground state of a 4-by-4 finite continuous system defined by the arbitrary optical potential. The form of the energy bands in the infinite lattice limit is not clear in the finite case. However, it is possible to observe that the first  $4 \times 4 = 16$  energy eigenvalues are isolated in the deep lattice limit where  $V_X, V_Y \gg E_R$ . These sixteen energies can be proposed as the representative states of the first band. The left plot shows these sixteen energies. . . . . 93

B.2 The energy eigenvalues of the optical lattice system are plotted as a function of the lattice depths  $V_X = V_Y$ . In the deep lattice limit, the energies are clustered as they would form the energy bands in the infinite lattice limit. Therefore, one can use the isolated energies of the lowest cluster as the approximate Bloch functions of the lowest band. . . . . 94

- B.3 The Wannier functions of the 4-by-4 lattice as the eigenstates of the weighted two dimensional projected operator,  $\hat{O}_n = \hat{x}_n + 0.1\hat{y}_n$ . 95

# List of Tables

# Chapter 1

## Introduction

This thesis investigates the effect of the adiabatic and the non-adiabatic changes in lattice systems. In particular, we first investigate energy spectrum of a single particle in a lattice under constant magnetic field as the lattice geometry is adiabatically changed. We also investigate the effect of a non-adiabatic magnetic flux change on the wavepackets created in the synthetic dimensions. For this purpose, we make a brief introduction to the adiabatic and the non-adiabatic dynamics in a quantum system.

This thesis will be presented in three chapters. In Chapter 2, we give a brief introduction to the adiabatic and the non-adiabatic dynamics. The discussion is kept within the interest of this thesis, more specialized and detailed discussions are considered within the corresponding chapters when they are needed.

In Chapter 3, we focus on the energy spectrum of an electron in a spatially periodic optical lattice under a uniform magnetic field, and consider an adiabatic change of lattice geometry and investigate the energy spectrum and the topological properties. There are five different lattice symmetry groups (Bravais lattices) in two dimensions, and they have distinct self-similar energy spectra as a function of the magnetic field with different topological properties, i.e. Hall conductivity. The adiabatic transitions between these different Bravais lattices

are investigated by examining the changes in the energy spectra and the Hall conductivity throughout the transition. It is found that all the transitions are non-trivial and lead to energy gap closures. Moreover, the transitions are also characterized by topological properties. We calculate the Chern number of energy gaps, and find that the Chern number transfer and consequently the topological phase transfer are inevitable. We then map the Bravais lattice into topological symmetry groups for a few non-trivial values of the magnetic flux, since the zero magnetic field point symmetry groups are no longer useful in categorizing lattices.

In Chapter 4, we investigate the dynamical behavior of wavepackets under non-adiabatic magnetic flux changes. In cold-atom experiments, we make the observation that there is no dynamical Maxwell's relations governing the behavior of neutral atoms because the effect of the magnetic field, the Aharonov-Bohm phase is simulated by various different methods[cite]. A quench scenario in magnetic flux, in this respect, is expected to show a gauge dependent dynamics. Such a sudden change in the magnetic flux is possible in a synthetic dimension experiment, where the simulated magnetic field can be changed much faster than other time scales of the system. We first take a toy model and two gauge choices, which are statically related by a gauge transformation, and show the gauge-dependent dynamics of the initially identical wavefunctions as they are quenched to new two Hamiltonians which are statically connected by a gauge transformation. We then consider the wavepackets in synthetic ladders under the magnetic flux quench, and show that the number of resulting packets after the quench of the initial wavepackets are different and therefore gauge dependent. In the last part, we consider the same flux quenches in a wide ribbon and the continuous strip, and investigate the dynamical behavior of the edge states.

The last chapter concludes the thesis with the findings and what kind of implications they have for the current cold atom experiments.

## Chapter 2

# Adiabatic and Non-Adiabatic Dynamics

In general, the Hamiltonian,  $\hat{H}$  of a close system defines the time evolution of the wavefunction  $\Psi(t)$ , which defines all observable properties,

$$\hat{H}|\Psi(t)\rangle = E|\Psi(t)\rangle. \quad (2.1)$$

Such a system have the energy conservation since the Hamiltonian or the Lagrangian has no explicit time dependence. However, the computational load of solving such an equation where all the effects are introduced as the quantum objects into the equation is heavy. Instead, it is natural to introduce certain parameters into the system with their classical forms or reduce the Hilbert space by excluding them from the equation as the external parameters. Then, this system is called either the effective system or the open system, and the Hamiltonian governing its properties can be explicitly time dependent,

$$\hat{H}(t)|\psi(t)\rangle = i\hbar\frac{\partial}{\partial t}|\psi(t)\rangle. \quad (2.2)$$

Pedagogically, the time dependent Schrödinger equation is taught to have larger class of functions spanning a larger Hilbert space where the time-position separable solutions (in the non-relativistic limit) occupy a smaller volume in this gigantic space. Mathematically speaking, it is true. However, the assumption

with the universe as a closed system tells us a different story. The energy is conserved in the universe, but we instead, greatly reduce the size and the possible interactions for the system such that the resulting Lagrangian and the Hamiltonian become time dependent. In a sense, this result is understandable as follows: The more complicated the system becomes, the more challenging the treatment is, including the time dependence of the effective Hamiltonians.

The time dependent Hamiltonians can be studied in two limiting cases. The first limit is the **adiabatic** limit. The typical time scale of a change in the external parameter is much larger than the typical largest period of the system. The second limit is the **non-adiabatic** limit, where the situation is the opposite. The extreme limit of a non-adiabatic change occurs in an instant and it is called a **quench** in the Hamiltonian.

The **adiabatic theorem** defines the conditions on how an initial state, e.g. the  $n$ th eigenfunction of the initial Hamiltonian  $\hat{H}_i(t_i)$ , by changing the external parameters of the system slow enough; this state is gradually transformed into the  $n$ th eigenstate of the new Hamiltonian  $\hat{H}_f(t_f)$  without crossing the other levels.

Starting from the general time dependent Schrödinger equation as in Eq.2.2, the most general solution for the waveket can be written as[2],

$$|\psi(t)\rangle = \sum_n c_n(t) e^{-i\Theta_n t/\hbar} |\psi_n(t)\rangle, \quad (2.3)$$

The dynamical phase term,  $\Theta_n$  is

$$\Theta_n = -\frac{1}{\hbar} \int_{t_0}^t E_n(t') dt', \quad (2.4)$$

and the eigenkets,  $|\psi_n(t)\rangle$  are the instantaneous eigenstates of the time dependent Hamiltonian,

$$\hat{H}(t) |\psi_n(t)\rangle = E_n(t) |\psi_n(t)\rangle. \quad (2.5)$$

We assume that  $\{|\psi_n(t)\rangle\}$  forms a complete orthonormal basis at each time instant,

$$\begin{aligned} \langle \psi_n(t) | \psi_m(t) \rangle &= \delta_{nm}, \\ \sum_n |\psi_n(t)\rangle \langle \psi_n(t)| &= \hat{I}. \end{aligned} \quad (2.6)$$

It is crucial to understand that  $\{|\psi_n(t)\rangle\}$  in Eq.2.5 are not the time evolved wavefunctions even if the system initially starts with  $n$ th state. Each different time instant accumulates a different phase factor as in Eq.2.4. Plugging the expression in Eq.2.3 back into Eq.2.3 and multiplying from the left by  $\langle\psi_m|$ ,

$$\begin{aligned}\dot{c}_m(t) &= -\sum_n c_n(t)\langle\psi_m(t)|\dot{\psi}_n(t)\rangle, \\ &= -c_m(t)\langle\psi_m(t)|\dot{\psi}_m(t)\rangle - \sum_{n\neq m} c_n(t)\langle\psi_m(t)|\dot{\psi}_n(t)\rangle.\end{aligned}\quad (2.7)$$

Moreover, we need to replace the first term of this equation to get rid of the time derivative on the waveket by taking the partial time derivative of Eq.2.5 and multiplying from the left again by  $\langle\psi_m|$  (we dropped the time variables,  $t$ ),

$$\begin{aligned}\langle\psi_m|\dot{H}|\psi_n\rangle + E_m\langle\psi_m|\dot{\psi}_n\rangle &= \dot{E}_n\langle\psi_m|\psi_n\rangle + E_n\langle\psi_m|\dot{\psi}_n\rangle, \\ \langle\psi_m|\dot{\psi}_n\rangle &= \frac{\langle\psi_m|\dot{H}|\psi_n\rangle}{E_n - E_m}, \quad m \neq n,\end{aligned}\quad (2.8)$$

substituting the second expression in Eq.2.7, it can be further simplified as follows,

$$\dot{c}_m = -c_m\langle\psi_m|\dot{\psi}_m\rangle - \sum_{n\neq m} c_n \frac{\langle\psi_m|\dot{H}|\psi_n\rangle}{E_n - E_m}.\quad (2.9)$$

In the adiabatic approximation[3], we neglect all contributions to  $c_m$  coming from other states, and drop the second summation of the previous equation. The remaining equation decouples each coefficients as,

$$\dot{c}_m(t) = -c_m\langle\psi_m|\dot{\psi}_m\rangle,\quad (2.10)$$

. The solution for the initial conditions  $c_m(0)$  are,

$$c_m(t) = c_m(0)e^{i\gamma_m(t)}.\quad (2.11)$$

The overall phase is called the geometric phase,

$$\gamma_m(t) := i \int_{t_0}^t \langle\psi_m(t')|\frac{\partial}{\partial t'}\psi_m(t')\rangle dt'.\quad (2.12)$$

Recalling the initial assumption, and taking the initial state as  $n$ th eigenstate,  $c_n(0) = 1$  with the initial condition  $c_n(t = 0) = 1$  and  $c_{m\neq n} = 0$ , the wavefunction at time  $t$  is,

$$|\Psi_n(t)\rangle = e^{i\Theta_n(t)}e^{i\gamma_n(t)}|\psi_n(t)\rangle.\quad (2.13)$$

We will come back to the discussion of the geometric phase in Chapter 3.

The **non-adiabatic** change, specifically a quench is defined as a sudden change in a Hamiltonian. An initial state  $|\psi(t_0)\rangle$  is prepared with Hamiltonian  $\hat{H}_0$ , and the governing Hamiltonian at time  $t_0$  is suddenly switched to  $\hat{H}'$ . If the state is prepared in the ground state of the initial single particle or many body Hamiltonian as  $|\psi_0(t_0)\rangle$ , the resulting system is going to have a non-equilibrium dynamics.

$$|\psi(t)\rangle = \hat{U}(t, t_0) |\psi_0(t_0)\rangle = \sum_n c_n(t) |\psi'_n\rangle, \quad \hat{U}(t, t_0) = e^{-i\hat{H}'(t-t_0)/\hbar}, \quad (2.14)$$

where,

$$\hat{H}' |\psi'_n\rangle = E'_n |\psi'_n\rangle. \quad (2.15)$$

The new system is decomposed into the new modes of the quenched Hamiltonian,  $\hat{H}'$ , and makes them evolve each of modes accordingly.

The quench experiments and the non-equilibrium dynamics are crucial to investigate the dynamics of many body states. In cold atom experiments, the initial state is prepared in a trap with a known Hamiltonian, e.g. that of a superfluid or a Mott insulator, and the onset of the interactions, shift in the chemical potential or a sudden change generally in the vicinity of the phase transition allow the investigation of the non-equilibrium dynamics of complicated interactions. Such fast changes in the Hamiltonian, for the cold-atom experiments is our main interest, and it can be achieved by various ways, two of which are a quench or a fast periodic driving one of the Hamiltonian parameters. Quench [4, 5] and Floquet [6, 7, 8] experiments have led to non-trivial phenomena such as many body localization[9, 10], pre-thermalized states[11] and new topological invariants[12].

## Chapter 3

# Adiabatic Change in Lattice Geometry

The Hofstadter butterfly is the fractal energy spectrum for an electron under a uniform magnetic field in a two dimensional crystal[13]. The self-similarity occurs with the indecisive the competition between the lattice constant and the magnetic length scale. It is necessary to understand the properties of this diagram as well as the topological properties to have a complete picture for the underlying physics. In other words, the magnetic field and the lattice geometry determines these properties. The lattice geometry, itself, is determined by the Bravais lattice and each unit cell in this lattice has different basis structure.

After its theoretical discovery, the observation of the fractal spectrum has challenged the physicists for the last forty years. It is because the self-similar spectrum requires a magnetic flux per unit cell on the order of one flux quantum. Let us make a small calculation to estimate the order of required the magnetic field to observe such a spectrum. Magnetic flux  $\Phi = Ba^2$  and the flux quantum  $\phi_0 = \hbar/e \approx 4.1 \times 10^{-15} m^2 kg s^{-1} C^{-1}$ . Assume that  $\Phi \approx \phi_0$ , and a typical lattice constant is on the order of angstroms. Therefore, the necessary magnetic field is on the order of hundred thousands of Tesla,  $B \approx 10^6 T$ . This is surely not accessible except for neutron stars. It is possible to overcome this by several

methods. First, one can increase the lattice constant by two stacked layers to form a superlattice[14]. The area of the unit cell is squared and the signature of the quantum Hall states were observed. Another new approach is implemented in cold atom systems. The realization of artificial gauge fields[15, 16] in optical lattices can simulate the Hofstadter Hamiltonian. This approach creates arbitrary lattices with various lattice parameters. Moreover, another demonstration creates the two dimensional tunable optical lattices[17]. This capability makes the analysis of an electron moving in the arbitrary lattices under a magnetic field and their dynamical properties interesting problems.

In a previous article [18], we investigated the band structure of the two dimensional(2D) optical lattices realized by the Zurich group[17]. We also calculated the topological properties of such a system and the change of Chern number by making an adiabatic transition from the square lattice to a Honeycomb-like geometry. Along the transition, the cell size is maintained to be a square lattice and the in-situ potential is deformed by displacing the potential minima within the unit cell. The resulting lattice has an effective Honeycomb geometry yielding Dirac points under zero magnetic field.

In this chapter, we answer the question of how the energy spectrum changes as the Bravais lattice point group symmetries are adiabatically changed. In particular, we analysed all possible transitions between point symmetry groups. We first take a spatially-varying sinusoidal potential which capable of forming an arbitrary two dimensional Bravais lattice with a single basis. Hence, one can examine a scenario where one set of the lattice parameters belonging to a specific point symmetry group make a transition to another point group symmetry by tuning the lattice parameters. In the deep lattice limit, such a system can be described by a tight binding (TB) Hamiltonian. The parameters of this Hamiltonian are obtained by fitting the energy bands of the TB Hamiltonian to necessary energy bands for the numerical solution to the Schrödinger equation for the real space potential, where one can calculate the Wannier functions (WF) and the tight-binding parameters.

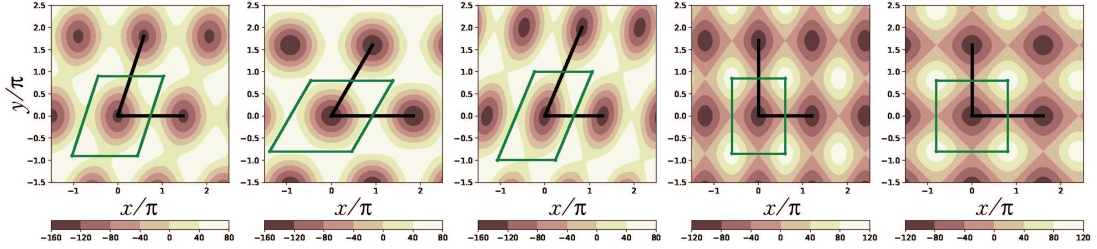


Figure 3.1: All 2D Bravais lattices can be generated by the spatial potential proposed in Eq.3.3. Starting from the left, there are five Bravais lattices, oblique, centered-rectangular(rhombic), triangular, rectangular, square lattices. The lattice depths are chosen as  $V_x = V_y = 50$ (units of  $E_R$ ) such that the tight binding limit is guaranteed, where  $E_R = \hbar^2/2m\lambda_1^2$  is the recoil energy. The thick black lines show the primitive vectors of the Bravais lattice. The unit cell is enclosed with thick solid lines.

As soon as the TB parameters are calculated, the system we desire, the particle under a magnetic field in a periodic potential can be introduced by the Peierls substitution[19]. The tight binding parameters obtained in zero magnetic field case are modified with a complex phase provided that the total phase within the smallest enclosed area is proportional to the magnetic flux within the corresponding loop. This way of introducing the magnetic field is relevant to recent cold-atom experiments, because the artificial magnetic field is imprinted by modifying the tunneling links between adjacent sites in an optical lattice[16, 15, 20]. Hence, one does not have to worry about a possible change in the magnetic flux while changing its geometry, because the enclosed flux is constant.

The TB Hamiltonian generates a reduced  $q$ -by- $q$  matrix utilizing a translational symmetry for a magnetic flux in each unit cell,  $\phi = p/q$ . Note that  $p$  and  $q$  are mutually prime numbers and it covers all possible rational numbers. The numerical exact diagonalization of the model Hamiltonian within the magnetic Brillouin zone yields the energy bands. This calculation is to be carried out for each 2D Bravais tight binding lattice parameters and we obtain each energy spectrum as well as their evolution in time.

It is found that the energy spectrum is critically dependent on the point group, namely the type of Bravais lattices[21]. In two dimensions, the point groups are characterized by five distinct categories depending on the number of symmetries

they possess. First of all, let us take the triangular or the hexagonal lattice. It is the most symmetric lattice among all 2D lattices. It has three mirror symmetries,  $C_1$ ,  $C_3$ , and  $C_6$  rotational symmetries, inversion symmetry along the perpendicular axis. The square lattice has four mirror symmetries,  $C_1$ ,  $C_2$  and  $C_4$  rotational symmetries and inversion symmetry. Breaking one of the mirror symmetries generates the centered rectangular and the rectangular lattices. Both of them have two mirror symmetries,  $C_1$ ,  $C_2$  rotational symmetries, and inversion symmetry. Note that all two dimensional lattices fall under the most general lattice, are the oblique lattice, which has no necessary mirror symmetry,  $C_1$  and  $C_2$  rotational symmetries, lastly the inversion symmetry. We expect certain symmetries to be broken or to be re-established which consequently bring topologically different Hofstadter butterflies. For this purpose, we parametrize the 2D Bravais lattices and analyse the evolution of the Hofstadter butterfly during the transition between different lattice geometries.

The most interesting evolution is the transition from the square lattice to the triangular lattice. One of main diagonal gaps of the Hofstadter spectrum gets smaller and divides into smaller gaps to disappear, then the fractal energy spectrum of the triangular lattice takes over during this process. This transition is non-trivial, because there are infinitely many gap closures and (re-)openings. The gap equations characterizing the topological properties of two point groups are different and these non-trivial gap events are valuable to connect these two limits. It is found that a small variation in the highest symmetry points can only be done by a broken symmetry. The departure from the Square lattice immediately breaks the bipartite symmetry of the lattice, then  $\pm$  energy symmetry around  $E = 0$  is broken. It is totally attenuated in the triangular lattice limit. In the same limit, the area of the unit cell is halved as well as the magnetic flux for the smallest plaquette, which is the unit cell. Thus, the periodicity of the fractal spectrum as a function of magnetic flux is doubled.

The transition from the triangular lattice to the square lattice has been studied before by Hatsugai and Kohmoto [1] with next nearest neighbour (nnn) in the square lattice. This connection is directly imposed by the tight-binding Hamiltonian without considering a real-space spatial lattice which makes sense of the

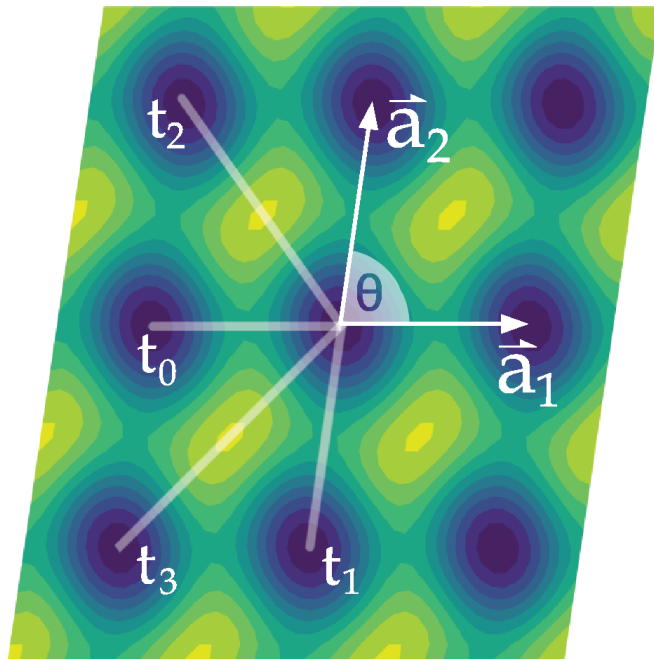


Figure 3.2: The tight-binding model for the arbitrary potential. It must have at least eight neighbors shown on the blue contour plot of the spatial potential to capture all possible transitions. Two arrows show the primitive lattice vectors, and the transparent thick lines represent the tight binding hopping parameters,  $t_0, t_1, t_2$  and  $t_3$ . Note that the symmetric hoppings are found to have same hopping amplitude.

values of the hopping parameters. We take the route of numerically calculating the tight-binding hopping parameters ab initio, considering a real space potential and make the connection with the corresponding hopping parameters in the deep lattice limit for the most general Bravais lattice. Our results agree with those in Ref.[1] for the case of the transition between the square lattice to the triangular lattices.

Another transition, from the square lattice to the rectangular lattice, gives an important clue on how the fractal spectrum is constructed out of a single ground state band. If the system is in the far rectangular limit, the overlap of the Wannier states have vanishing coefficients, and the whole system becomes a set of one dimensional lattices. In this configuration, the effect of the magnetic field is simply lifted by a simple gauge transformation and the initial zero-field continuous band for each chain is retained. Starting from this limit, one can perturbatively connect the isolated chains and observe the construction of the self-similar energy spectrum with higher order terms step by step. The inclusion of interactions in such a system creates the fractional quantum Hall states as excited states[22]. We analyse other transitions like the ones from the centered rectangular lattice to the triangular lattice and the oblique lattice to the rectangular or the centered rectangular lattices and show the distinct energy spectrum change.

Another perspective to analyse such transitions among the point groups can be tracked by the change in the Hall conductance. Thus, we calculate the Chern numbers of the significantly large gaps during a transition scenario. We observe that the Chern numbers are transferred as integer multiples of the denominator of the magnetic flux per plaquette,  $q$ , whenever two bands touch and re-dressed to open a gap. This behaviour is due to the degeneracy by  $q$  in momentum space. It leads to the emergence of  $q$  Dirac cones and transfer of Chern numbers by  $q$ . In order to characterise the space of 2D Bravais lattices topologically, we first take two close loops for fixed magnetic flux per plaquette and calculate the evolution of the Chern numbers in the gaps while tracking various lattice geometries during the cycle. In addition, we numerically derive the Chern number map of all lattice geometries and topologically characterise the lattice geometries for fixed dimensionless magnetic flux at  $1/3$ .

This chapter is organized as follows: Section 3.1 proposes the real space optical lattice potential and derives an adequate tight-binding model under a uniform magnetic field. Section 3.2 deals with the exact diagonalization of the corresponding tight-binding Hamiltonian and numerical calculation of the energy spectrum. In the next section, all possible transitions among the Bravais lattices and the evolution of their energy spectra. Then in section 3.4, the Bravais lattices are topologically characterized by their Chern numbers for the energy gaps at each magnetic flux. To conclude the chapter, we overview the results and consider the experimental possibilities to observe the lattice transitions.

### 3.1 The Model

This section first focuses on an optical lattice potential capable of creating arbitrary 2D Bravais lattices. Then, the lattice is described in the deep potential limit by a proper tight binding model. The effect of the magnetic field is substituted by the Peierls method [19] in the next section.

All Bravais lattices are described by their primitive vectors[21]. We consider two arbitrary vectors, one of them is directed along the  $x$ -axis without a loss of generality as follows,

$$\begin{aligned}\vec{a}_1 &= \lambda_1 \hat{x}, \\ \vec{a}_2 &= \lambda_2 (\cos \theta \hat{x} + \sin \theta \hat{y}).\end{aligned}\tag{3.1}$$

Parameter  $\theta$  determines the angle between the primitive vectors and the lattice constants are denoted by  $\lambda_1$  and  $\lambda_2$ . Resulting Bravais lattice points are constructed as,

$$\begin{aligned}\vec{R}_{n_1, n_2} &= n_1 \vec{a}_1 + n_2 \vec{a}_2, \quad n_1, n_2 \in \mathbb{Z}, \\ &= [(\lambda_1 n_1 + \lambda_2 n_2 \cos \theta) \hat{x} + (\lambda_2 n_2 \sin \theta) \hat{y}].\end{aligned}\tag{3.2}$$

This arbitrary lattice is, by definition, discrete translationally invariant under each translation by  $\vec{R}_{n_1, n_2}$ .

Such an arbitrary lattice can be realized with a spatial optical lattice potential  $V(x, y)$ , as shown in Fig.3.1. With minimum number of Fourier coefficients, such a potential is proposed as,

$$\begin{aligned}
V(x, y) &= -V_X \cos(\vec{k}_1 \cdot \vec{x}) - V_Y \cos(\vec{k}_2 \cdot \vec{x}) \\
&\quad - 2 \cos \theta \sqrt{V_X V_Y} \cos((\vec{k}_1 - \vec{k}_2) \cdot \vec{x}).
\end{aligned} \tag{3.3}$$

It is a sinusoidal potential and they are commonly generated in cold atom experiments by two or three retro-reflected lasers. The potential in Eq.3.3 can be generated by three lasers, but the term in the potential, namely the interference term can be produced simultaneously if  $|\vec{k}_1| = |\vec{k}_2|$ . The wave vectors of lasers are given as  $\vec{k}_1 = \frac{2\pi}{\lambda_1 \sin \theta} (0, 1)$ ,  $\vec{k}_2 = \frac{2\pi}{\lambda_2 \sin \theta} (-\sin \theta, \cos \theta)$  as a function of  $\theta$ .

All 2D Bravais lattices can be realized with two parameters in our system, and they are  $|\vec{a}_2/\vec{a}_1| = |\lambda_2/\lambda_1|$  and  $\theta$ . This mapping is valid at each length scale. We first write the Schrödinger equation and solve the continuum system for the above potential as,

$$\left[ -\frac{\hbar^2}{2m} (\partial_x^2 + \partial_y^2) + V(x, y) \right] \psi(x, y) = E \psi(x, y).$$

A typical method is to use a finite difference method for the system under magnetic field and obtain the energy spectrum. It requires vast computational effort, because the translation symmetry group for non-zero magnetic field is much more complicated than common crystal symmetries[23]. Alternatively, we deal with the lowest band and project the continuum Hamiltonian onto this band in momentum space and describe it with a tight-binding model. This description captures the underlying physics as long as the lattice depth is much larger than the recoil energy,  $E_R = \hbar^2/2m\lambda_1^2$ . Also, the effect of the magnetic field can simply be introduced into the system by Peierls substitution.

The tight binding parameters for the lowest band of the continuum system can be calculated by two methods. In the first case, one can obtain the energy band for the tight binding lattice and fit the hopping parameters to match with the lowest band of the continuum solution within the Brillouin zone. Secondly, the Wannier functions for the lowest band are calculated and the tight binding parameters can

be calculated from the first principles for a single orbital at each site. We prefer the second method with an alternative description of the Wannier functions [24], which provides an easy way of constructing such localized functions. The whole procedure is explained in detail, in Appendix A. The fitting method is used to cross-check the parameters obtained from Kivelson's method[24] and it is found that they are in agreement within our assumptions for the system.

The traditional definition of Wannier functions have an ambiguity in phase factor while integrating along all Bloch waves within the Brillouin zone. The choice of gauge determines the spread of the resulting function and a typical maximal localization is achieved with a computational burden[25]. There is a good candidate definition by Kivelson[24] for Wannier functions as eigenfunctions of projected position operators. The position operator is projected to the single isolated band with a band index  $n$ ,  $\hat{x}_n$ , and it is defined as,

$$\begin{aligned}\hat{x}_n &= \hat{P}_n \hat{x} \hat{P}_n, \\ \hat{y}_n &= \hat{P}_n \hat{y} \hat{P}_n,\end{aligned}$$

where the band projection operators for the  $n$ th band is

$$\hat{P}_n = \sum_k^{BZ} |n, k\rangle \langle n, k|. \quad (3.4)$$

diagonalizing this operator in the position space directly yields the eigenstates as the Wannier functions, where the eigenvalues are their center coordinates,

$$\hat{x}_n |W_n(\vec{r} - \vec{R})\rangle = \vec{R}_x |W_n(\vec{r} - \vec{R})\rangle.$$

This definition not only works for an infinite system as a part of the standard definition by a Fourier transform but also works in finite and disordered systems. Hence, we utilize this definition in a finite lattice of our system to calculate the tight binding hopping parameters.

To obtain the Wannier functions, we first take a finite continuum system with four unit cells along the direction of each primitive vector. The wavefunctions obtained from the numerical solutions of this system are used to create the projection operators and the projected position operator. However, note that we

do not have a periodicity for a finite system therefore the formation of such a projection operator in Eq.3.4 does not seem to be possible. However, we can still generate the projection operator with the following argument. Consider larger and larger lattices; they are not periodic as long as the number of lattice sites goes to infinity. However, we can observe the accumulation of the energy eigenvalues as we increase the number of unit cells. We can well take the lowest accumulated energy eigenstates as the equivalent lowest band and generate the required operators. The projection operator of the lowest band is generated out of the first sixteen nearly degenerate states for a 4-by-4 finite system with sixteen unit cells. The crucial point is each projected position operator  $\hat{x}_n$  and  $\hat{y}_n$  do not commute. Therefore, it does not seem to be possible to simultaneously diagonalize them. However, one can readily check that even for a 4-by-4 lattice, the commutation of these operators are almost negligible and one can diagonalize a linear combination of two operators, for example  $\hat{O}_n = \hat{x}_n + \alpha\hat{y}_n$ , where  $\alpha$  is an arbitrary scale factor. It is noteworthy that even a 4-by-4 lattice comfortably captures the hopping parameters in an infinite lattice scenario with less than one percent error.

During all the evolution scenarios involving five distinct Bravais lattices, the number of nearest neighbors (NN) and the next nearest neighbors (NNN) can change. To capture all such changes, we take eight neighbors for the tight binding model. These neighbors are shown in fig.3.2. Half of the corresponding hopping parameters are identical to their partners under inversion symmetry.

The tight binding Hamiltonian for this system is,

$$\hat{\mathcal{H}} = - \sum_{m_1, m_2} \left[ \begin{aligned} & t_0 |m_1 + 1, m_2\rangle \langle m_1, m_2| \\ & + t_1 |m_1, m_2 + 1\rangle \langle m_1, m_2| \\ & + t_2 |m_1 - 1, m_2 + 1\rangle \langle m_1, m_2| \\ & + t_3 |m_1 + 1, m_2 + 1\rangle \langle m_1, m_2| \\ & + h.c. \end{aligned} \right]. \quad (3.5)$$

The energy eigenvalue equation,  $\hat{\mathcal{H}}|\Psi\rangle = E|\Psi\rangle$  can be represented in the localized basis as  $|\Psi\rangle = \sum_{n_1, n_2} \psi_{n_1, n_2} |n_1, n_2\rangle$ , and we obtain the following second order

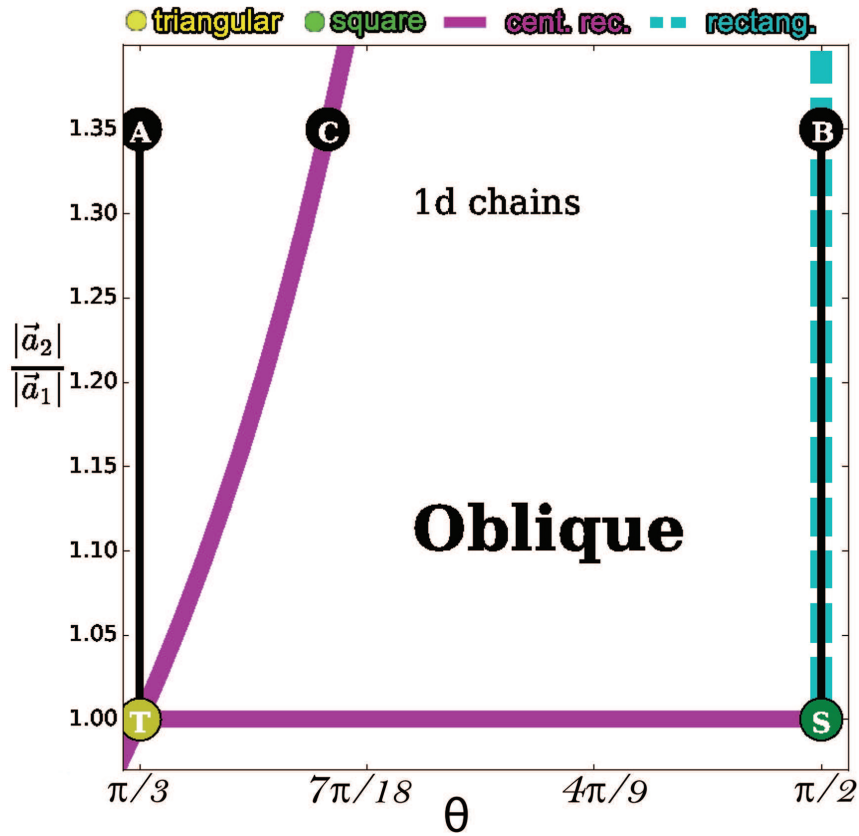


Figure 3.3: The parameter space of all 2D Bravais lattices, shown as a function of the angle between the primitive vectors  $\theta$  and the ratio of the lattice constants  $\frac{|\vec{a}_2|}{|\vec{a}_1|}$ . As the number of simultaneous symmetries increase, lattices of high symmetry are shown by lines and points, there is a dimensional reduction. The triangular lattice and the square lattice are shown with yellow (T) and green (S) points. The rectangular lattice is denoted with blue (S to B, dashed) line and the centered rectangular lattice is denoted with two purple (T to C and T to S, thick solid) lines.

difference equation on each localized site  $|n_1, n_2\rangle$ :

$$\begin{aligned}
E\psi_{n_1, n_2} &= -2t_0\psi_{n_1, n_2} - t_1\psi_{n_1, n_2-1} - t_1\psi_{n_1, n_2+1} \\
&- t_2\psi_{n_1+1, n_2-1} - t_2\psi_{n_1-1, n_2+1} \\
&- t_3\psi_{n_1-1, n_2-1} - t_3\psi_{n_1+1, n_2+1}.
\end{aligned} \tag{3.6}$$

It is a two-dimensional difference equation with boundary conditions  $\psi_{n_1+n_0, n_2+m_0} = e^{ik_1n_0+ik_2m_0}\psi_{n_1, n_2}$ , where  $k_i \triangleq \vec{k} \cdot \vec{a}_i$ , and  $i \in \{1, 2\}$  are the primitive lattice vector indices. It indicates that the Hamiltonian is invariant under discrete lattice translations ( $T_x = |n_1+1, n_2\rangle\langle n_1, n_2|$ ,  $T_y = |n_1, n_2+1\rangle\langle n_1, n_2|$ ) and the wavefunctions at each site are connected by a Bloch phase. Hence, one can choose a mutual basis for the operators  $\{H, T_x, T_y\}$ ,

$$\psi_{n_1, n_2} = \sum_{k_1, k_2} A_{k_1, k_2} e^{ik_1n_1} e^{ik_2n_2}. \tag{3.7}$$

The first term of Eq.3.6 is a constant. Then the difference equation yields the following energy dispersion relation,

$$\begin{aligned}
E(k_1, k_2) &= -2t_0\cos(k_1) - 2t_1\cos(k_2) \\
&- 2t_2\cos(k_1 - k_2) - 2t_3\cos(k_1 + k_2).
\end{aligned} \tag{3.8}$$

The wavenumbers are determined by the geometry of the lattice. The resulting energy dispersion relation in Eq.3.8 is capable of generating the energy spectrum for all two dimensional Bravais lattices. For a clear picture, we plot the energy dispersion in the square and triangular lattice limits in Fig.3.4.

Calculation of the tight binding parameters are discussed in AppendixB. From this point on, we have the hopping parameters calculated from the continuous potential, Eq.3.3. We include the magnetic field by the Peierls substitution[19]

$$t_{\mathbf{m}, \mathbf{n}} |\vec{R}_{\mathbf{n}}\rangle \langle \vec{R}_{\mathbf{m}}| \rightarrow e^{i\Theta_{\mathbf{m}, \mathbf{n}}} t_{\mathbf{m}, \mathbf{n}} |\vec{R}_{\mathbf{n}}\rangle \langle \vec{R}_{\mathbf{m}}|,$$

where  $\mathbf{m} = (m_1, m_2)$  and  $\mathbf{n} = (n_1, n_2)$ . First of all, we choose the magnetic vector potential in the Landau gauge along  $\vec{a}_1$  direction,  $\vec{A} = By\hat{x}$ . The phase acquired when a particle hops from one arbitrary lattice point to another,  $\vec{R}_{m_1, m_2} \rightarrow \vec{R}_{n_1, n_2}$

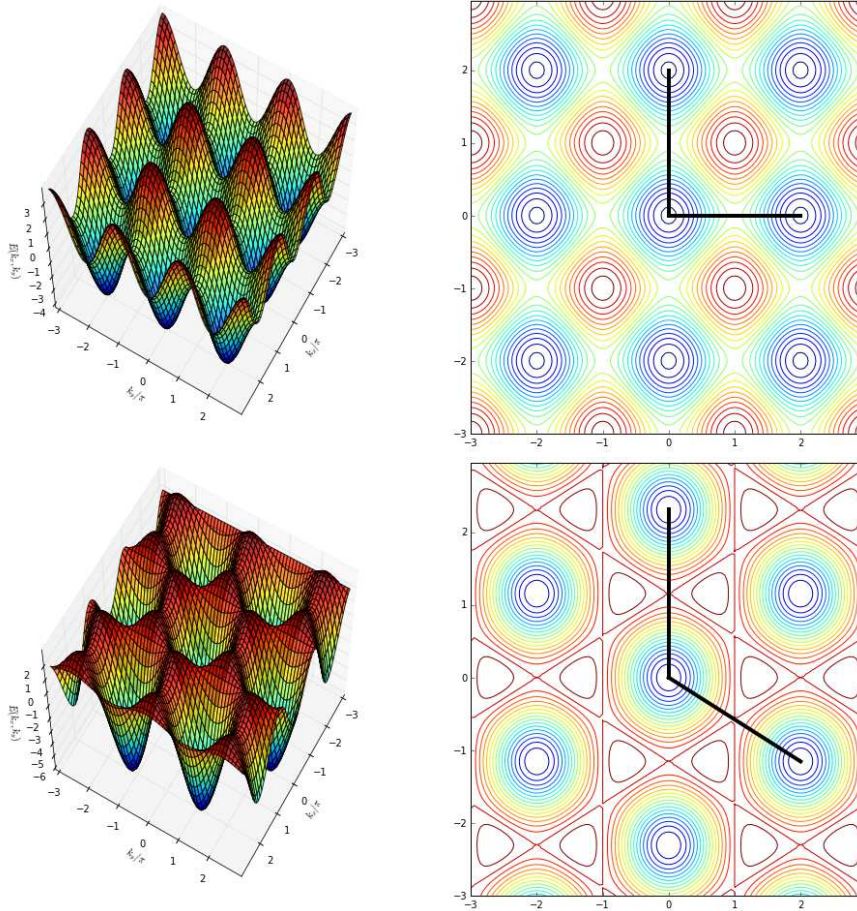


Figure 3.4: The energy dispersion relation in Eq.3.8 is plotted for the square and triangular lattices. All possible energy bands of the 2D Bravais lattices projected onto the lowest band can be described by this function. In our two plots, the lattice parameters are,  $t_0 = t_1 = 1, t_2 = t_3 = 0.035$  for the square lattice,  $t_0 = t_1 = t_2 = 1, t_3 = 0.0$  for the triangular lattice.

is calculated from the line integral above (See Appendix C) as,

$$\begin{aligned}\Theta_{\mathbf{m},\mathbf{n}} &= -\frac{e}{\hbar} \int_{\vec{R}_{\mathbf{m}}}^{\vec{R}_{\mathbf{n}}} \vec{A} \cdot d\vec{\ell} \\ &= 2\pi\phi([\vec{R}_{\mathbf{n}} - \vec{R}_{\mathbf{m}}] \cdot \hat{x}) \left( \frac{\vec{R}_{\mathbf{n}} + \vec{R}_{\mathbf{m}}}{2} \cdot \hat{y} \right),\end{aligned}$$

where  $\phi = B\lambda_1\lambda_2 \sin\theta/\phi_0$  is magnetic flux per plaquette normalized by the magnetic flux quantum  $\phi_0 = h/e$ . This method is proved to work in magnetic tb systems as long as the zero-field version have the same hoppig parameters is valid[26].

The new magnetic field Hamiltonian is the modified version of the zero field Hamiltonian,

$$\begin{aligned}\hat{\mathcal{H}} &= - \sum_{m_1, m_2} \left[ \right. \\ &\quad t_0 e^{-i2\pi\phi m_2} |m_1 + 1, m_2\rangle \langle m_1, m_2| \\ &\quad + t_1 e^{-i2\pi\phi \frac{\lambda_2}{\lambda_1} \cos\theta(m_2+1/2)} |m_1, m_2 + 1\rangle \langle m_1, m_2| \\ &\quad + t_2 e^{i2\pi\phi(1-\frac{\lambda_2}{\lambda_1} \cos\theta)(m_2+1/2)} |m_1 - 1, m_2 + 1\rangle \langle m_1, m_2| \\ &\quad + t_3 e^{-i2\pi\phi(1+\frac{\lambda_2}{\lambda_1} \cos\theta)(m_2+1/2)} |m_1 + 1, m_2 + 1\rangle \langle m_1, m_2| \\ &\quad \left. + h.c. \right].\end{aligned}\tag{3.9}$$

The tight binding Hamiltonian is modified with the dimensionless parameter,  $\phi$  the magnetic flux per plaquette per flux quantum. The smallest area which can enclose a non-zero magnetic flux is the primitive unit cell, and it changes as a function of the lattice geometry. Hence, one can investigate the evolution by two approaches. In the first one, both the lattice geometry and the magnetic flux change. In the second case, the magnetic flux per flux quantum,  $\phi$  is fixed during the lattice transition. In contrary to the common sense, the second approach is more relevant to cold-atom experiments. It is because the magnetic flux is simulated by the artificial gauge fields and in each different gauge choice, the Peierls phase is imprinted on the links. That is why the Peierls phase and the enclosed flux does not change as one change the lattice geometry. In addition, we calculate the energy spectrum for all possible geometries and the magnetic fluxes; this choice is valid without loss of generality.

## 3.2 Calculation of the Energy Spectrum

Acting the Hamiltonian under magnetic field in Eq.3.9 on a localized basis  $|\Psi\rangle = \sum_{n_1, n_2} \psi_{n_1, n_2} |n_1, n_2\rangle$ , gives the following equation,

$$\begin{aligned}
E\psi_{m_1, m_2} = & - t_0 \left( e^{-i2\pi\phi m_2} \psi_{m_1-1, m_2} + e^{i2\pi\phi m_2} \psi_{m_1+1, m_2} \right) \\
& - t_1 \left( e^{-i2\pi\phi \frac{\lambda_2}{\lambda_1} \cos \theta (m_2-1/2)} \psi_{m_1, m_2-1} \right. \\
& \quad \left. + e^{i2\pi\phi \frac{\lambda_2}{\lambda_1} \cos \theta (m_2+1/2)} \psi_{m_1, m_2+1} \right) \\
& - t_2 \left( e^{i2\pi\phi \left(1 - \frac{\lambda_2}{\lambda_1} \cos \theta\right) (m_2-1/2)} \psi_{m_1+1, m_2-1} \right. \\
& \quad \left. + e^{-i2\pi\phi \left(1 - \frac{\lambda_2}{\lambda_1} \cos \theta\right) (m_2+1/2)} \psi_{m_1-1, m_2+1} \right) \\
& - t_3 \left( e^{-i2\pi\phi \left(1 + \frac{\lambda_2}{\lambda_1} \cos \theta\right) (m_2-1/2)} \psi_{m_1-1, m_2-1} \right. \\
& \quad \left. + e^{i2\pi\phi \left(1 + \frac{\lambda_2}{\lambda_1} \cos \theta\right) (m_2+1/2)} \psi_{m_1+1, m_2+1} \right).
\end{aligned}$$

The magnetic vector potential with zero electric potential is chosen as the Landau gauge, and  $\vec{A}$  is parallel to one of the primitive vectors,  $\vec{a}_1$ . This directional choice is advantageous since the magnetic Hamiltonian still preserves the zero-field discrete translation symmetry in  $\vec{a}_1$ . The eigenstates of the Hamiltonian is chosen as the mutual eigenstates of the translation operator. The wavefunction is written as a superposition of plane waves times an undetermined function of  $m_2$ .

$$\psi_{m_1, m_2}(k_1, k_2) = e^{ik_1 m_1} g_{m_2}(k_1, k_2), \quad (3.10)$$

with the choices  $k_{1,2} = \vec{k} \cdot \vec{a}_{1,2}$ . By this way, it is possible to reduce the two dimensional difference equation into one dimensional difference equation for  $g_{m_2}(k_1, k_2)$ .

The difference equation is periodic for the rational values of the magnetic flux per plaquette,  $\phi = p/q$ , and  $p$  and  $q$  are mutually prime integers. The reduced

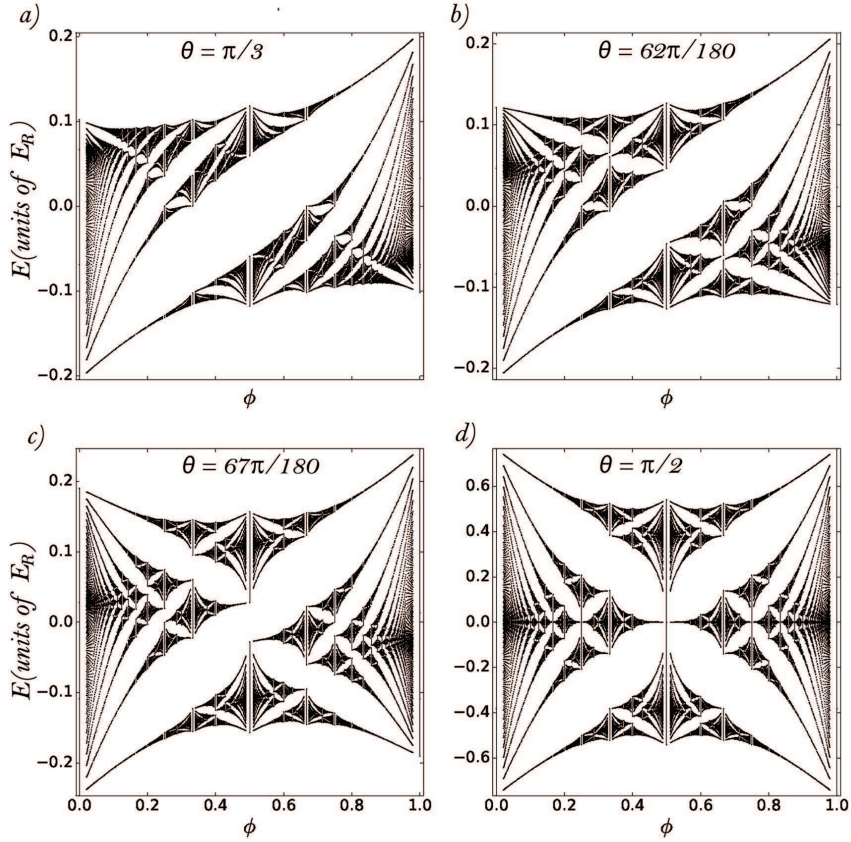


Figure 3.5: The energy spectrum evolves from the triangle lattice to the square lattice. The spectrum is shown with four representative points of  $\theta$ , as shown in *a, b, c, d*. The transition between the lattice geometries is non-trivial. One of the major energy gaps of the square lattice butterfly disappears along the triangular lattice transition. This closing procedure is achieved by infinitely many closures and re-openings of the smaller gaps. The results for this special case is in agreement with those in [1], and additionally show that in a spatial realistic potential, the square to triangular lattice transition qualitatively takes place near the triangular lattice limit,  $\theta \approx 62$  degrees. It means that the major energy gap disappears around  $\theta \approx 62$

one-dimensional equation is,

$$\begin{aligned}
Eg_{m_2} = & - t_0 \left( e^{-i2\pi\frac{p}{q}m_2} e^{-ik_1} g_{m_2} \right. \\
& \left. + e^{i2\pi\frac{p}{q}m_2} e^{ik_1} g_{m_2} \right) \\
& - t_1 \left( + e^{-i2\pi\frac{p}{q}\frac{\lambda_2}{\lambda_1} \cos\theta(m_2-1/2)} g_{m_2-1} \right. \\
& \left. + e^{i2\pi\frac{p}{q}\frac{\lambda_2}{\lambda_1} \cos\theta(m_2+1/2)} g_{m_2+1} \right) \\
& - t_2 \left( e^{i2\pi\frac{p}{q}(1-\frac{\lambda_2}{\lambda_1} \cos\theta)(m_2-1/2)} e^{ik_1} g_{m_2-1} \right. \\
& \left. + e^{-i2\pi\frac{p}{q}(1-\frac{\lambda_2}{\lambda_1} \cos\theta)(m_2+1/2)} e^{-ik_1} g_{m_2+1} \right) \\
& - t_3 \left( e^{-i2\pi\frac{p}{q}(1+\frac{\lambda_2}{\lambda_1} \cos\theta)(m_2-1/2)} e^{-ik_1} g_{m_2-1} \right. \\
& \left. + e^{i2\pi\frac{p}{q}(1+\frac{\lambda_2}{\lambda_1} \cos\theta)(m_2+1/2)} e^{ik_1} g_{m_2+1} \right).
\end{aligned}$$

The difference equation is clearly not periodic by  $q$  translations. However, it can be made  $q$ -periodic by a unitary transformation as discussed in Rammal's paper[27]. The transformation is as follows,

$$g_{m_2} = e^{-i\pi\frac{p}{q}\frac{\lambda_2}{\lambda_1} \cos\theta m_2^2} f_{m_2}.$$

The periodicity of the resulting equation is logically from the perspective of Bloch's theorem. Because, one expects the mixing of  $q$  sites in the presence of  $\phi = p/q$  magnetic flux. Hence, the diagonalization of the following difference equation leads a  $q$ -by- $q$  matrix,

$$\begin{aligned}
Ef_{m_2} = & - t_0 \left( 2 \cos \left( 2\pi\frac{p}{q}m_2 + k_1 \right) f_{m_2} \right) \\
& - t_1 \left( f_{m_2-1} + f_{m_2+1} \right) \\
& - t_2 \left( e^{i2\pi\frac{p}{q}(m_2-1/2)} e^{ik_1} f_{m_2-1} \right. \\
& \left. + e^{-i2\pi\frac{p}{q}(m_2+1/2)} e^{-ik_1} f_{m_2+1} \right) \\
& - t_3 \left( e^{-i2\pi\frac{p}{q}(m_2-1/2)} e^{-ik_1} f_{m_2-1} \right. \\
& \left. + e^{i2\pi\frac{p}{q}(m_2+1/2)} e^{ik_1} f_{m_2+1} \right), \tag{3.11}
\end{aligned}$$

where  $f_{m_2+q} = e^{ik_2q} f_{m_2}$ .

The calculation of the energy spectrum for each value of  $\phi$  is not a trivial task. It is necessary to calculate all possible energies within the Brillouin zone as a function of  $(k_1, k_2)$ . The burden of this computational work is overcome

by determining the band maximum and minimum points at all critical momenta. Simple symmetry arguments regarding the eigenvalue equation of the  $q \times q$  matrix lead the band edges [28, 25, 27] for each  $\phi = p/q$ .

By diagonalizing the  $q \times q$  matrix, we numerically obtain the energy spectrum for an arbitrary Bravais lattice. The next section shows all the energy spectra and discusses all the lattice transitions.

### 3.3 Transitions between Bravais Lattices

This section analyses the transition in the fractal energy spectra as the lattice geometry is adiabatically changed from one point group symmetry to another. Before going into the discussion, the characterization of the Bravais lattices in our system is summarized. All 2D Bravais lattices are characterized by two parameters,  $\theta$  and  $|\vec{a}_2|/|\vec{a}_1|$ . The Fig.3.3 shows the five distinct lattices with different point symmetry groups and all transition paths within the space of two parameters. These five lattices are the triangular, square, rectangular, centered rectangular and oblique lattices. The lattices possessing higher symmetries occupy smaller region. For example, the triangular lattice and the square lattice are represented by point, while the rectangular and the centered rectangular lattices are shown with curves. The most general Bravais lattice, the oblique lattice covers the whole region.

We first start with the transition between two high symmetry point lattices, the triangular and the square lattices. In the parameter space (see Fig.3.3), the transition is represented by the path  $\overline{BA}$ . The spectra are calculated for all points in this path and represented in Fig.3.5 at four points on the path  $\overline{BA}$ .

During the adiabatic transition from the square lattice to the triangular lattice, we calculate the tight-binding hopping elements over the path and obtain the energy spectrum throughout the transition. In the deep lattice potential with  $V_X = V_Y = 50(\text{units of } E_R)$  and  $\theta = \pi/2$ , the potential resembles the square

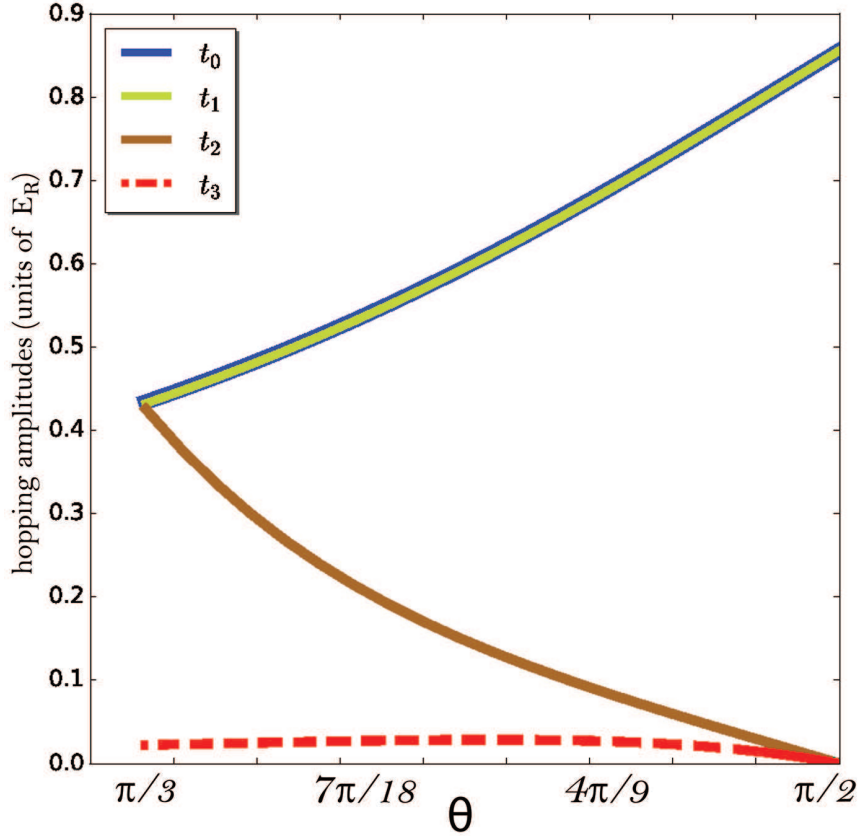


Figure 3.6: The hopping parameters during the transition from the triangular to the square lattice are calculated as a function of angle  $\theta$ . For this purpose, the real space potential parameters are  $V_X = V_Y = 20$ (units of  $E_R$ ). The NN hopping parameters,  $t_0, t_1$  follows the same magnitude and decrease down to  $t_2 = 0.43$ (units of  $E_R$ ) in the triangular lattice limit due to the increase in the strength of the interference term in Eq.3.3. The NNN hopping,  $t_3$  starts almost from zero and increases up to an order of magnitude smaller amplitude,  $t_3 \approx 0.025$ .

lattice, the tight-binding NN hopping parameters are  $t_0 = t_1 = 0.1913$ (units of  $E_R$ ), and the NNN hoppings  $t_2, t_3$  are below our numerical precision. Including their inversion symmetric hopping partners, four of the NN hopping parameters are equal during the transition and they are order of magnitude larger than the four NNN hoppings up until the triangular lattice limit. It is no surprise since the Wannier functions are localized in each unit cell in deep lattice limit and NNN hoppings almost vanish. However, the triangular lattice limit makes  $t_2$  comparable to  $t_0, t_1$  due to the gradual increase of the effect of the interference term in the potential in Eq.3.3. During the transition, the interference term also decreases  $t_0$  and  $t_1$  hoppings until they are equal to  $t_2 = 0.0345$ (units of  $E_R$ ) in the triangular lattice limit (see Fig.3.6).

The decisive property of the square lattice Hofstadter butterfly is the bipartite symmetry (energy is symmetric with respect to  $E = 0$  line) when we neglect NNN hoppings. Even the on-set of non-zero NNN hoppings break; bipartite symmetry, the overall energy spectrum roughly preserves the reflection property. Broken bipartite symmetry is more visible in the vicinity of the triangular lattice and the asymmetry in the energy bands is at its maximum at  $\phi = 1/2$  and proportional to  $t_0 - t_2$ . The asymmetry is the result of the shrinking in one of the diagonal upper left and the lower right energy gaps. At the same time, the upper right and the lower left gaps are enlarged to form the largest gap of the triangular butterfly. The transition occurs in a highly complicated way as there are infinitely many energy gap closures and re-openings. Such a merger and splitting of the bands are among the signatures of the change in the symmetry properties of the system, and in a sense they are expected for an adiabatically disconnected lattices[29].

Highlighting the fact that the high symmetry points of Bravais lattices are denoted with single points, we expect dramatical changes when the system leaves these points. What we find is that the energy spectrum is highly dependent on phase space parameters,  $\theta$  and  $|\vec{a}_2|/|\vec{a}_1|$  near these points. For example, a small angle departure from the triangular lattice limit around  $\theta = 63$  degrees, leads to huge band shifts and band closing and re-openings. Therefore, under the uniform magnetic field, we can expand the definition of the triangular lattice from a single point to a small region of lattice parameters considering experimental concerns.

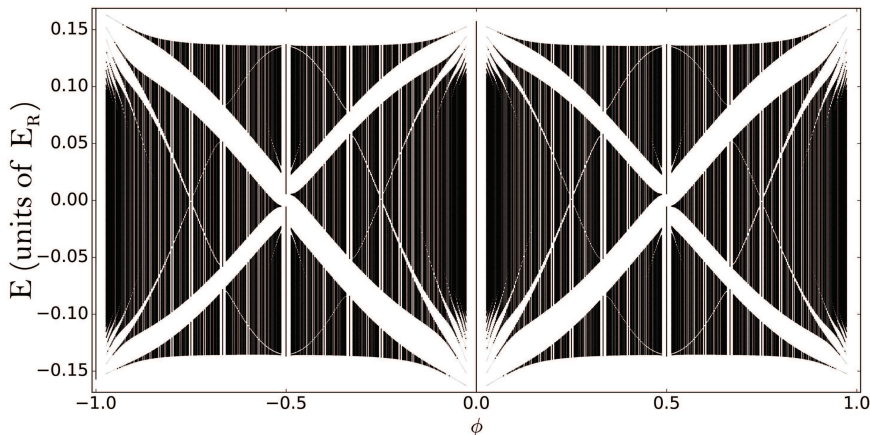


Figure 3.7: The energy spectrum of the oblique lattice. The spectrum is plotted for  $\phi = [-1, 1]$  to underline the doubling in the periodicity of energy. It is also clear that the energy is symmetric under  $\phi \rightarrow -\phi$ . Note that this symmetry is followed by the beloved inversion symmetry that all two dimensional Bravais lattices have.

We keep the convention of a fixed magnetic flux during the lattice transition. By this choice, we observe that the magnetic flux per plaquette is halved at the triangular lattice. As discussed by Claro and Wannier[30], the unit cell is half of the parallelogram forming the lattice. As a result, the energy spectrum is periodic by  $\phi = 2$  as can be grasped from Fig.3.5.

The energy spectra are all symmetric under  $\phi \rightarrow -\phi$  operation. It is a trivial result of the reflection symmetry with respect to z-axis except for the oblique lattice under uniform magnetic field. In the case of the oblique lattice, one can uniquely define the z-axis that the reflection symmetry is broken. However, the inversion symmetry coupled to the reflection symmetry is still preserved with a different choice of primitive vectors and restores  $\phi \rightarrow -\phi$  symmetry (see Fig.3.7). It can only be broken by asymmetric mass terms between the NN sites.

The second adiabatic transition to examine is between the square and the triangular lattices (see Fig.3.9). The study of this transition is useful for two reasons. Firstly, it reveals how the symmetries of the system are related to the energy spectrum in a deeper sense along the transition path  $\overline{BS}$ . Secondly, to understand how the self-similar energy spectrum emerges, we can connect isolated

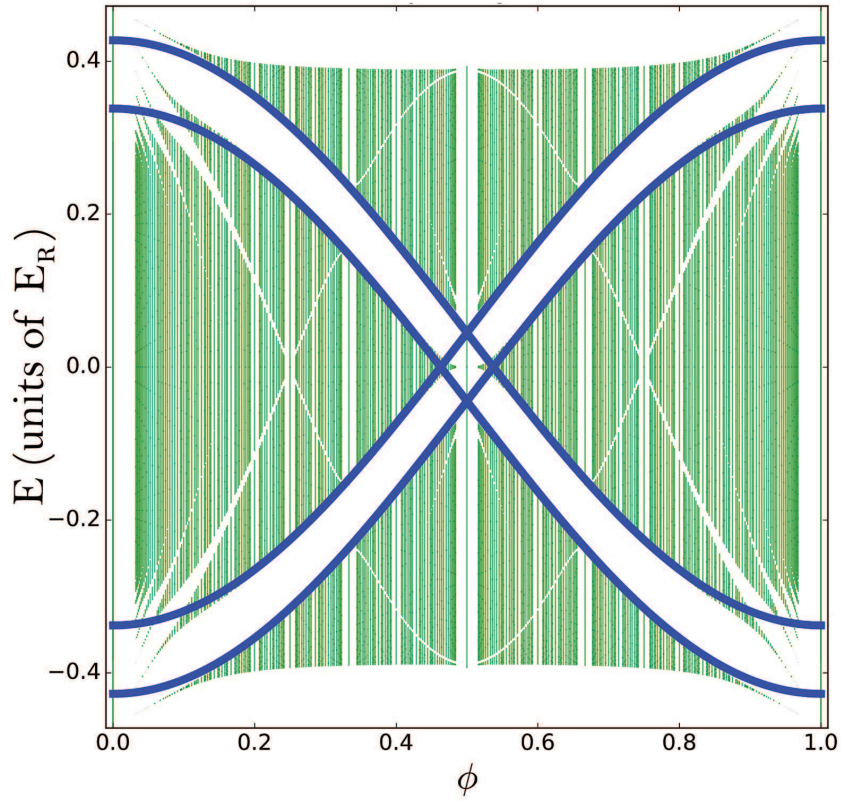


Figure 3.8: The energy spectrum in the rectangular lattice limit is compared with the weak interaction limit of one dimensional infinite chains under magnetic flux  $\phi = p/q$ . The dominant energy gaps are calculated from 1D chains perturbatively. First order calculation yields two large and robust energy gaps even in the far rectangular limit which are shown with thick blue curves. Smaller gaps or the whole energy spectrum can be calculated by higher order perturbative corrections.

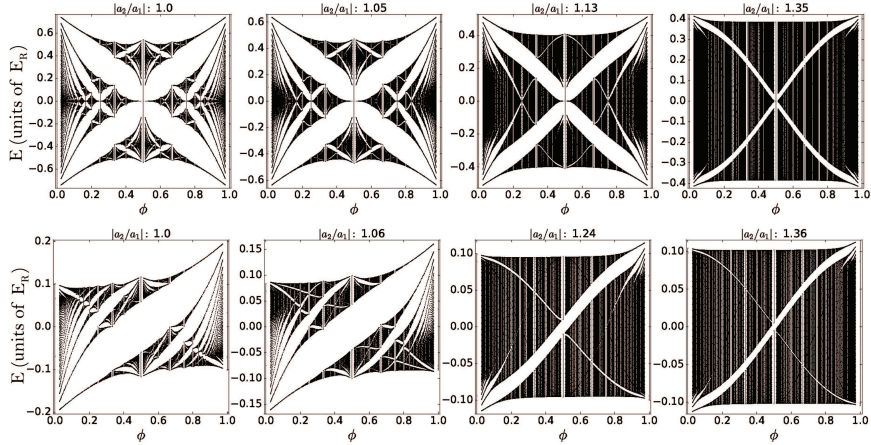


Figure 3.9: Energy spectrum evolution for two scenarios. From the square lattice to the rectangular lattice and from the triangular lattice to the centered rectangular lattice. The first transition is along the straight line along the  $\theta = \pi/2$  line in Fig.3.3. The second transition is along the centered rectangular lattice curve in the same phase diagram. The gaps close as the ratio of the lattice constants increase (see Fig.3.8), and the lowest band splitting gets smaller and smaller.

set of 1D chains and calculate all gaps in the Hofstadter butterfly spectrum perturbatively. During the transition from the square lattice to the rectangular lattice, the energy gaps shrink and vanish in the rectangular limit. The system is described by isolated 1D chains and the effect of the magnetic field in this limit can be gauged out. This behaviour is shown with four representative points in Fig.3.8. Since the magnetic field is the very reason for the band fracturing, it is no surprise to see un-fragmented lowest band in the extreme rectangular lattice (the precise lattice parameters are  $|\vec{a}_1/\vec{a}_2| = 2.5$  and the corresponding hopping amplitudes are  $t_0 = 0.19$ (units of  $E_R$ ),  $t_1 = 0.04$ (units of  $E_R$ ) whereas the other hopping elements are completely vanishing). This limit mainly yields three bands irrespective of the value of the magnetic flux  $\phi = p/q$ .

The major gaps are robust for large ratio of lattice constants. We can understand this with a simple perturbative approach. A collection of isolated 1D chains is considered as the unperturbed part and the hoppings between the chains are the perturbation. The energy dispersion of the  $m^{\text{th}}$  unperturbed chain is,

$$E_m(k_1) = -2t_0 \cos(2\pi\phi m + k_1). \quad (3.12)$$

The adjacent chains' energies are degenerate at two points in the Brillouin zone

and separated by  $2\pi\frac{p}{q}$  for the rational magnetic flux  $\phi = \frac{p}{q}$ . The on-set of the tunneling (parameter  $t_1 \neq 0$ ) among the adjacent chains lifts the degeneracy at these k-points and the energies are modified to be  $\pm 2t_0 \cos(\pi\frac{p}{q} + k_1) \pm t_1$ . In this respect, the interchain hopping parameter,  $t_1$  is the measure of the energy splitting of the main gaps as in Fig.3.8. It is possible to calculate the smaller energy gaps and the Hofstadter butterfly can be re-constructed as the higher order energy corrections are included [31].

This section is concluded with the discussion of transitions from the triangular lattice to the centered rectangular lattice (see Fig.3.9) and to the oblique lattice. The corresponding transitions are denoted in Fig.3.3 by the paths  $\overline{TC}$ ,  $\overline{TA}$ . Both cases are similar to the square to the rectangular lattice transition as the main gaps shrinks to end up with weakly coupled chains. Unlike the transition from the square to the rectangular lattices, there is no bipartite symmetry present both scenarios and only one of the energy gaps is robust. Hence, the presence of two diagonal gaps is a good measure for the bipartite symmetry in extreme asymmetry of the ratio of the lattice constants.

We have a complete picture on the evolution of the energy spectrum, and we show all the energy spectra possible to have for the two dimensional Bravais lattice parameter space (see Fig.3.10).

Our tight-binding model considers the smallest area to enclose flux as half the unit cell formed by a triangle irrespective of its orientation. Hence, all the energy spectra are periodic with  $\phi = 2$ . In the special case of NNN hoppings, where  $t_2$  and  $t_3$  are negligible, the smallest magnetic field enclosing area becomes the unit cell and the periodicity of the spectra with  $\phi = 1$  is recovered. A direct conclusion of this observation is that the periodicity of the energy spectrum with respect to  $\phi$  can be utilized to understand the range of significant hoppings. The larger the periodicity, the longer the range of hoppings are. For example, the triangular lattice, the centered rectangular lattice and the oblique lattice have the energy spectra preserving the periodicity of  $\phi = 2$ . Therefore, not only the NN hoppings but also the NNN hoppings are effective and the smallest flux enclosing cells are the halved unit cells.

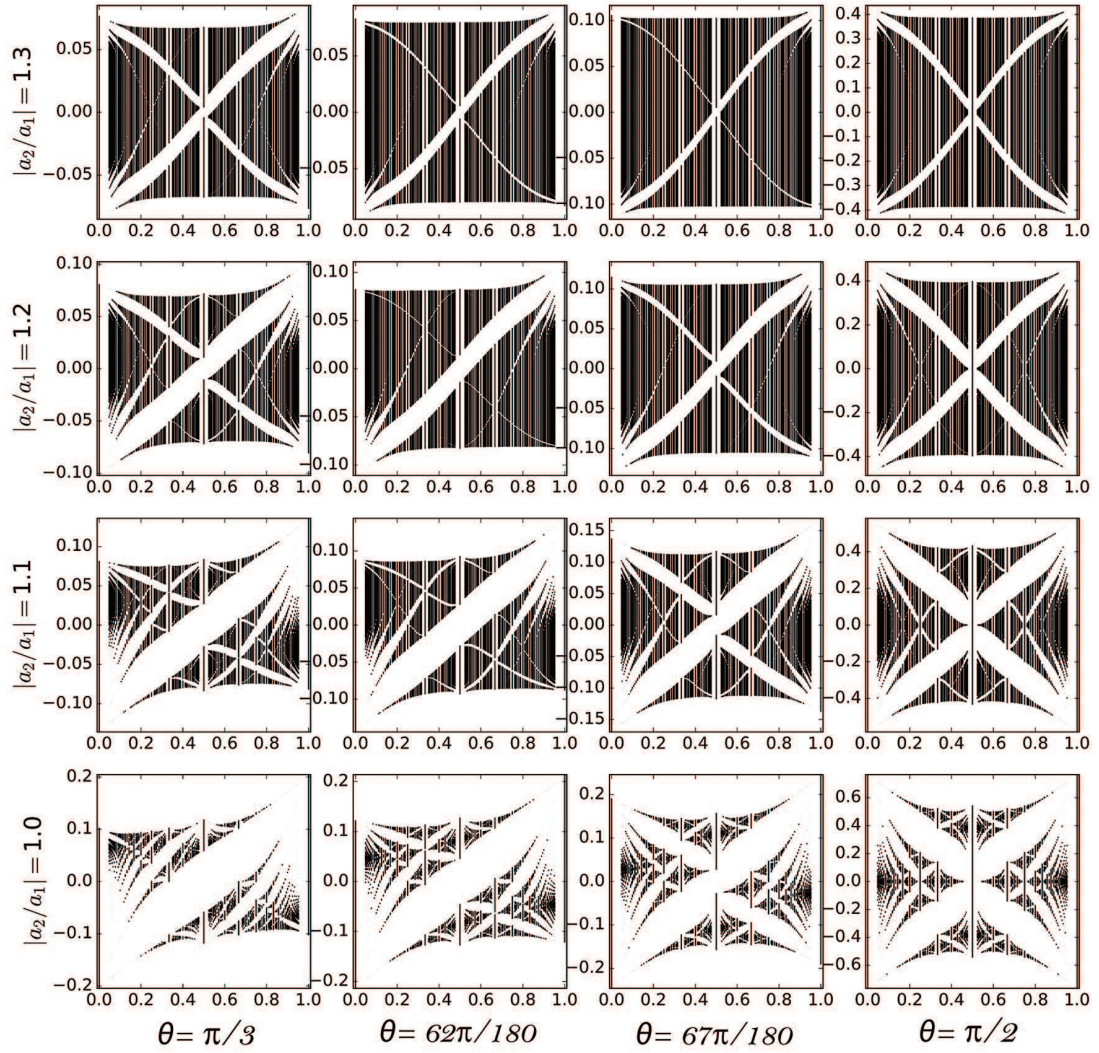


Figure 3.10: In analogy to Bravais lattice phase diagram in Fig.3.3, the Hofstadter butterfly phase diagram in the phase space of two dimensional Bravais lattices.

### 3.4 Topological Characterization of the Bravais Lattice Phase Space

The energy bands of Bravais lattices under a uniform magnetic field are topologically characterized by an invariant called the first Chern number [32]. For a non-interacting fermionic system, this number is equivalent to the contribution of each Bloch band to the Hall conductivity,  $\sigma_{xy} = \mathcal{C}e^2/h$ . Alternative and equal description is that Chern numbers are linked to the energy gaps by the summation of all Chern numbers of each band below that gap. This section is devoted to utilize the Chern numbers to characterize two dimensional Bravais lattices under magnetic field.

The magnetic flux per plaquette per flux quantum,  $\phi = p/q$  creates  $q$  bands and  $q - 1$  gaps out of the lowest band of the zero field lattice. As the gaps are determined by the magnetic flux, the Chern numbers for each of the gaps is different for different lattice geometries. For the square lattice under magnetic flux  $\phi = 1/3$ , there are two gaps and their Chern numbers are  $-1, 1$ . Meanwhile, for the same magnetic flux, the triangular lattice gaps have the Chern numbers  $1, 2$ . The feature of the Chern numbers associated with the gaps or the bands is their robustness under band deformations. In other words, one cannot change these invariants for a specific band as long as there is a gap closure, indicating an adiabatic discontinuity. Making use of this property, it is possible to extend the point symmetry groups for zero-field case to the non-zero magnetic field and classify all 2D Bravais lattices into the equivalence class by their Chern number sequence of the gaps at each  $\phi = p/q$  value. Therefore, we can create a topological phase equivalence class for our parametrization space in Fig.3.3. Consequently, we obtain regions of different topological phases and the corresponding boundaries separating these regions are those where at least one non-trivial gap closure occurs.

The calculation of Chern numbers is done by the total accumulation of the Berry curvature around the Brillouin zone, but one can use an indirect but computationally much simpler approach[33]. The conductivity is a thermodynamic

variable and calculated as a variation of the number of energy levels below the Fermi level with respect to the variations in the magnetic field in a two dimensional system[34]. The lattice version of this relation yields the Chern number for a corresponding energy gap as,

$$\mathcal{C} = \frac{\partial n}{\partial \phi}, \quad (3.13)$$

and  $n(\phi)$  is the total density of a unit cell below the energy gap,  $\phi$  is the magnetic flux per plaquette normalized to the flux quantum. This simple formula suggest that the Chern number can be calculated as a finite difference and the difference in the number of energy levels below the Fermi level for two close magnetic flux values yields this invariant.

The phase space of the 2D Bravais lattices is explored for the first two simplest and non-trivial fluxes,  $\phi = 1/3, 1/5$ . For this purpose, we take a closed transition path in the phase space,  $\overline{ATSB\bar{A}}$ , and calculate the band evolutions. The path is chosen such that the 1D chain limit is avoided, because the energy gaps gets so small as in Fig.3.9 and may lead to numerical errors. It still does not lead to a loss of generality. Both of the band evolutions for  $\phi = 1/3, 1/5$  are shown in Fig.3.11. In the case of  $\phi = 1/3$ , it shows that all possible lattices are either equivalent to the square lattice with Chern numbers  $-1, 1$  or to the triangular lattice with Chern numbers  $2, 1$ . Hence the phase space is divided into two different topological phase class (see Fig.3.12). Specifically speaking, the region equivalent to the triangular lattice topological phase roughly follows the centered rectangular lattice curve. For the magnetic flux  $\phi = 1/5$ , there are four different regions of topological phase indicated in Fig.3.11. As the denominator of the magnetic flux  $q$  gets a larger integer value, the number of gaps increases and the size of the gaps decreases, and the phase diagram divides into smaller topological phase classes.

A significant observation is that the transition at the phase boundaries always occurs with Chern number transfers exactly by an amount of  $q$  for a magnetic flux  $\phi = p/q$ . This exciting observation has a simple and elegant explanation. The magnetic translation symmetry leads to a  $q$ -fold degeneracy inside the magnetic Brillouin zone. If the gap closes and two bands touch, they touch at least with

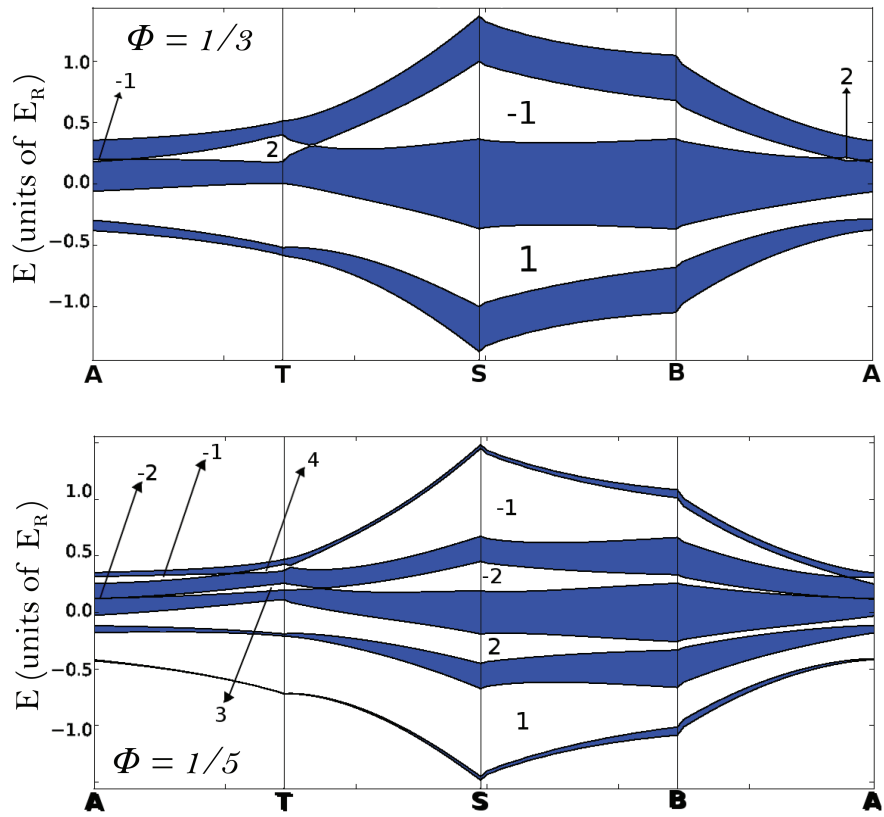


Figure 3.11: The energy band evolution for  $\phi = \frac{1}{3}$  and  $\phi = \frac{1}{5}$  along the closed path  $\overline{ATSB\bar{A}}$  denoted in Fig.3.3. The Chern numbers of the gaps are shown explicitly. For  $\phi = 1/3$ , there are two topologically disconnected regimes in the Bravais lattice space and characterized by the Chern numbers 1,  $-1$  and 1, 2. For the case of  $\phi = 1/5$ , there are four topologically distinct regimes with the Chern numbers labeled on the evolution graph.

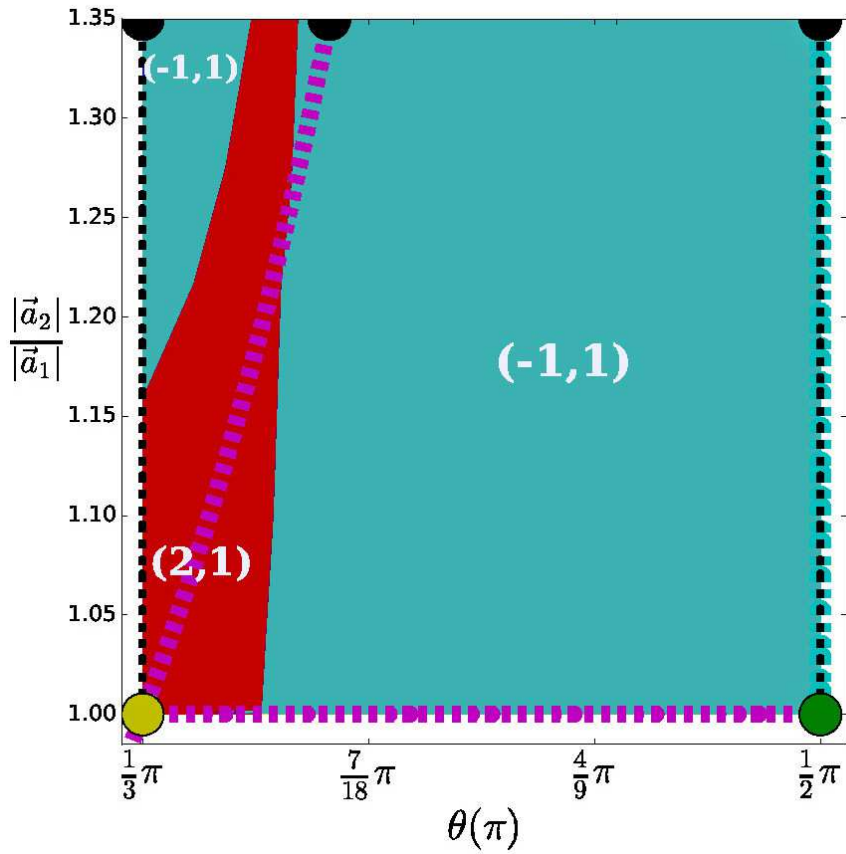


Figure 3.12: Two different topological phases in the two dimensional Bravais lattice phase space for the magnetic flux,  $\phi = 1/3$ . All possible lattices are either classified by Chern numbers  $-1, 1$  including the square lattice or with  $2, 1$  including the triangular lattice. Observe that the triangular lattice topological phase class roughly follows the centered rectangular lattice curve.

$q$  degenerate points. For each closure and reopening of a Dirac cone, there is exactly one Chern number transfer. If each of degenerate points forms a Dirac cone for suitable lattice parameters, the total Chern number exchange is  $q$ . If the degenerate points are of higher order, integer multiples of  $q$  Chern number can also be exchanged. So far, we do not observe such Chern number transfers numerically.

# Chapter 4

## Non-Adiabatic Change in Magnetic Flux

In cold atom experiments, it is possible to investigate many body systems in a clean and controlled environment. Also, external parameters of the Hamiltonian can be controlled much faster than a typical hopping time scale of atoms in such experiments. This capability allows the investigation of non-equilibrium interacting many body systems. Such fast changes are discussed in Section 2.

As another recent development paved the way for the creation of the artificial gauge fields in continuum[35] and in lattice [36, 16] systems for effective charged particles by neutral cold atoms. It is possible to explore a variety of physical phenomena in Abelian and non-Abelian gauge fields, such as the topological properties [37, 38, 39, 40], quantum Hall states[41], Hofstadter's fractal energy spectrum[16, 36] and supersolid-like states in non-abelian fields[42, 43]. Artificial magnetic fields are created by the interaction of atoms with electromagnetic fields and this yield a position dependent momentum shift to simulate spatial vector potentials[44]. However, momentum-shift based real-space phase manipulation in optical lattices makes these experiments non-trivial and puts limitations on the homogeneity and lifetime of the system and the magnitude of the artificial magnetic flux per unit cell[37, 16].

In this chapter, our goal is to understand the effects of a sudden change of artificial magnetic field in a cold atom system. Until recently, it is not possible to change the artificial magnetic field in lattices at fast time scales. The new method, based on utilizing hyperfine levels of atoms in a one dimensional lattice to expand it into two dimensions, the extra one being a synthetic dimension, is a good candidate for a sudden change in the artificial magnetic field[45]. The hyperfine levels are coupled by Raman lasers such that a detuning imprints position-dependent Peierls phases. Unlike the artificial magnetic fields created in real space two-dimensional optical lattices, since a typical Raman frequency is much larger than all inverse time scales in the system, the study of non-adiabatic changes in the artificial magnetic field is possible. In this respect, the time dependent investigation of bosons and fermions are realized in static artificial magnetic fields[46, 47], and the quench scenarios that we consider are within the experimental capabilities of quite a number of research groups.

Putting aside the experimental relevance, the study of time-dependent artificial magnetic fields is valuable for two reasons. The first one is about the method of creating such fields. Current experiments are dependent on simulating the effect of the magnetic vector potential  $\vec{A}$ , but a time dependent effect of this field, the scalar potential  $\Phi$  is lacking. In static gauge fields, two sets of vector potentials yielding the same magnetic field and the scalar potential leads to totally equivalent Hamiltonians which are connected by a gauge transformation,  $\vec{B} = \nabla \times \vec{A}_1 = \nabla \times \vec{A}_2$  and  $\Phi_1 = \Phi_2$ . It means both Hamiltonians lead to identical observables, hence the choice of the gauge does not matter. In the case of time dependent gauge fields, however, it makes a difference due to the realization method of such fields. Even if the two vector potentials have the same curl at each instant of time,  $\vec{B}(t) = \nabla \times \vec{A}_1(t) = \nabla \times \vec{A}_2(t)$ , the corresponding Hamiltonians are disconnected by the lack of equivalence between scalar potentials. This indicates gauge dependence and has interesting consequences as observed with the expansion images of a recent experiment in Ketterle's group[48], where they measure the gauge dependent canonical momentum distribution.

Secondly, the question on if the edge states created under a magnetic field are robust within such non-adiabatic quench scenarios is also important. Normally,

the emergent edge states protected due to topological reasons or the chiral symmetry are robust against perturbations. However, this robustness is not guaranteed by any topological argument after a magnetic field quench.

These questions are answered by analysing the dynamics of wavepackets under sudden changes in the artificial magnetic field. The wavepackets are created in lattices and each lattice configuration is described by a tight binding model, then the effect of the magnetic field is imposed by the Peierls substitution[19]. To emphasize the gauge dependence in dynamical systems, we first propose a toy model, a six site lattice formed by two squares. An arbitrary initial wavefunction is evolved in time for two different vector potentials yielding the same magnetic field. We compare the probability distributions as a function of time and show their evolutions are gauge dependent, and this difference in evolution becomes more apparent as the ramping rate of the artificial magnetic field is from zero to a finite value. We also verify that two disconnected Hamiltonians are reconnected as they are healed with their time dependent on site potentials and the gauge invariance is re-established. We present our results in the next section.

In Section 4.2, the magnetic flux quenches of wavepackets are analysed in two- and three-leg synthetic ladders. Initial Gaussian wavepackets created around an eigenstate of ladder system under zero field are quenched to a non-zero magnetic flux and the initial packet splits into smaller packets with different velocities. It is shown that the gauge choice determines the number and the weight of the resulting sub-packets. In a gauge choice, where the vector potential is perpendicular to the rungs of the ladder for a  $n$ -leg ladder system, the number of the smaller packets after the quench is equal to the number of legs,  $n$ . For a gauge choice, where the vector potential is parallel to the rungs of the  $n$ -leg ladders, there can be at most  $n^2$  packets out of the same initial wavepacket. It is a counter intuitive result since this number is independent of the value of the magnetic flux, whereas the number of the band splitting is theoretically determined by the magnetic flux, at least for the rational values of it. We calculate and quantify the number, the weights and the velocities of the post-quench split packets by the overlap of the pre- and post-quench bands. In a two-leg ladder, in addition, we consider a quench between two arbitrary magnetic fluxes for the vector potential

perpendicular to the rungs and obtain analytical results for packet weights and velocities. In a three-leg ladder, we also focus on a special scenario where an initial wavepacket prepared in the presence of arbitrary non-zero magnetic flux is quenched to zero flux created with a constant vector potential and zero vector potential. We observe that the number and the weight of smaller packets do not change for two cases but the hyperfine distribution of the packets are different. It shows even a trivial difference in vector potentials leading to an observable effect.

In Section 4.2, we analyse the dynamics of the edge states after a flux quench in a wide ribbon which consists of synthetic ladders or the continuum limit of this ribbon. The choice of the gauge is fixed in this scenario, where the vector potential is perpendicular to the rungs. For the thick lattice, the topological edge states are found to survive after the artificial magnetic flux quench with an additional condition. If there exists another edge state residing in the same gap of an initial edge state, we found that the topology of bands is protected and consequently the corresponding edge state survives. If the situation is the opposite and there is no edge state solution, then the initial packet propagates into the bulk and de-coheres into bulk modes. In the continuum limit of the thick ribbon, however, the edge mode solutions are guaranteed for any value of the magnetic flux (field) because of the massive degeneracy. Hence, an initial edge state, after the quench, continues its evolution as skipping quantized orbits. This finding is verified by the numerical calculation of the trajectories of an initial edge state before and after the quench, which shows skipping character with two different radii.

The last section, Section V, concludes the whole work and its experimental indications.

## 4.1 A minimal model

The physics is invariant under gauge transformations since all the observables are independent of the scalar or vector potentials describing them. The wave

functions and the role of the gauge choice is well understood for static scalar and vector potentials. For a time dependent set of vector potentials, two gauge choices describing the same system are related by a gauge transformation,

$$\begin{aligned}\vec{A}_2(\vec{r}, t) &\rightarrow \vec{A}_1(\vec{r}, t) + \vec{\nabla}\Lambda(\vec{r}, t), \\ \Phi_2(\vec{r}, t) &\rightarrow \Phi_1(\vec{r}, t) - \frac{\partial\Lambda(\vec{r}, t)}{\partial t}\end{aligned}\tag{4.1}$$

where  $\Lambda(\vec{r}, t)$  is a scalar function. Considering the artificial gauge fields in cold atom experiments, the situation is more complicated. Because the required scalar potential is not simulated in the experiments, there is no set of dynamical Maxwell's equations governing the system[49]. Hence, a time dependent change in an artificial magnetic flux does necessarily correspond to an artificial electric field. Moreover, a recent experiment[48] in the MIT group has measured the mechanical momentum and the expansion images which are observed to be gauge dependent. It has two possible explanations: First, the system implemented the magnetic field but did not simulate the induced electric field of the dynamical vector potential, and the system does not have a gauge symmetry. Second equivalent interpretation is that a turn-off of the optical lattice does not shut down the magnetic flux but involves an artificial electric field, breaking the isotropy of the lattice.

In this section, we investigate the validity of the gauge-dependence argument that are elaborated above by a simple model. Specifically, we investigate the evolution of an initial wavefunction in two time dependent gauge potentials, which are related by a static gauge transformation. This simple model is a six-site tight-binding lattice, formed by two stacked square lattices (see Fig.4.1). This model can be experimentally realized by two isolated sites of a spin-1 synthetic lattice[45]. All the hopping elements are fixed to a constant kinetic energy,  $J$ , where the left bottom corner is the origin. The wider side of the lattice is chosen as the  $\hat{x}$ -axis. In our scenario, the magnetic flux per square is ramped from zero to a final value  $\phi$ (in units of the flux quantum,  $\phi_0 = h/e$ ), for both gauge potentials, during  $0 \leq t \leq \tau$ .

Let us first define the ramping magnetic field as  $\vec{B}(t) = B_0 f_\tau(t) \hat{z}$ , where the

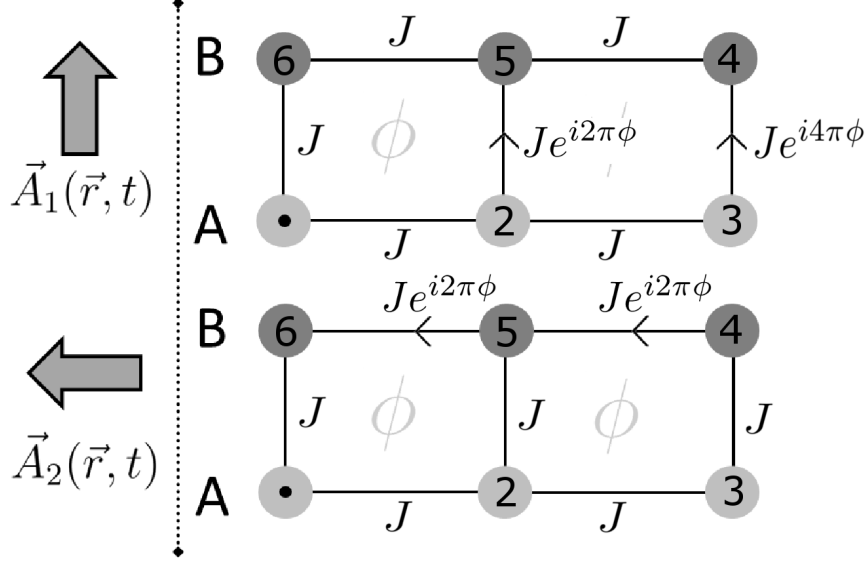


Figure 4.1: The minimal model, made of a six site tight binding lattice as two stacked squares. Two different set of gauge potentials  $\vec{A}_1(\vec{r}, t)$ ,  $\Phi_1(\vec{r}, t)$  and  $\vec{A}_2(\vec{r}, t)$ ,  $\Phi_2(\vec{r}, t)$  yields Hamiltonians in Eq.4.4 and Eq.4.6. The magnetic field modifies the hopping parameters with Peierls phase. The origin is as the left bottom corner.

ramp function  $f_\tau(t)$  is,

$$f_\tau(t) = \begin{cases} 0 & : t \leq 0 \\ \frac{t}{\tau} & : 0 < t < \tau \\ 1 & : t \geq \tau \end{cases} \quad (4.2)$$

and  $\phi = \frac{B_0 a^2}{h/e}$  is the magnetic flux per square with the lattice constant  $a$  normalized by the flux quantum.

The first set of potentials to create the corresponding dynamical flux is defined as,

$$\begin{aligned} \vec{A}_1(\vec{r}, t) &= f_\tau(t) B_0 x \hat{y}, \\ \Phi_1(\vec{r}, t) &= 0. \end{aligned} \quad (4.3)$$

It creates the following Hamiltonian,

$$\begin{aligned} H_1(t) = & - J \left( a_1^\dagger a_2 + a_2^\dagger a_3 + a_4^\dagger a_5 + a_5^\dagger a_6 + a_6^\dagger a_1 + h.c. \right) \\ & - J \left( e^{-i2\pi\phi f_\tau(t)} a_2^\dagger a_5 + e^{-i4\pi\phi f_\tau(t)} a_3^\dagger a_4 + h.c. \right). \end{aligned} \quad (4.4)$$

Note that the Peierls substitution leads to the modification of the hopping parameters,  $J \rightarrow J \exp\left(-ie/\hbar \int_{\vec{R}_i}^{\vec{R}_f} \vec{A} \cdot d\vec{l}\right)$ , where the line integral of the vector potential is along the classical path between the initial and final lattice points.

The same magnetic flux can also be created by the following set of gauge potentials,

$$\begin{aligned}\vec{A}_2(\vec{r}, t) &= -f_\tau(t)B_0y\hat{x}, \\ \Phi_2(\vec{r}, t) &= 0.\end{aligned}\tag{4.5}$$

The resulting Hamiltonian is

$$\begin{aligned}H_2(t) = & - J \left( a_1^\dagger a_2 + a_2^\dagger a_3 + a_2^\dagger a_5 + a_3^\dagger a_4 + a_6^\dagger a_1 + h.c. \right) \\ & - J \left( e^{-i2\pi\phi f_\tau(t)} a_4^\dagger a_5 + e^{-i2\pi\phi f_\tau(t)} a_5^\dagger a_6 + h.c. \right).\end{aligned}\tag{4.6}$$

The magnetic flux is static for  $t < 0$  and  $t > \tau$ , and the two Hamiltonians are related by a static gauge transformation in these time intervals. However, the Hamiltonians, during the ramping interval, are disconnected. The following third set of gauge potentials,

$$\begin{aligned}\vec{A}_3(\vec{r}, t) &= -f_\tau(t)B_0y\hat{x}, \\ \Phi_3(\vec{r}, t) &= \frac{B_0}{\tau}xy(\theta(t) - \theta(t - \tau)),\end{aligned}\tag{4.7}$$

provides the dynamical gauge invariance. Note that  $\theta(t)$  is the step function. The corresponding Hamiltonian has extra on-site terms in addition to  $H_2(t)$ ,

$$H_3(t) = H_2(t) + J \left[ 2\pi\phi\gamma a_5^\dagger a_5 + 4\pi\phi\gamma a_4^\dagger a_4 \right] (\theta(t) - \theta(t - \tau)).\tag{4.8}$$

Here  $\gamma = \frac{\hbar}{J\tau}$  is a dimensionless parameter, which controls the adiabaticity of the ramping of magnetic flux, i.e.  $\gamma \rightarrow 0$  indicates the absolute adiabatic limit.

The gauge dependence can be checked numerically. We prepare an arbitrary initial wavefunction under zero magnetic field. This initial function is time evolved by the two Hamiltonians,  $H_1$  and  $H_2$  in Eq.4.4, Eq.4.6. The magnetic flux ramping is initiated at  $t = 0$  and gets its final value at  $t = \tau$ . Time evolution is carried out by Cayley's form of the time evolution operator.

$$\mathcal{T} \exp\left(-\frac{i}{\hbar} \int_t^{t+\Delta t} \hat{H}(\tau) d\tau\right) \approx \frac{1 - iH\Delta t/2}{1 + iH\Delta t/2}.\tag{4.9}$$

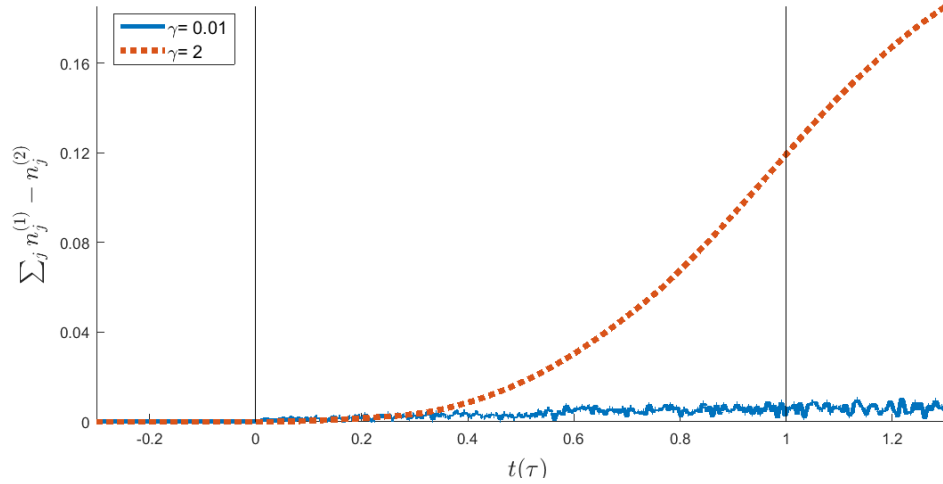


Figure 4.2: The total difference in the site densities of two wavefunctions separately evolved with  $H_1$  and  $H_2$  as a function of time. The initial wavefunctions are identical,  $\Psi_j^1(t=0)\Psi_j^2(t=0)$ , where  $j \in 1, \dots, 6$ . The magnetic flux is ramped from  $\phi = 0$  to  $\phi = 1/3$  within the time interval  $0 \leq t \leq \tau$  for two ramping parameters,  $\gamma = \{0.01, 2\}$ . For  $\gamma = 0.01$ , the ramping is almost adiabatic, as a result, the total difference in each site density is less than 0.01%. It is within our numerical accuracy. For  $\gamma = 2$ , the ramping is non-adiabatic and the evolutions of the same initial wavefunction for two Hamiltonians,  $|\psi_1(t)|^2$  and  $|\psi_2(t)|^2$  are distinct as a function of time.

If the time step  $\Delta t$  is much smaller than the average inverse energy within this interval,  $\hbar/\langle H(t) \rangle$ , a typical time scale of the system, then the evolution can be carried out comfortably.

We compare the density of each of the six lattice sites,  $\langle a_i^\dagger a_i \rangle$ , for three Hamiltonians as a function of dimensionless time. Recall that all the Hamiltonians are connected to each other by a static gauge transformation for  $t \leq 0$  and  $t \geq \tau$ , but only the first and third Hamiltonians are also related by a dynamical gauge transformation in the ramp interval,  $0 \leq t \leq \tau$ .

If the ramping parameter is close to the adiabatic limit,  $\gamma \ll 1$ , the differences in the density of each of the sites are so small within our numerical error, see Fig.4.2. It is because the effect of the lacking on-site potential connecting the two Hamiltonians is proportional to  $\gamma = \hbar/J\tau$ , and this value is negligible for the adiabatic limit. Another interpretation is that  $H_1$  and  $H_2$  are related by a unitary transformation  $U(t)^\dagger H_2(t) U(t) = H_1(t)$ , and the adiabatic limit indicates a negligible time dependence in the unitary transformation. On the contrary, for  $\gamma \gtrsim 1$ , the time evolution is non-adiabatic, the wavefunction evolved by  $H_2$ ,  $\Psi_2(t)$  is different from its counterparts evolved with  $H_1$  and  $H_3$ . This non-adiabatic evolution is shown in Fig.4.3 for  $\gamma = 2$ . Since the value of the missing on-site potential or the rate of change in the unitary transformation operator relating  $H_1$  and  $H_2$  is no longer negligible, the **static** gauge invariance is not correct any more. The third Hamiltonian,  $H_3$  includes the necessary on-site potential and re-establishes the **dynamical** gauge invariance between  $H_1$  and  $H_3$ .

In the opposite non-adiabatic limit, where  $\gamma \rightarrow \infty$ , the magnetic flux is simply quenched. It means, the first two Hamiltonians are equivalent by a static gauge transformation at all times except for  $t = 0$ . Even a comparably small non-adiabatic ramping parameter  $\gamma = 2$  leads to a distinct time evolution of site densities as seen in Fig.4.3. This difference is clearly due to the lack of the presence of a gauge transformation, consequently the lack of the on-site potential at  $t = 0$ . Even if the on-site potential is present within an infinitesimal amount of time,  $\tau \rightarrow 0$ , the magnitude scales at  $J\phi\gamma \sim 1/\tau$  and provides the gauge independence at  $t = 0$ . In a quench experiment scenario, hence, even if the

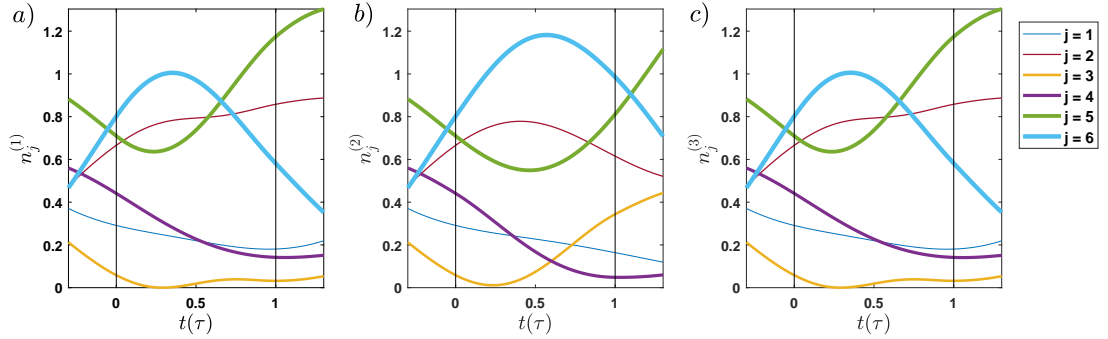


Figure 4.3: The non-adiabatic time evolutions of an arbitrary initial wavefunction in the minimal model, for  $\gamma = 2$ . Three plots show each site density  $\langle a_i^\dagger a_i \rangle$  for three Hamiltonians,  $H_i$  and  $i \in \{1, 2, 3\}$ . The evolution is carried out during the ramping of the magnetic flux from 0 to  $1/3$ .  $H_1$  (see Eq.4.4) and  $H_3$  (see Eq.4.8) are equivalent with a dynamical gauge transformation, and lead to identical time evolution, as in plot (a) and (c). The second Hamiltonian,  $H_2$  (see Eq.4.6) lacks the on-site scalar potential in artificial magnetic fields of synthetic lattice. Therefore, site densities are clearly different from the two other cases, as shown in (b).

Hamiltonians are equivalent up to a unitary transformation, the dynamical results are gauge dependent due to the discussed issue at  $t = 0$ .

Another way of interpreting the results are as follows, the magnetic flux quenches with two Hamiltonians lead to two different physical scenarios. Even if the resulting magnetic fields before and after the quench are equal, the resulting electric fields are different. This difference manifests itself for a quench scenario as a delta function potential at time  $t = 0$ , as seen in the third Hamiltonian. It is extremely hard to generate on-site delta potentials in cold atom experiments, and as a result, the artificial magnetic quench experiments will be gauge dependent.

## 4.2 Two-Leg and Three-Leg Ladders

This section investigates the quench dynamics for two- and three-leg ladders in an artificial magnetic field. Therefore, we work in  $\gamma \rightarrow \infty$  limit. In real-space lattices, the two-leg ladder in an artificial magnetic flux is experimentally

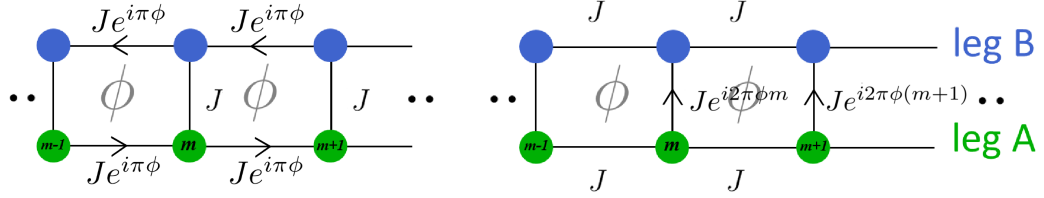


Figure 4.4: The two-leg ladder tight binding model illustration for Hamiltonians with two gauge potentials as in Eq.4.10 and Eq.4.17.

realized[50]. A magnetic flux quench scenario is highly challenging in such a system, but we consider a two-leg ladder for two reasons. Firstly, a two leg ladder has an analytical solution in a particular gauge choice and leads detailed interpretations. Secondly, it can be implemented in future experiments with effective spin-1/2 synthetic dimensions, probably utilizing dark states in spin-1 systems. A three-leg ladder, on the other hand, is formed as one dimensional lattice plus a synthetic dimension[45, 46]. It can be realized by coupling the hyperfine  $F = 1$  levels or three coupled levels of higher degeneracies.

In this section, the quenches are realized with initial eigenstates of the pre-quench Hamiltonian localized around a lattice momentum and forming a Gaussian shape. We analysed the dynamics of these single wavepackets as frequently done in bosonic systems or can be realized with filling the energy bands with Fermions.

Starting with the two-leg ladder, we obtain analytical properties of quenched systems for the gauge where the magnetic vector potential is perpendicular to the rungs of the ladder (see Eq.4.5 for  $\gamma \rightarrow \infty$ ). In this gauge choice, the hopping elements along the rungs are maintained, while the hopping elements along the infinite direction are modified with Peierls phases (see Fig.4.4). The corresponding Hamiltonian is,

$$\hat{H}_{2L}^{(1)} = -J \sum_{m=-\infty}^{\infty} (e^{i\pi\phi} a_{m+1}^\dagger a_m + e^{-i\pi\phi} b_{m+1}^\dagger b_m + b_m^\dagger a_m + H.c.) \quad (4.10)$$

where  $b_m a_m$  are annihilation operators for the leg B and A. Utilizing the translation invariance preserved in momentum space,

$$\begin{pmatrix} a_k^\dagger \\ b_k^\dagger \end{pmatrix} = \frac{1}{\sqrt{N}} \sum_{m=1}^N e^{ikm} \begin{pmatrix} a_m^\dagger \\ b_m^\dagger \end{pmatrix}, \quad (4.11)$$

the Hamiltonian is simplified and can be written as a sum of  $2 \times 2$  decoupled Hamiltonians at each lattice momentum in  $k$ -space:

$$\hat{H}_{2L}^{(1)}(k) = -2J \cos(k) \cos(\pi\phi) \hat{I} + \hat{h}(k) \cdot \sigma, \quad (4.12)$$

where  $\hat{h}(k) \cdot \sigma / J = -2 \sin(k) \sin(\pi\phi) \hat{\sigma}_z - \hat{\sigma}_x$ . The symbols  $\sigma_z, \sigma_x$  are spin Pauli matrices. This operator is readily diagonalized along the rotated spin-1/2 quantization axis,  $\sigma \cdot \hat{n}$ . The resulting energy bands, satisfying the eigenvalue equation  $\hat{H}_{2L}^{(1)}(k) |k, n; \phi\rangle = E |k, n; \phi\rangle$ , where  $n \in 1, 2$  are:

$$\frac{E^{1,2}(k)}{J} = -2 \cos k \cos(\pi\phi) \pm \sqrt{4 \sin^2 k \sin^2(\pi\phi) + 1}. \quad (4.13)$$

Note that each value of magnetic flux  $\phi$  and  $k$ -point corresponds to two eigenstates,  $|k, n; \phi\rangle$ , and the number of bands before and after the flux quench gives two bands. The resulting diagonalized operators at each  $(k, \phi)$  are,

$$\begin{pmatrix} \hat{\alpha}_k \\ \hat{\beta}_k \end{pmatrix} = \begin{pmatrix} \cos \theta_k^\phi / 2 & \sin \theta_k^\phi / 2 \\ -\sin \theta_k^\phi / 2 & \cos \theta_k^\phi / 2 \end{pmatrix} \begin{pmatrix} \hat{a}_k \\ \hat{b}_k \end{pmatrix},$$

with  $\tan \theta_k^\phi = \frac{1}{2 \sin k \sin(\pi\phi)}$ .

The initial wavepacket is created as a superposition of  $k$ -points around a specific lattice momentum,  $k_0$  for an initial magnetic flux  $\phi_1$ . Then it is quenched to the final magnetic flux  $\phi_2$  and we investigate the dynamical response of such a system. We choose the wavepacket in the lower band, with a group velocity of  $v_g \propto \partial E^1 / \partial k$ . This packet after the quench is distributed into two post-quench bands as a linear combination and the split packets will probably have two different velocities. The typical time for two packets to split spatially is determined by the spread of the initial packet. The weight of each packet is related to the overlap of the initial band with two post-quench bands. This overlap coefficient is simply written as,

$$C_{n_1, n_2}^{\phi_1, \phi_2}(k) = \langle k, n_1; \phi_1 | k, n_2; \phi_2 \rangle, \quad (4.14)$$

where  $n_1$  and  $n_2$  are the final and the initial band indices. These coefficients can be directly measured by in-situ density probes, and the analytical expression for

four possible combinations of the overlap coefficients are written as,

$$\begin{aligned}
C^{\phi_1, \phi_2}(k) &= \begin{pmatrix} \cos\left(\frac{\theta_k^{\phi_2} - \theta_k^{\phi_1}}{2}\right) & \sin\left(\frac{\theta_k^{\phi_2} - \theta_k^{\phi_1}}{2}\right) \\ -\sin\left(\frac{\theta_k^{\phi_2} - \theta_k^{\phi_1}}{2}\right) & \cos\left(\frac{\theta_k^{\phi_2} - \theta_k^{\phi_1}}{2}\right) \end{pmatrix}, \quad (4.15) \\
\cos\left(\frac{\theta_k^{\phi_2} - \theta_k^{\phi_1}}{2}\right) &= \frac{1}{2} \left( \sqrt{1 + \frac{b_2}{h_2}} \sqrt{1 + \frac{b_1}{h_1}} + \sqrt{1 - \frac{b_2}{h_2}} \sqrt{1 - \frac{b_1}{h_1}} \right), \\
\sin\left(\frac{\theta_k^{\phi_2} - \theta_k^{\phi_1}}{2}\right) &= \frac{1}{2} \left( \sqrt{1 - \frac{b_2}{h_2}} \sqrt{1 + \frac{b_1}{h_1}} - \sqrt{1 + \frac{b_2}{h_2}} \sqrt{1 - \frac{b_1}{h_1}} \right),
\end{aligned}$$

where  $b_i = -2 \sin(k) \sin(\pi \phi_i)$  and  $h_i = \sqrt{4 \sin^2 k \sin^2(\pi \phi_i) + 1}$ . Note that  $|C_{1,2}^{\phi_1, \phi_2}|^2(k)$ , for example means that the probability for an initial state of the lower band at lattice momentum  $k$  under magnetic flux  $\phi_1$  to jump to the second band of the new system at  $\phi_2$  at the same lattice momentum. Note that the lattice momentum is a conserved parameter in the system, and a flux quench does not affect this value.

If the gauge choice is along the rungs (see Eq.4.3 for  $\gamma \rightarrow \infty$ ), the Hamiltonian can at most be reduced to a  $q \times q$  matrix for a magnetic flux with  $\phi = p/q$ , and the system is described by  $q$  bands within the magnetic Brillouin zone. This system can only be solved and time evolved numerically. Therefore, to compare the two gauge choices, we create a wide enough two-leg ladder and form a Gaussian wavefunction around the lattice momentum  $k = k_0$ ,

$$\psi_0(m) = \frac{1}{(\pi \Delta^2)^{1/4}} e^{-\frac{(m-m_0)^2}{2\Delta^2}} e^{ik_0 m}. \quad (4.16)$$

The width in each long chain along the  $x$ -axis is  $\Delta = 60$  and centred in the middle of the lattice system whereas the whole system has 1200 sites in each chain, and the pre-quench flux is zero. Note that the wavepacket is localized enough in the lattice momentum space so that the constituent  $k$ -modes cannot disperse to form separate packets in the total time scale of the pre- and post-quenching process. The initial wavepacket is,

The initial pre-quenched wavepacket at  $k_0 = \pi/4$  is evolved in time with two quenched Hamiltonians at  $\phi_2 = 1/6$  in two gauge choices. As shown in Fig.4.5, the post-quench energy bands are the slightly deformed version of the zero field bands, and the group velocities at each lattice momentum value are also different.

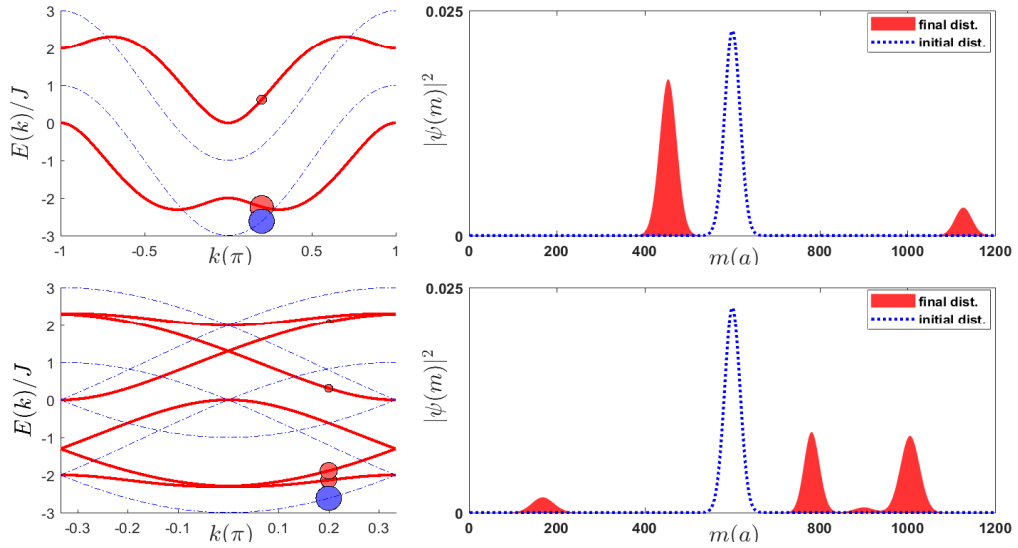


Figure 4.5: The post-quench dynamics of the initial wavepacket for the two gauge choices in Eq.4.3 and Eq.4.5 for  $\gamma \rightarrow \infty$ . The initial packet is prepared under zero magnetic flux at the lattice momentum  $k = 0.2\pi$ . The artificial magnetic flux is quenched as  $\phi = 0 \rightarrow 1/3$ . The upper plot shows the gauge in Eq.4.5, the initial wavepacket is divided into two packets moving in opposite directions, while in the gauge of Eq.4.3, in the lower plot, the initial wavepacket splits into four packets with different velocities. Note that the blue dashed curves are the pre-quench bands on the left and the initial wavepacket on the right. Similarly, the red curves are the post-quench bands on the left and the red filled curves are the final distribution of the wavefunction long after the quench. Lastly, the distribution of the initial and the final packets are sequentially shown with blue (dark grey) and red (grey) filled circles on the corresponding energy bands on the left lower and upper plots.

The initial wavepacket splits into packets with different velocities along the same direction. The numerical and analytical results are compared for the weight of the packets after the quench. Total weights of each packet after the quench are numerically found as  $P_1 = 0.91$  and  $P_2 = 0.09$ , and they are in perfect agreement with the analytical coefficients  $|C_{11}|^2 = 0.91$  and  $|C_{12}|^2 = 0.09$ , where the error is less than 0.2 percent.

The dynamical response of the flux quench can be dramatic if the post-quench bands at each lattice momentum mostly have velocities in opposite directions. For example, in Fig.4.5, we quench the initial wavepacket at  $k = \pi/5$  as  $\phi = 0 \rightarrow 1/3$ . The initial packet splits into a right- and two left-moving two packets for the

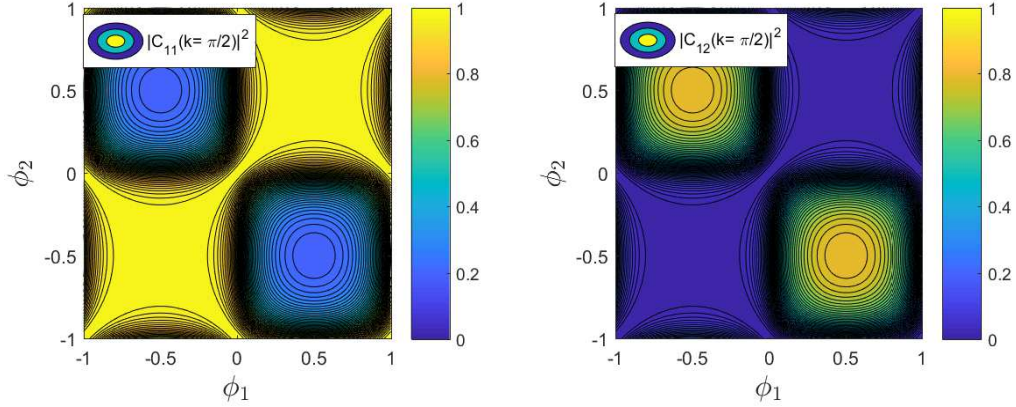


Figure 4.6: The weight of each packet after a quench between two arbitrary magnetic fluxes,  $\phi_1$  and  $\phi_2$ , see Eq.4.15. The initial packet is prepared around the lattice momentum  $k = \pi/2$  of the lowest band. The left plot shows the weight remaining in the first band,  $|C_{11}(k = \pi/2)|^2$  as a function of  $\phi_1$  and  $\phi_2$ . The right plot is the weight transferred to the upper band after the quench,  $|C_{12}(k = \pi/2)|^2$ .

gauge choices in Eq.4.5. The weight of each packet are theoretically calculated in Eq.4.15 and they match with the numerical time evolution. In this system, the lattice momentum is a conserved quantity while the canonical momentum is not. This can be explained as the result of the induced electric field at the moment of the quench at  $t = 0$ , as discussed in the previous section.

In Fig.4.6, we calculate the re-distribution of an initial wavepacket prepared at lattice momentum  $k = \pi/2$  of the lowest band of initial magnetic flux  $\phi_1$  on new bands at arbitrary final flux  $\phi_2$  as calculated in Eq.4.15. The coefficients,  $|C_{11}(k)|^2$  and  $|C_{12}(k)|^2$  are symmetric for their complementary part. They indicate the post-quench weights of two wavepackets created. The initial packet is preserved by a significant amount (more than seventy percent) if the pre- and the post-quench magnetic flux values are close to an integral value.

The Hamiltonian  $H_{2L}^{(1)}$  with the gauge choice is easier to implement since it preserves the translational symmetry and does not change the size of the Brillouin zone and the number of the bands. However, this Hamiltonian is not unique to describe the magnetic flux. Another gauge choice in a two-leg ladder can be, as seen in Fig.4.4 (b), the vector potential along the rungs of the lattice such

that the Peierls phases modify the hopping element of the rungs. Corresponding Hamiltonian is,

$$\hat{H}_{2L}^{(2)} = -J \sum_{m=-\infty}^{\infty} (a_{m+1}^\dagger a_m + b_{m+1}^\dagger b_m + e^{i2\pi\phi m} b_m^\dagger a_m + H.c.). \quad (4.17)$$

The most distinctive feature of two Hamiltonians is that  $H_{2L}^{(1)}$  commutes with the discrete translation operator along the  $\hat{x}$ -axis while  $H_{2L}^{(2)}$  does not. Hence, for the rational values of  $\phi = p/q$ , the first Hamiltonian still has two bands uniquely extending in the Brillouin zone  $-\pi < k < \pi$ , and the two bands of the zero field in the second Hamiltonian fractures into  $2q$  bands confined into the magnetic Brillouin zone,  $-\pi/q < k < \pi/q$ . Note that these two descriptions are totally equivalent, and one can fold the energy bands of  $H_{2L}^{(1)}$  into the magnetic Brillouin zone and validates the equivalence.

It is crucial to determine the observable effects of the gauge choice, and we have already discussed the dynamical behaviour of the Gaussian wavepackets after magnetic flux quenches having distinct properties. In this respect, we can track the number of packets for most of the quench scenarios. We take an initial Gaussian wavepacket created in the lowest band of the zero-field two-leg ladder Hamiltonian, and it is localized around a specific lattice momentum. A quench to  $H_{2L}^{(1)}$  results in two split wavepackets irrespective of the value of the magnetic flux. It is because the system preserves the translational symmetry along the infinite leg, and each packet possesses the same lattice momentum. The same quench to  $H_{2L}^{(2)}$  would break the translational symmetry mixing  $2q$  sites, and it is natural to expect  $2q$  wavepackets. I might be tempted to expect larger and larger number of packets as the denominator of the magnetic flux  $\phi = p/q$  is increased. However, in the extreme limit of an irrational value of the magnetic flux, it would be absurd to expect infinite number of packets. Although there would be a large number of bands in the quenched system, the number of bands do not control the number of subsequent packets. It is because  $H_{2L}^{(2)}$  is not arbitrary and connected to the translational invariant  $H_{2L}^{(1)}$  by a unitary transformation.

$$H_{2L}^{(2)} = U^\dagger H_{2L}^{(1)} U, \quad (4.18)$$

and this restricts the connected bands before and after the quench. The unitary

operator is

$$U = e^{i\pi\phi \sum_m m(a_m^\dagger a_m - b_m^\dagger b_m)}. \quad (4.19)$$

Consider an eigenstate of the ladder at zero magnetic field,  $|\psi_k(0)\rangle$ , the time evolution of the quenched state with  $H_{2L}^{(1)}$  is,

$$|\psi_k(t)\rangle_1 = e^{-iH_{2L}^{(1)}t/\hbar}|\psi_k(0)\rangle. \quad (4.20)$$

It includes the linear combination of two components at the same lattice momentum  $k$ . We seek for the number of modes evolving with different frequencies when the initial eigenstate is quenched to  $H_{2L}^{(2)}$ .

$$|\psi_k(t)\rangle_2 = e^{-iH_{2L}^{(2)}t/\hbar}|\psi_k(0)\rangle. \quad (4.21)$$

Recalling the static gauge equivalence in Eq.4.18, Eq.4.21 can be rewritten as,

$$|\psi_k(t)\rangle_2 = U^\dagger e^{-iH_{2L}^{(1)}t/\hbar}U|\psi_k(0)\rangle. \quad (4.22)$$

Let us examine the effect of two terms in this expression. The first unitary operator,  $U^\dagger$  introduces a complex phase at each site but the real space density does not change as well as the number of packets since  $U^\dagger$  is time independent. The remaining term is the time evolution of  $U|\psi_k(0)\rangle$  with  $H_{2L}^{(1)}$ . This picture has an advantage, because  $H_{2L}^{(1)}$  splits any function into at most two more components. Now let us count the number of modes in  $U|\psi_k(0)\rangle$ . The eigenket  $|\psi_k(0)\rangle$  is shifted to the eigenkets at lattice momentum  $k \pm \pi\phi$ , hence there are  $q$  modes that would be mixed as a result of the  $q$ -fold degeneracy in the Brillouin zone. In short, a magnetic flux quench of an initial packet at zero field creates four packets with different velocities. In a specific example, consider an initial wavepacket at  $k = 0.2\pi$  (see Fig.4.5), it splits into two packets as it is quenched to  $H_{2L}^{(1)}$ , while the number of packets is four as it is quenched to  $H_{2L}^{(2)}$ .

The two-leg ladder system is a useful analytically solvable model to understand wider ladders, and it can be implemented with optical lattices[50]. However, a magnetic flux quench scenario is not easy to achieve, because the artificial magnetic flux is created by the overlap of off-site Wannier functions as a result of Raman assisted tunneling. Therefore, one must change the difference in laser wave vectors, which is not an easy task. A magnetic flux quench in three-leg

ladder in a similar realization is also difficult. Another way of implementing the artificial gauge field is to couple the hyperfine levels of the atoms by Raman lasers and modify the hopping parameter by the laser intensity and the effective Peierls phase by the detuning between the hyperfine levels. Hence, wider leg ladders can be implemented in this synthetic dimension along with an artificial gauge field. Moreover, these changes can be carried out at a fast time scale.

We investigate an artificial magnetic field quench in a three-leg ladder, which can be created by coupling three hyperfine levels and creating spin-1 manifold along the synthetic dimension. Similar to the two-leg ladder, we propose two (statically equivalent) Hamiltonians describing a quantum particle in the three-leg system with a magnetic flux  $\phi$  within each plaquette. In the first Hamiltonian, the Peierls phases are again imprinted along the infinite legs,

$$\hat{H}_{3L}^{(1)} = -J \sum_{m=-\infty}^{\infty} (e^{i2\pi\phi} a_{m+1}^\dagger a_m + b_{m+1}^\dagger b_m + e^{-i2\pi\phi} c_{m+1}^\dagger c_m + b_m^\dagger a_m + c_m^\dagger b_m + H.c.). \quad (4.23)$$

where  $a_m$ ,  $b_m$  and  $c_m$  are the annihilation operators for leg A, B and C. The second Hamiltonian has these hopping phases along the synthetic dimension

$$\hat{H}_{3L}^{(2)} = -J \sum_{m=-\infty}^{\infty} (a_{m+1}^\dagger a_m + b_{m+1}^\dagger b_m + c_{m+1}^\dagger c_m + e^{i2\pi\phi m} b_m^\dagger a_m + e^{i2\pi\phi m} c_m^\dagger b_m + H.c.). \quad (4.24)$$

Two Hamiltonians are connected by a unitary (static gauge) transformation,

$$U = e^{i2\pi\phi \sum_m m (a_m^\dagger a_m - c_m^\dagger c_m)}, \quad (4.25)$$

and the corresponding two energy spectra are equivalent albeit with folded energy bands in the reduced Brillouin zone for  $\hat{H}_{3L}^{(2)}$ . We plot each spectrum by blue and red colors for  $\phi = 0$  and  $\phi = 1/4$  respectively, as shown in Fig.4.7.

We calculated the quenched distribution of all the initial eigenstates prepared at each lattice momentum of the lowest band of the zero magnetic field Hamiltonian ( $\phi_1 = 0$ ) within the Brillouin zone for two gauge choices. Each eigenstate is quenched to two Hamiltonians in Eq.4.23 and Eq.4.24 as seen in Fig.4.7. The initial packets are denoted with blue dots and the quenched distributions with their weights are with red dots with different sizes. One thing to notice is that

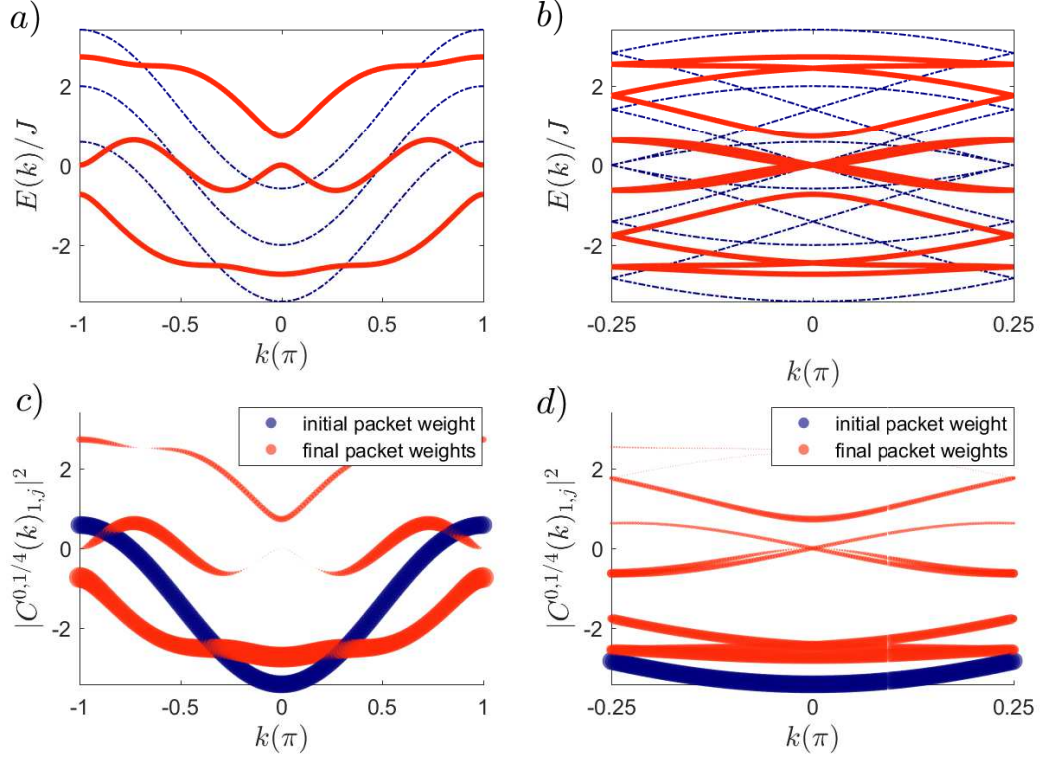


Figure 4.7: The pre-quench and the post-quench energy band structures and the packet weights on each band after the quench. Plot *a* and *b* show the pre- ( $\phi = 0$ ) and post-quench ( $\phi = 1/4$ ) energy bands for two gauge choices with dashed blue lines and red solid lines. The plot *c* (*d*) shows the weight of the initial packet in each lattice momentum of the lowest band of zero field Hamiltonian on the new energy bands at  $\phi = 1/4$ . All initial wavepackets are in the lowest bands and the thickness of blue line is same at each  $k$ -point. After the quench, these wavepackets are re-distributed at each  $k$ -point into new bands with different thickness (weight) in the gauge choice 2 (1). Focusing the first gauge choice, (see Eq.4.3), the initial packet prepared within the reduced Brillouin zone at lattice momentum is distributed into nine bands. The connection (see Eq.4.25) between the two Hamiltonians, 4.23 and 4.24 constraints the largest number of packets that initial packets can divide into, which is the square of the number of legs  $3 \times 3 = 9$ .

the energy bands are equivalent up to a folding procedure. It is also seen clearly that the number of the resulting packets are different in each gauges, and it cannot simply be explained by the folding of the bands into the reduced Brillouin zone. Just like the selection rules, the unitary transformation relating the two Hamiltonians in Eq.4.25 restricts the allowed bands and the number of packets. For the case of  $\phi_2 = 1/4$ , just as in the two-leg ladder,  $\hat{H}_{3L}^{(2)}$  breaks the translational invariance mixing  $2 \times 4 = 8$  sites, and the translational symmetry is recovered by a translation of four lattice sites. Therefore, the magnetic Brillouin has  $3 \times 4 = 12$  bands. It is exciting to see that the initial packet splits into  $n^2 = 9$  bands in contrast to the common expectation as twelve packets. Again, the static gauge connection (see Eq.4.25) of  $\hat{H}_{3L}^{(2)}$  with the translational invariant Hamiltonian  $\hat{H}_{3L}^{(1)}$  puts an upper bound for the number packets that can be created after any magnetic flux quench. For an  $n$ -leg ladder, this finding can be generalized as the eigenstates at each lattice momentum of resulting  $n$  bands under zero field are coupled at most with  $n$  eigenstates within the Brillouin zone, and there are  $n^2$  resulting packets after the quench as  $\phi = 0 \rightarrow p/q$ .

In an example, we take one sample from the post-quench distribution of plot (a) and (b) of Fig.4.7 as the system is quenched as  $\phi = 0 \rightarrow 1/4$ . We consider an initial wavepacket created around the lattice momentum  $k = 0.15\pi$  with large blue dots in Fig.4.8. On the left plots of (a) and (b), post-quench packets are denoted with red dots with different size proportional to their weights. In plot (a), the quenched Hamiltonian,  $\hat{H}_{3L}^{(1)}$  preserves the translational symmetry and the expectation is that the packet will split into three. It is clearly seen that, the initial packet splits at most 2 packets, whereas this number is verified to be 8 for  $\hat{H}_{3L}^{(1)}$  which is less than nine. The right plots of (a) and (b) show the pre- (dashed blue) and post-quench (solid red) total density of each site, where the density of the synthetic dimensions is traced out. The number, weights and velocities of the packets are strikingly different and underline the gauge dependence in quench scenarios.

The synthetic dimension experiments have the advantage of the full control over the tunneling amplitudes and the complex phases imprinted on each element. However, all these experiments are readily implemented with the second

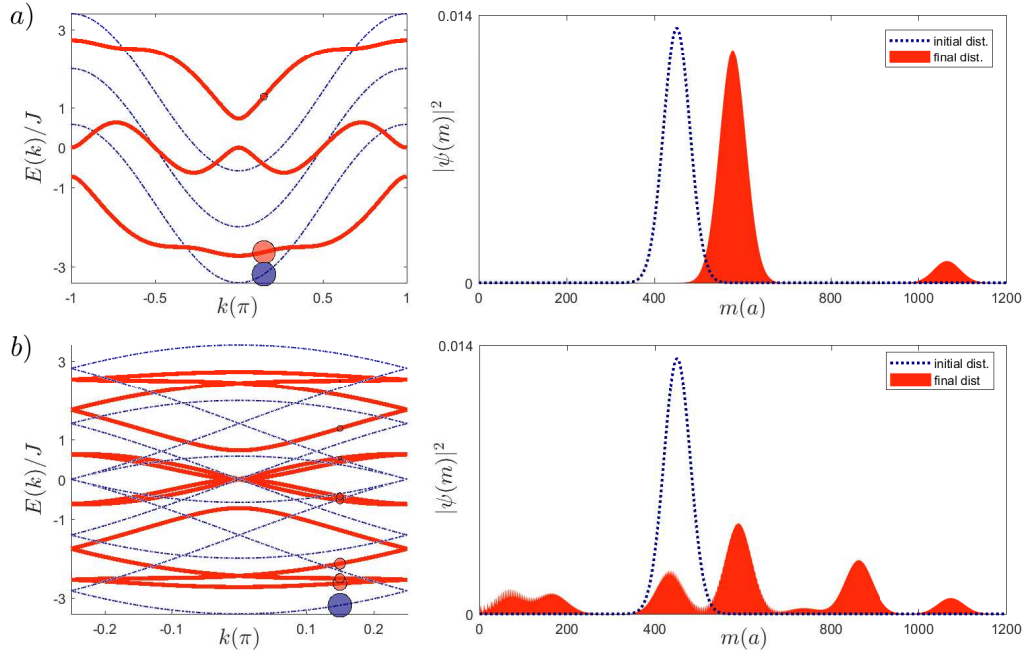


Figure 4.8: Time evolution of the wavepacket sample extracted from Fig.4.7 at the lattice momentum  $k = 0.15\pi$ . The initial packet is a zero field Gaussian function which is localized around at  $k = 0.15\pi$ . (a) Flux quench  $\phi = 0 \rightarrow 1/4$  in the first gauge choice creates two packets independent of the denominator of magnetic flux  $q = 4$ , which is against common expectation. The blue and red dots on the left plot show the weights of packets before and after the quench. (b) The same flux quench in the second gauge choice: Creates eight packets with different weights and velocities. The amount of packets are in accordance with our upper limit,  $3 \times 3 = 9$ , as expected.

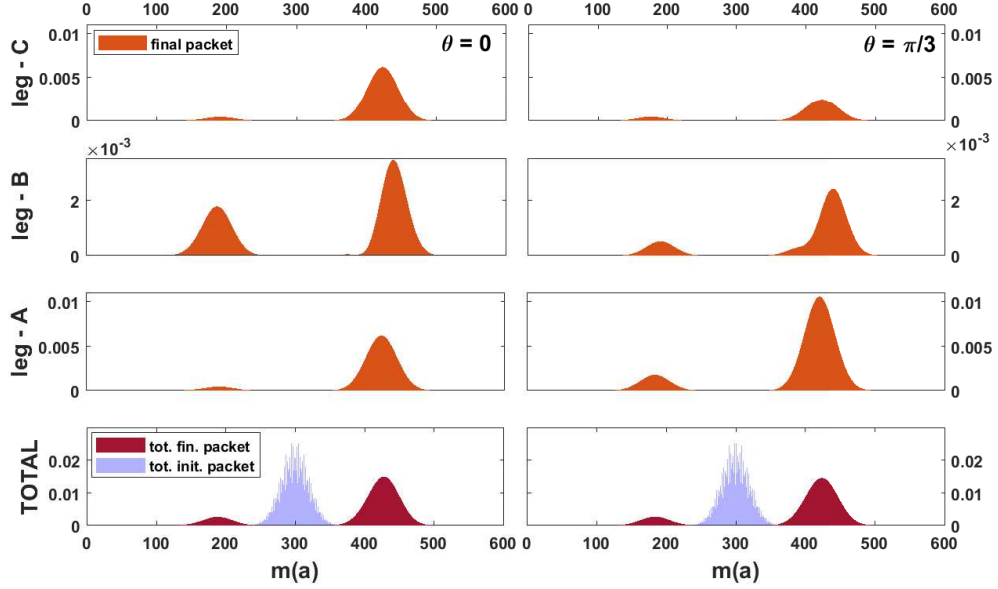


Figure 4.9: The time evolution of the density at each leg for the quench  $\phi = 1/2 \rightarrow 0$ . The initial packet is prepared around an eigenstate of  $H_{3L}^{(2)}$  under  $\phi = 1/2$  at  $k_0 = 0.15\pi$  and is quenched to  $H_{3L}^\Theta$  for the gauge angles,  $\Theta = 0$  and  $\Theta = \pi/3$ . The difference in each leg is because of the absence of an induced electric field  $\frac{\Theta}{a}\delta(t)$  needed for the dynamical gauge equivalence. Notice that the total density is same for both gauge angles.

Hamiltonian,  $H_{3L}^{(2)}$ . In this respect, it is useful to further examine quench scenarios with the first gauge choice in synthetic dimensions. We introduce another Hamiltonian, having zero flux per plaquette but the Peierls phases along the rungs (synthetic direction) are non-zero and equal to a phase angle  $\Theta$  due to a constant vector potential,

$$\hat{H}_{3L}^\Theta = -J \sum_{m=-\infty}^{\infty} (a_{m+1}^\dagger a_m + b_{m+1}^\dagger b_m + c_{m+1}^\dagger c_m + e^{i2\pi\Theta} b_m^\dagger a_m + e^{i2\pi\Theta} c_m^\dagger b_m + H.c.). \quad (4.26)$$

All possible Hamiltonians for  $\Theta \in [0, 2\pi)$  are equivalent by a trivial gauge transformation. Under an arbitrary constant vector potential, a coordinate shift of  $a\Theta/2\pi$ , where  $a$  is the lattice constant along the synthetic dimension, takes care of the necessary transformation.

We take two scenarios for an eigenstate of  $\hat{H}_{3L}^{(2)}$  with  $\phi$  at lattice momentum  $k = 0.3\pi$ , where it is quenched to  $\hat{H}_{3L}^\Theta$  for  $\Theta = 0$  and  $\Theta = \pi/3$ . As seen in Fig.4.9,

in both scenarios, the initial packet is divided into three packets, which is a natural result for zero field final Hamiltonian, and each packet possesses the same amount of contribution to the weight. However, they have the same velocity, and it not possible to distinguish these contributions. In that regard, the total weights along the synthetic dimension are identical in two gauge angles, and they are actually independent of the angle,  $\Theta$ . On the other hand, we have another observable quantity, the population of each hyperfine level. In our system, the density of each packet along the synthetic dimension is found to depend on the phase angle. To further visualize it for each of two  $\Theta$  values, we take two snapshots of the the pre- and post-quench distributions of the hyperfine densities in leg-A, leg-B and leg-C (see Fig.4.9). It elegantly shows that even if the cumulative densities along the synthetic dimension on each site are identical for  $\Theta = 0$  and  $\Theta = \pi/3$ , the hyperfine distribution of each packet are different at each time slice.

Even a trivial difference in gauge potentials makes an observable difference in flux quenches. One should be aware that a quenching of a finite magnetic flux as  $\phi = p/q \rightarrow 0$  with the phase angle  $\Theta$  lacks the scalar potential at the instant of quench to re-establish the gauge equivalence of all  $H_{3L}^\Theta$ . This potential would lead to an electric field impulse  $\frac{\Theta}{a}\delta(t)$  proportional to the magnitude of  $\Theta$ . It means that a turn-off in magnetic flux at each phase angle would have different electric field impulses along the synthetic dimension. Hence, the cumulative density along the synthetic dimension does not change, but the hyperfine density is clearly modified for each  $\Theta$  value.

### 4.3 Wide ladders and the robustness of the edge states

Synthetic dimensional systems are limited in realizing the large extended systems, but utilizing larger nuclear spins we can obtain a good approximation two its two-dimensional spatial counterpart. The latest cold atom experiments, in this respect, are done with large nuclear spins as  $I = 7/2, 9/2$ [46] and are well capable

to simulate strongly correlated systems. We investigate the flux quenches in fifteen leg ladder system and compare with the continuum strip.

In a wide lattice with magnetic flux, a large wavepacket created around a momentum eigenstate undergoes to a semi-classical motion, and it has following two properties. Firstly, the center of mass of the packet is modified by the Lorentz force due to the magnetic flux, and in the wave picture creates a non-trivial Berry curvature. Secondly, the weighted summation around a momentum eigenstate results in the broadening of the packet. The first property, semi classical center of mass motion can be used to examine the underlying artificial magnetic field[51]. A magnetic flux quench will lead the semi-classical center of mass motion with a velocity kick due to the Lorentz force. In the lattice picture, a flux quench can drastically affect the Gaussian profile since the packet will be distributed to other bands with different velocities and weights as in the case of few-leg ladders.

For this purpose, we consider a fifteen-leg ladder with magnetic flux. The energy spectrum as a function of the flux (see Fig.4.10) is reminiscent of the energy spectrum of the two dimensional infinite lattice, which is known as the Hofstadter butterfly. The difference comes with the existence of the edge states residing the in energy gaps of the infinite lattice butterfly. First of all, we analyse the flux quench as  $\phi = 0 \rightarrow 1/3$  for an initial wavepacket whose width is five lattice sites along synthetic dimension and fifteen sites along the legs with an initial momentum in the same direction. We find the post-quench wavepacket splits into smaller packets and the finite edges causes a complicated evolution, as a result the initial packet dissolves into the bulk. The initial wavepackets created from the bulk states are investigated for quench parameters and gauge scenarios and no interesting behavior is found.

The edge states are robust thanks to the bulk edge correspondence if the bulk system has a topological invariant. In this regard, we wonder whether the robustness is preserved under an artificial flux quench. Generally speaking, we cannot expect the topological protection of these states as these invariants are possible to change leading different class of topological phases under flux changes as partially discussed in Chapter3 and more detailly discussed as an adiabatic

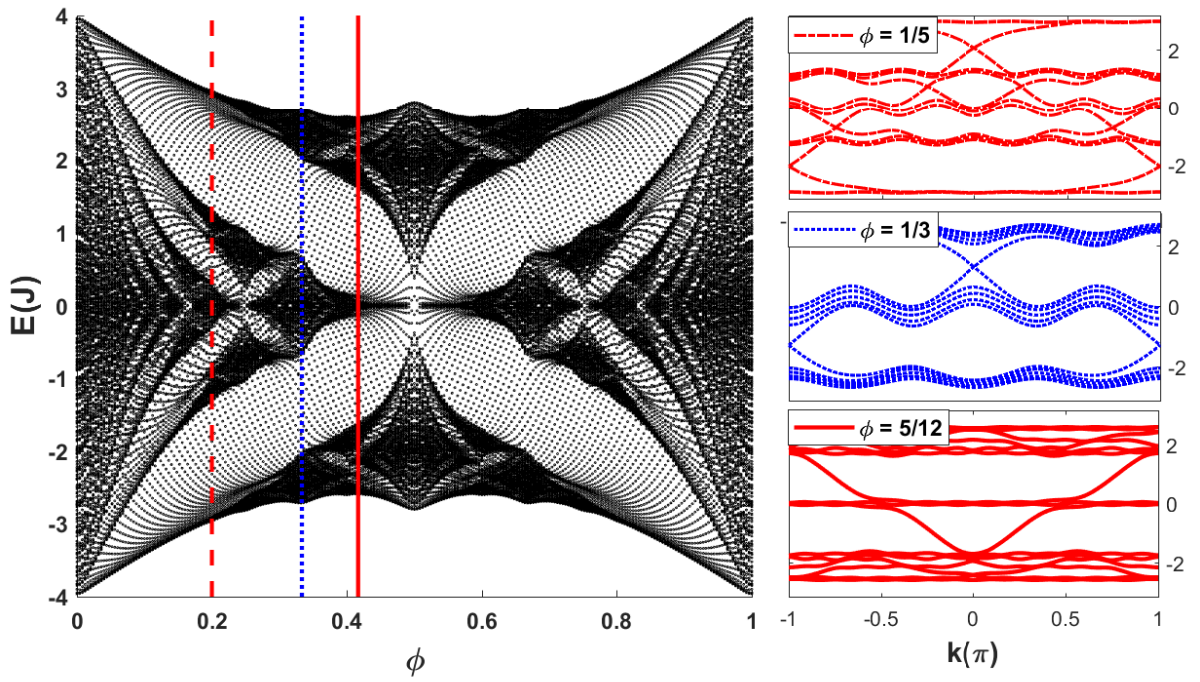


Figure 4.10: The energy spectrum of the fifteen-leg ladder are shown with 51 points in the momentum space as a function of the magnetic flux,  $\phi$ . The number of lattice site is infinite and the gauge choice is the LAndau gauge parallel to the legs. This spectrum is reminiscent of the Hofstadter butterfly as the density of states are equivalent in the  $n \rightarrow \infty$  ladder limit. In our flux quench scenarios, we take three slice of energy bands at  $\phi = 1/5, 1/3, 5/12$  and create wavepackets at edge state modes. Corresponding edge modes live within the energy gaps.

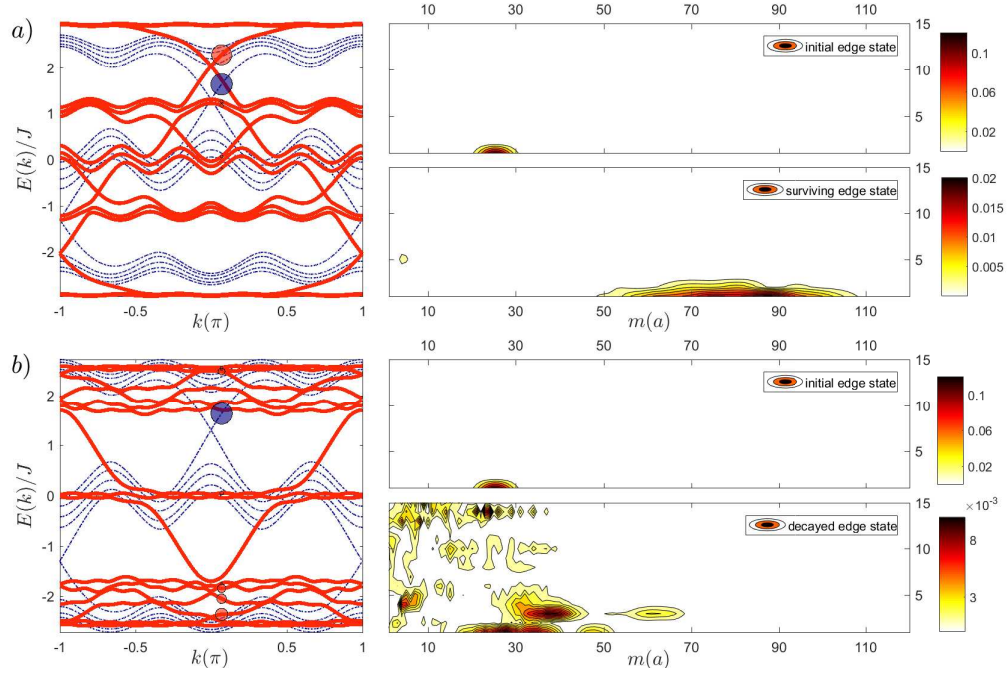


Figure 4.11: Time evolution of the edge state packets which are extracted in Fig.4.10 for two different flux quenches. (a)  $\phi = 1/3 \rightarrow 1/5$  (b)  $\phi = 1/3 \rightarrow 5/12$ . The initial packet in both cases are created around the lattice momentum  $k = 0.07\pi$  at the magnetic flux  $\phi = 1/3$  and it is quenched to  $\phi = 1/5$  and  $\phi = 5/12$ . The plots on the left are the energy bands before (blue dashed lines) and after (red solid lines) the quench, and the initial and the final distribution of the packets are denoted on the band diagram with blue and red large dots, respectively. The same initial edge state is observed to survive and decay in two flux values. Two plots on the right are the snapshots of the packets for pre- and post-quench. As clearly seen, the magnetic flux quench for the case  $\phi = 1/3 \rightarrow 1/5$ , results in the survival of the edge state with its 88 percent. The same packet decays into the bulk for the case  $\phi = 1/3 \rightarrow 5/12$  as it is roughly uniformly distributed into all bulk states.

change of flux in our previous work[18]. Moreover, it has been recently shown that the topological invariants in the equilibrium can be extracted from dynamics[52, 53] in two band systems. We answer this question by observing if an initial edge state preserves its form and the topological invariant or dissolves into the bulk after a flux quench. We obviously observe both behaviors. First of all, when the edge packets created at a finite flux are quenched to zero field, the edge states disappears in the bulk as there are no edge state present in our model. We can also claim that a small perturbation of the flux does not disturb the edge state.

The decay and survival of the edge states under a magnetic flux quench are plotted in Fig.4.11. After the quench, the edge state survives only if there is another edge state living in the same energy gap. In a specific example, we consider three energy bands as calculated in Fig.4.10, and prepare the edge state wavepackets at the lattice momentum  $k = 0.07\pi$  in one of the three magnetic fluxes,  $\phi_1 = 1/3$ . The flux quench,  $\phi = 1/3 \rightarrow 1/5$ , preserves 88% of the initial edge state as the edge state of the new Hamiltonian at  $\phi = 1/5$ . The same cannot be said of the flux quench,  $\phi = 1/3 \rightarrow 5/12$  where the edge state uniformly disperses into the bulk modes.

As the last part of this section, we consider flux quenches in a continuum strip and compare the dynamics of wavepackets with wide ribbon case. This strip has a length of  $L$  along the  $\hat{x}$ -axis and infinite along  $\hat{y}$ -axis. The corresponding Hamiltonian is,

$$\mathcal{H}_{strip} = \frac{1}{2} \left( \vec{p} - \vec{A} \right)^2 + V(x, y), \quad (4.27)$$

where

$$V(x) = \begin{cases} 0 & : 0 < x \leq L; \quad -\infty < y < \infty \\ \infty & : x < 0, x > L \end{cases} \quad (4.28)$$

All length parameters are non-dimensionalized with  $\ell_0 = \sqrt{\hbar/m\omega_c}$ , and all energies are with  $E = \hbar\omega_c$ , where  $\omega_c = eB_0/m$ . We choose the vector potential in  $\hat{y}$ -direction such that the system maintains the translational invariance in this direction for quench scenarios. The vector potential is the Landau gauge

$$\vec{A}_1 = x\hat{y}. \quad (4.29)$$

We are working in the high magnetic field limit such that the magnetic length  $\ell_0$  is

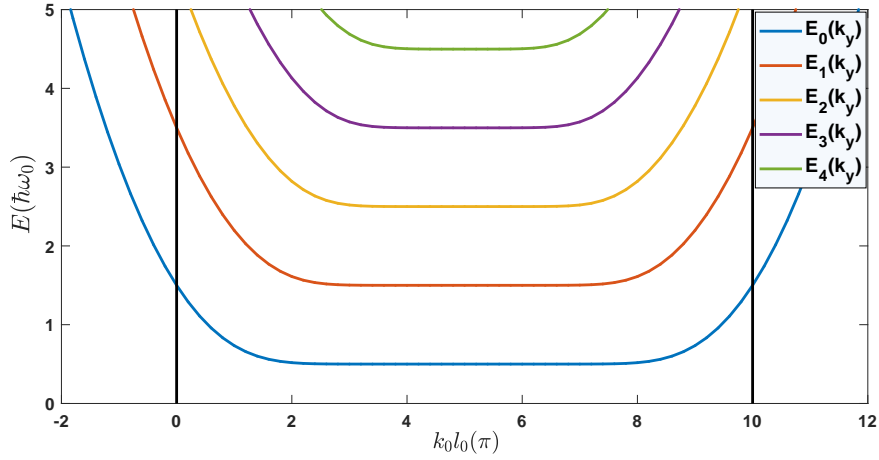


Figure 4.12: The single particle energy spectrum of a continuous strip under constant magnetic field. The particle is confined to  $0 < x < L = 10$ . There are two types of eigenstates in the system. The degenerate levels are the first type, the bulk Landau levels, and they consist of equally separated plateaus. The second type of eigenstates are the edge states, and their guiding center,  $x_g = k_y$  is out of the strip and consequently the matter waves are squeezed to the edges. The energy of the edge states change as a function of  $k_y$ .

much smaller than the width of the strip. There are two reasons for this: Firstly, we do not desire the bulk states get affected by the presence of the edges, secondly, the behavior of the edge states can be isolated to single edge scattering problem. Under these assumptions, we quench the magnetic field in the same gauge choice. The canonical momentum along  $\hat{y}$ -axis is conserved under such a quench and it determines the guiding center of the Landau levels in  $\hat{x}$ -axis,  $x_g = k_y$  (in units of  $\ell_0$ ). We calculate the energy spectrum of Landau level particles confined in  $\hat{x}$ -axis as a function of guiding center,  $x_g$ . As seen in Fig.4.12, the energy states can be grouped into two groups. The ones with guiding center residing in the bulk and the states whose guiding center is out of the strip at least by few times the magnetic length,  $\ell_0$ . The first group of eigenstates are the Landau levels forming wide plateaus as degenerate bulk states, and the second group are the quantized edge states residing at two edges, where their energies change as a function of the guiding center or the momentum in the  $\hat{y}$  direction.

Back to the quench problem, we claim the gauge choice is again significant in the dynamics of the wavepackets in continuous system, and prove it by wavepacket

creating a wavepacket in the bulk. The packet is a superposition of all bulk states of the lowest Landau level,

$$\psi(x, y) = \frac{1}{\sqrt{\Delta}\sqrt{\pi}} \int_{-\infty}^{\infty} dk_y e^{-\frac{(k_y - k_0)^2}{2\Delta^2}} \Psi_{0, k_y}(x, y), \quad (4.30)$$

$$\Psi_{0, k_y}(x, y) = \frac{e^{ik_y y} e^{-(x - k_y)^2/2}}{\sqrt{2\pi} \pi^{1/4}}, \quad E_{0, k_y} = 1/2. \quad (4.31)$$

Note that the center of the packet is determined by the expectation value of the canonical momentum in the  $y$  direction,  $\langle \vec{x} \rangle = (k_0, 0)$ . The packet widths are given as  $\langle x^2 \rangle = 1 + \Delta^2$  and  $\langle y^2 \rangle = (1 + \Delta^2)/\Delta^2$ . The packet is stationary as formed by the lowest Landau levels and still an eigenstate of the Hamiltonian.

We consider a quench scenario, where the magnetic field does not change at all, but the vector potential is simply shifted by a finite amount as,

$$\vec{A}_2 = (x - d)\hat{y}, \quad (4.32)$$

where  $d$  is the amount of the shift. In this new gauge choice, even if the initial and the final magnetic fields are the same, this packet is not static any more. The gauge choices are connected by a static gauge transformation, and still the lack of the scalar potential at the instant of the quench prevents the stationary behavior of the initial packet. Instead, it fails to compensate for the shifted kinetic energy in the kinetic momentum term and provides a momentum kick on the packet. The time evolution is calculated as a coherent state of the quenched Hamiltonian is,

$$\begin{aligned} \psi(x, y, t) &= e^{-i\omega_c t/2} e^{-\frac{d^2}{4}(1 - e^{-2i\omega_c t})} \frac{1}{\sqrt{\pi}} \sqrt{\frac{\Delta}{1 + \Delta^2}} \\ &\times e^{i \left[ (x - d(1 - e^{-i\omega_c t}))y + \frac{y}{1 + \Delta^2} \left[ k_0 - x + d(1 - e^{-i\omega_c t}) \right] \right]} \\ &\times e^{-\frac{\Delta^2}{1 + \Delta^2} \frac{y^2}{2}} e^{-\frac{1}{2(1 + \Delta^2)} \left[ x - (k_0 + d(1 - e^{-i\omega_c t})) \right]^2}. \end{aligned} \quad (4.33)$$

The density has a trivial form,

$$|\psi(x, y, t)|^2 = \frac{1}{\pi} \frac{\Delta}{1 + \Delta^2} e^{-\frac{\Delta^2}{1 + \Delta^2} \left[ y - d \sin \omega_c t \right]^2} e^{-\frac{1}{1 + \Delta^2} \left[ x - (d + k_0) + d \cos \omega_c t \right]^2}. \quad (4.34)$$

This new packet is a semi-classical object and makes a elliptic motion with the cyclotron frequency. It is obviously not in the lowest Landau level of the system as

it is not stationary any more. The kinetic momentum shift provides the necessary energy for the excitation to higher Landau levels. The missing electric field pulse  $\vec{E} = \frac{d}{\tau}\hat{y}$  for the time dependent vector potential  $\vec{A}(\vec{r}, t) = (x - d\frac{t}{\tau})\hat{y}$  causes this momentum kick. After the quench, the coherent state has the following classical center of mass as a function time,

$$\langle \vec{x}_{CoM}(t) \rangle = \left( k_0 + d(1 - \cos \omega_c t), d \sin \omega_c t \right) \quad (4.35)$$

The continuum and the lattice systems provides qualitatively similar answers to the magnetic flux and field (they are identical for quantized orbits) quenches and both of the dynamics are gauge dependent.

The edge states are defined for the guiding center coordinates which is a few magnetic lengths outside the strip. Since the wavepacket is incapable of escaping outside the infinite walls as the edges, they are squeezed in a small region and form new quantized skipping orbits. This system can well be modelled as a linear potential. Then the resulting wavefunction is approximated as,

$$\psi_{n,k_y}(x, y) = A_0 Ai([2k_0^2]^{1/3}(x - \frac{E_n}{k_0} + \frac{k_0}{2})) \frac{e^{ik_0 y}}{\sqrt{2\pi}}, \quad (4.36)$$

$$E_n = \frac{k_0^2}{2} - \left(\frac{k_0^2}{2}\right)^{1/3} z_n, \quad (4.37)$$

$A_0$  is the normalization constant and  $z_n$  are the quantizing zeros of the Airy function[54].

For the edge states, we consider a quench in the vector potential as,

$$\vec{A}_2 = \frac{B_1}{B_0} x \hat{y}, \quad (4.38)$$

note that the potential is non-dimensional. The sudden change will decompose the initial wavefunction into the new eigenstates with different weights. The large number and amount of overlaps with the bulk states result in the dispersion of that edge state into the whole strip, if the situation is the opposite, the initial edge state wavepacket maintains itself at the edge. The overlap weights can be grasped from the local density of states of the quenched Hamiltonian. In contrast to the ribbon case, there are infinitely many states present in the new system. In

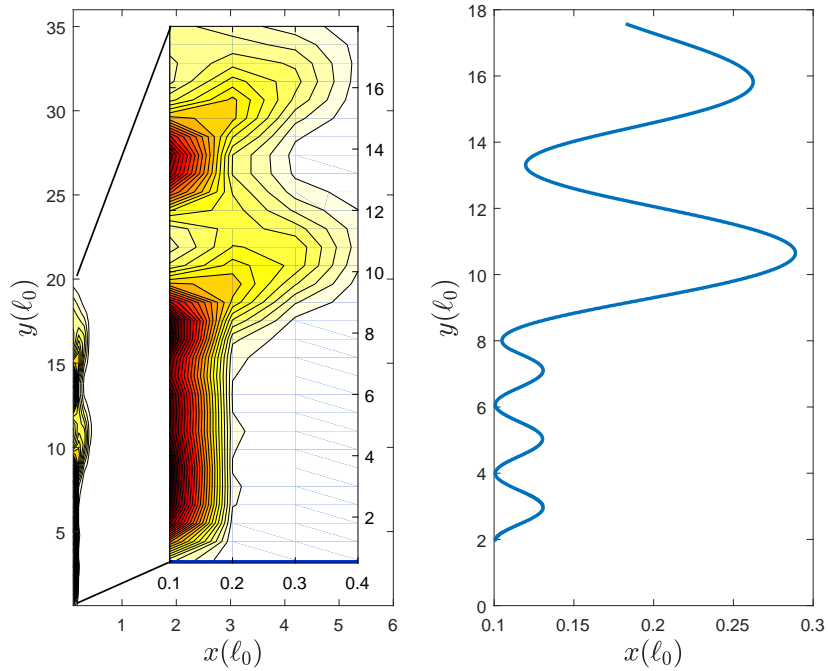


Figure 4.13: The dynamical response of the initial edge state wavepacket during the magnetic field quench. The initial packet, in  $x$  direction, is initially prepared as the shifted waveform of the ground state of the guiding center  $k_0 = -2$  and in  $y$ -direction, the form is Gaussian as a superposition of momentum eigenstates localized around the guiding center  $k_0$ . The magnetic field is quenched as  $B = 90 \rightarrow 35$  in units of initial magnetic field  $B_0$ , and  $B_0$  also determines the typical length scale  $\ell_0 = \sqrt{\hbar/eB_0}$  and the energy scale  $E_0 = \hbar e B_0/m$  in the system. We also plot the center-of-mass coordinate as a function of time, the wavepacket clearly indicates the skipping orbits before and after the quench with different quantized radius of orbits. It is worth noting that the edge state in continuum case is always robust unlike its lattice counterpart since the number of available edge states are infinite in this limit.

this respect, one expect the robustness of all edge states under a magnetic field quench as long as this quench is not the turn-off or the reversal of the direction. We plot the accumulated density, in Fig.4.13, within the time interval including pre- and post-quench wavefunction. The edge state is bound to the edge and shows a skipping orbit character[55]. If we are to combine the preservation of the edge states in the lattice and the continuum case, it is observed that the lattice edge states robust if they are protected under the quench and the continuum limit guarantees this protection.

## Chapter 5

# Artificial Magnetic Flux Quench of the Laughlin State

We have the most trivial quenching calculation for a Gaussian packet of Landau levels in a finite width continuum model in Chapter 4. We now consider a quench scenario, where the magnetic field does not change at all, but the symmetric gauge is simply shifted by constant term,

$$\vec{A}(t) = \begin{cases} \frac{B}{2}(-y, x), & \text{if } t < 0. \\ \frac{B}{2}(-(y - y_0), (x - x_0)), & \text{if } t \geq 0. \end{cases}$$

The Hamiltonian is as follows,

$$\hat{H}(t) = \begin{cases} \frac{1}{2} \left[ \left( -i \frac{\partial}{\partial x} - \frac{y}{2} \right)^2 + \left( -i \frac{\partial}{\partial y} + \frac{x}{2} \right)^2 \right], & \text{if } t < 0. \\ \frac{1}{2} \left[ \left( -i \frac{\partial}{\partial \tilde{x}} - \frac{\tilde{y}}{2} \right)^2 + \left( -i \frac{\partial}{\partial \tilde{y}} + \frac{\tilde{x}}{2} \right)^2 \right], & \text{if } t \geq 0, \end{cases} \quad \begin{cases} \tilde{x} = x - x_0, \\ \tilde{y} = y - y_0. \end{cases} \quad (5.1)$$

We would like to change the notation,  $z = (x + iy)/l_B$ ,  $(x - iy)/l_B$  and  $z_0 = (x_0 + iy_0)/l_B$ . Then,

$$\partial = \frac{\partial}{\partial z} = \frac{1}{2l_B}(\partial_x - i\partial_y), \quad \bar{\partial} = \frac{\partial}{\partial \bar{z}} = \frac{1}{2l_B}(\partial_x + i\partial_y),$$

where  $l_B = \sqrt{\frac{\hbar}{eB}}$ . Note that  $[\partial, z] = [\bar{\partial}, \bar{z}] = 1$ . Defining the annihilation and creation operators as,

$$\hat{a} = -\frac{i}{\sqrt{2}} \left( 2\bar{\partial} + \frac{z}{2} \right), \quad \hat{a}^\dagger = -\frac{i}{\sqrt{2}} \left( 2\partial - \frac{\bar{z}}{2} \right).$$

The algebraic relation still holds,  $[a, a^\dagger] = 1$ , since it is constant it shows  $a, a^\dagger$  are canonical conjugate variables. The Hamiltonian, then, can be rewritten as,

$$\hat{H} = \hbar\omega (a^\dagger a + 1/2).$$

The independent basis for the lowest Landau levels (LLs) can be chosen as,

$$\psi_n(z, \bar{z}) = \frac{z^n}{(n!\pi(2l_B^2)^{n+1})^{1/2}} e^{-z\bar{z}/4}$$

The generator and annihilator of degenerate basis operators can be constructed as follows

$$b^\dagger = \frac{1}{\sqrt{2}} \left( -2\bar{\partial} + \frac{z}{2} \right), \quad b = \frac{1}{\sqrt{2}} \left( 2\partial + \frac{\bar{z}}{2} \right)$$

$[b, b^\dagger] = 1$  and  $[b^\dagger, H] = 0$ . The algebra implies that  $b$  and  $b^\dagger$  generates degenerate basis because it preserves the energy eigenvalues when a function of two operators  $f(b, b^\dagger)$  is acted on any eigenstate of Hamiltonian.

Laughlin state is the exact many-body ground state wavefunction for the contact interaction of LLs[56]. For the filling factor,  $\nu = 1/q$ , the Laughlin function has the following form,

$$\begin{aligned} \Psi_q^{Laughlin}(\{z_k\}) &= \prod_{i < j}^N (z_i - z_j)^q e^{-\frac{1}{4} \sum_i |z_i|^2}, \\ &= \left( \prod_{i < j}^N (z_i - z_j)^q e^{-\frac{1}{4N} |z_i - z_j|^2} \right) e^{-\frac{N}{4} |Z|^2}, \quad Z = N^{-1} \sum_i z_i. \end{aligned}$$

where  $z_i = \frac{x_i + iy_i}{l_B}$ . In the second line, the many-body wavefunction is decomposed into the relative and center-of-mass (CoM) components.

The vector potential quench results in a shift of every coordinate in the many-body wavefunction and we can decompose it into the following form,

$$\begin{aligned}
\Psi_q^{Laughlin}(\{z_k - z_0\}) &= e^{-\frac{N}{4}|Z - z_0|^2} \left( \prod_{i < j}^N (z_i - z_j)^q e^{-\frac{1}{4N}|z_i - z_j|^2} \right), \\
&= e^{\frac{iN}{2}(Z_x y_0 - Z_y x_0)} e^{-\frac{N}{4}(Z\bar{Z} - 2\bar{z}_0 Z + z_0 \bar{z}_0)} \left( \prod_{i < j}^N (z_i - z_j)^q e^{-\frac{1}{4N}|z_i - z_j|^2} \right), \\
&= e^{\frac{iN}{2}(Z_x y_0 - Z_y x_0)} \psi_{N^{0.5}\bar{z}_0}^{cohrnt}(Z) \left( \prod_{i < j}^N (z_i - z_j)^q e^{-\frac{1}{4N}|z_i - z_j|^2} \right)
\end{aligned}$$

Note that the CoM state becomes a coherent state with the following form,

$$\psi_{N^{0.5}\bar{z}_0}^{cohrnt}(Z) = e^{-\frac{N}{4}(Z\bar{Z} - 2\bar{z}_0 Z + z_0 \bar{z}_0)}, \quad (5.2)$$

and the notation for  $\psi_{N^{0.5}\bar{z}_0}^{cohrnt}(Z)$  is simplified as  $\psi_{\bar{z}_0}^{cht}(Z)$ . In addition, the coherent CoM state  $\psi_{\bar{z}_0}^{cht}(Z) = \langle Z | \psi_{\bar{z}_0}^{cht} \rangle$ , can also be represented as the translated ground state harmonic oscillator eigenstate,  $D(\sqrt{N}\bar{z}_0)|0\rangle = |0; \sqrt{N}\bar{z}_0\rangle$ , where  $D(\alpha)$  is the translation operator in the complex plane, defined as  $D(\alpha) = e^{(\alpha B^\dagger - \alpha^* B)/2}$ . The first index in the ket notation,  $|0; \sqrt{N}\bar{z}_0\rangle$  is the LL index, the second is the amount of translation or the coherent state phase.

The overall wavefunction gains a magnetic phase proportional to the CoM displacement as shown in the first term.

And as seen from the quenched many-body wavefunction, the CoM coordinate becomes a coherent state, which is the eigenstate of the many-body CoM annihilation operator,

$$\hat{B} = \sum_i \hat{b}_i = \frac{1}{\sqrt{2}} \left( 2\partial_Z + \frac{N\bar{Z}}{2} \right),$$

and

$$\hat{B} \psi_{N^{0.5}\bar{z}_0}^{cohrnt}(Z) = \frac{N\bar{z}_0}{\sqrt{2}} \psi_{N^{0.5}\bar{z}_0}^{cohrnt}(Z).$$

Note that the CoM eigenstates are degenerate and a coherent state of them is also the ground state. In the post-quench system, the CoM makes a cyclotron motion around  $Z = 0$  with a radius of  $|\sqrt{N}z_0|$ . The adiabatic phase accumulation after one period has two contributions, the Aharonov-Bohm phase and the Berry phase due to the coherent state.

In this representation, it is trivial to calculate the accumulated Aharonov-Bohm phase due to the symmetric gauge, it is proportional to the enclosed flux as follows,

$$\Theta_{AB} = \frac{q}{\hbar} \oint_C \vec{A} \cdot d\vec{l} = \frac{q}{\hbar} \iint_D \vec{B} \cdot d\vec{S} = \frac{q}{\hbar} B \pi N r_0^2 = 2\pi \frac{q}{e} \frac{\Phi}{\phi_0}.$$

Accumulated phase  $\gamma_0$  due to the coherent CoM state  $\psi_{N^{0.5}\bar{z}_0}^{cohrrnt}(Z)$  can be calculated by adiabatically moving  $z_0$  around the origin of CoM coordinate. Assume  $\sqrt{N}\bar{z}_0 = X_1 + iX_2$ , then

$$\begin{aligned} \gamma_0(c) &= \oint_c d\mathbf{X} \langle 0, \bar{z}_0 | \vec{\nabla}_{\mathbf{X}} | 0; \bar{z}_0 \rangle, \\ &= \oint_c d\mathbf{X} \langle 0 | D^\dagger(\bar{z}_0) \vec{\nabla}_{\mathbf{X}} D(\bar{z}_0) | 0 \rangle, \end{aligned}$$

$$\text{where , } \begin{cases} D^\dagger(\bar{z}_0) \partial_{X_1} D(\bar{z}_0) = iX_2 + (B^\dagger - B) \\ D^\dagger(\bar{z}_0) \partial_{X_2} D(\bar{z}_0) = iX_1 + i(B^\dagger + B) \end{cases},$$

$$\gamma_0(c) = \oint_c (dX_2 X_1 - dX_1 X_2), \text{ using Green's theorem on a plane [57]}$$

$$\gamma_0(c) = \iint_D \left( \frac{\partial X_1}{\partial X_1} + \frac{\partial X_2}{\partial X_2} \right) dX_1 dX_2 = 2\pi N r_0^2 / l_B^2 = 2\pi \frac{\Phi}{\phi_0}.$$

$\phi_0 \equiv \frac{h}{e}$  is the magnetic flux quantum and  $\Phi$  is the magnetic flux enclosed by a semi-classical motion.

As seen in the quenched system, the total accumulated magnetic phase has two sources: the coherent center of mass wavefunction and the effective spread of

the relative coordinates in the many-body wavefunction. This finding is no surprise and in agreement with Kohn's theorem[58]. It simply states that the many body systems interacts with the magnetic field only through the center of mass coordinates. The center of mass coordinate is quantized as a harmonic oscillator eigenstates. Note that the strong correlation Jastrow-like factor is not due to the magnetic field but the massive degeneracy. Hence, our result is exactly the coherent state of CoM wavefunction and this semi-classical behavior, as discussed in Chapter 4, is due to the trivial vector potential quench.

# Chapter 6

## Conclusion

In this Thesis we investigated the effect of adiabatic and non-adiabatic changes of external parameters in lattice systems.

In Chapter 2, we discussed the role of adiabaticity in the Schrödinger equation. We first explained the adiabatic approximation and derived the time evolution of a system with an additional geometric phase and dynamical phase,  $\gamma_n(t)$  and  $\Theta_n(t)$ . The geometric phase is crucial to introduce the effect of the magnetic field by the Peierls substitution as a Aharonov-Bohm effect. We then briefly summarized the non-adiabaticity, and as a special extreme case the quench. Also, we discussed the significance of quench experiments in the current many-body non-equilibrium cold-atom experiments.

In Chapter 3, we focused on the direct relation between the point group symmetries in 2D and the energy spectrum even in the presence of magnetic flux. Specifically, we examine the adiabatic transitions between Bravais lattices belonging to different symmetry groups. All two dimensional such lattices are created using a spatial optical lattice potential created by two interfering lasers. This potential modelled by a tight binding description for the lowest band solution of the Schrödinger equation and the parameters of the model are calculated ab-initio.

The magnetic field is introduced through a Peierls phase. Next, the energy spectra for lattices belonging to each point symmetry group are calculated and the evolution of the energy spectrum during an adiabatic transition between these lattices is investigated.

We found that departure from the high symmetry lattices lead to significant changes in the energy spectra. The evolution of the lattice geometry from the square lattice to the triangular lattice is guided by the broken bipartite symmetry. The non-trivial changes in the spectrum take place around  $\theta = \pi/3$ , the triangular lattice limit. Such a rapid change in the vicinity of the triangular lattice should be experimentally observable for the simplest non-trivial magnetic flux  $\phi = 1/3$ , because a small deviation from the angle  $\theta = \pi/3$  results in jump in the Hall conductivity when the system is filled such that the Fermi energy is in the first gap.

Transitions are found to follow the touching and reopening of the energy bands and lead to Chern numbers transfer. We find that the Chern number transfer only occurs with integer multiples of  $q$ , the denominator of the magnetic flux. We explain this interesting property by exploiting the  $q$ -fold degeneracy in the magnetic Brillouin zone. The transport experiments can directly probe for  $q$ -Chern number transfer.

In the last section, we classify all the Bravais lattices in the parameter space with their topological phases. For a rational value of the magnetic flux,  $\phi = p/q$ , each topological phase is characterized by the Chern numbers associated with the  $q - 1$  energy gaps. For  $\phi = 1/3$ , all Bravais lattices are found to belong either to the square lattice or the triangular lattice. The triangular lattice topological phase is observed to track the centered rectangular lattice curve. For  $\phi = 1/5$ , the space is divided into four phases and this number of regions of phases increase as the value of  $q$  larger.

In Chapter 4, we investigated the effect of sudden changes in the artificial magnetic field for lattice systems. The take-away message is that the gauge choices in implementing the artificial magnetic field have dynamical observable effects

on the system. More specifically, the artificial gauge fields are realized without any dynamical Maxwell equation restricting the system. Therefore, quenching of the magnetic field into two Hamiltonians which are connected by a static gauge transformation yields two different dynamics and consequently observables.

This surprising observation is first verified with a toy model, made of six site tight binding lattice. The same initial wavefunction is dynamically tracked during the magnetic field change for two Hamiltonians related by a static gauge transformation. If the magnetic field is changed adiabatically, the two Hamiltonians yield the same dynamics. In the case of non-adiabatic changes, including the instantaneous changes or quenches, the observables are affected by the choice of the vector potential. The two statically connected Hamiltonians are lacking the dynamical gauge invariance due to the missing time dependent on-site potentials in the experiments to recover the full gauge symmetry.

We observe that this gauge dependence in the minimal model with synthetic dimensions can well be implemented for two reasons. Firstly, the capability of fast changes of artificial gauge fields using the Raman lasers allows for non-adiabatic dynamics. Secondly, two gauge choices discussed and proposed to be implemented by a real space potential plus the hyperfine synthetic dimension. One of the gauges corresponds to two isolated spatial sites and three hyperfine levels on each spatial site. Another gauge can be implemented by isolated three spatial lattice sites and two hyperfine levels as the synthetic dimension.

The flux quench scenarios were investigated in two- and three-leg ladder systems as the recent synthetic dimensional experiments are capable to implement the flux quenches and investigate the dynamical implications. The initial wavepackets, after the artificial magnetic flux quench, are found to split into different number of packets depending on the gauge choice. The smaller packets have distinct weights and velocities, and these quantities are calculated analytically in two-leg ladders and numerically in three-leg ladders. More specifically, we first consider flux quenches from zero field to a finite value  $\phi$ . In the case of the gauge choice for a generalized  $n$ -leg ladder, where the magnetic vector potential is parallel to the infinite legs, the initial packet around a lattice momentum

eigenstate can at most divide into  $n$  smaller packets. Meanwhile the number of maximum post-quench packets are  $n^2$  if the magnetic vector potential is along the rungs of the ladder. This is a surprising and understandable result. Firstly surprising, because the number of resulting packets are independent of the value of the magnetic flux,  $\phi$ , and this value determines the number of band fracturing in one of the gauge choices. Secondly, it is an understandable result because we cannot expect larger and larger number of packets as a rational value of magnetic flux,  $\phi = p/q$  has a larger denominator; irrational values of  $\phi$  would absurdly leads infinite number of packets. The findings on the maximum number of packets are verified numerically by the overlap of the initial states with the new states in the quenched Hamiltonian at the same lattice momentum. Moreover, we considered a quench where an initial packet prepared at finite magnetic flux is quenched to zero flux generated by a constant vector potential along the synthetic dimension. We concluded that a constant vector potential, as compared to zero vector potential, does not change the number of packets or their total density in each spatial site, but it changes the dynamical hyperfine distribution due to the gauge dependent character of the system. The analysis for synthetic ladder systems are within the capabilities of current experiments.

In the last section of Chapter 4, under a quench, we investigated the dynamical behavior of the edge states, which are topologically protected at equilibrium. In a wide ladder, specifically fifteen leg ladder, an initial edge state packet is not guaranteed for protection under a flux quench. Under certain values of the magnetic fluxes, the edge state is robust only if there exist at least one edge state residing in the same energy gap of the quenched Hamiltonian and the initial packet is mostly transferred into the new edge state. We compared this finding with the continuum problem and unlike the lattice case, the edge states are always protected under the quench as the existence of the edge states are guaranteed in continuous strip due to the termination of the Landau levels and the appearance of the skipping orbits. The post-quench wavepackets have skipping orbit as a semi-classical object.

In Chapter 5, we calculated the effect of a shift on the vector potential by a constant on the many-body ground states of contact interaction of LLs, the

Laughlin state. We found that the Laughlin state center of mass couples with the extra magnetic field and becomes a coherent state. The signature of such effect is the total accumulated phase as it is doubled compared to the pre-quench case, because the geometrical phase gives an equal contribution as the Aharonov-Bohm phase for a  $2\pi$  rotation around the origin.

## 6.1 Outlook

In this section, we focus on two aspects of this thesis, experimental indications and possible extensions to make contribution to the literature. We highlight the discussion in the manuscript to gather experimental indications in one place. In addition, there are certain subjects which are not covered due to time limitation or is not included in the thesis. We try to answer how the work carried out within this thesis can be extended for other studies.

### Experimental Aspects

Concerning Chapter 3, the effect of an adiabatic lattice deformations on the energy spectrum and the Hall conductivity, firstly, the energy spectrum during the transition from the square to rectangular lattice can be traced in the reverse limit. Isolated 1D chains in optical lattices can be arranged to couple weakly. This coupling must lead to two robust energy gaps characterized by non-trivial Chern numbers,  $\pm 1$ . In other words, the quantum Hall currents seem to be robust under a asymmetric deformation of hopping amplitudes in two directions. Secondly, it is found that the Chern number transfers changes by the denominator  $q$  of the magnetic flux per plaquette,  $\phi = p/q$ . The topological phase transition can be observed during the deformation from the triangular lattice (broken bipartite symmetry) to the square lattice. Surprisingly the transition takes place in the vicinity of  $\theta = \pi/3$ , or a few degrees of deviation from this angle should lead to a jump in the Hall current by proportional to the denominator  $q$ . In the case of  $\phi = 1/3$ , the jump in the current is  $3e^2/\hbar$ . The deviations in the lattice

angle can be realized by manipulating acoustic modulators or by an extra laser to introduce an extra potential barrier to reduce the hopping amplitudes in one axis of  $C_6$  symmetric lattice such that  $C_6$  is broken.

Concerning the gauge dependent dynamics in Chapter 4, it can be realized in synthetic dimensions. In a concrete example, the minimal six-site model to prove the gauge dependence of site densities as a function of time can be realized by either isolated two real sites plus three synthetic nuclear spin states or isolated three real site plus two synthetic nuclear spin states. Also, the synthetic ladder flux quench experiments in the case of  $\phi = 0 \rightarrow \phi_f$ , results in  $N$  or  $N^2$  packets depending on the Landau gauge choice if our calculations captures the physical system in current experiments.

## Possible extensions

In Chapter 3, we investigated the effect of an adiabatic lattice deformations on the energy spectrum and the Hall conductivity. In each unit cell there is one potential minimum, we did not cover the case where there is  $N$  basis elements arbitrarily distributed within the unit cell. The energy spectrum and the Chern number map for such a system can be useful considering the recent experiments on 2D layered heterostructures.

In Chapter 4, we investigated the effect of the gauge choice on the artificial magnetic flux wavepacket dynamics. The implications of the gauge dependence can be extended to interacting systems and one can search for possible signature of gauge dependence in measurements.

Concerning the gauge dependent effects on the Laughlin state in Chapter 5, it is possible to generate non-trivial excitations as a quench in the magnetic vector potential goes beyond a shift by a constant. If the magnitude of the magnetic field is scaled then it is possible to obtain quasi-hole and quasi-electron oscillations[56].

## 6.2 Self-Evaluation

In artificial gauge fields, we eventually become aware of the source of another extra gauge dependence due to the micromotion operator due to the periodically electric field coupled dipole elements of atoms. We did not include this effect as it can be arranged to give zero contribution if the effective system can be measured at integer multiple of time period. Therefore, there will be two source of gauge dependent dynamics, one is inherent to the lack of simulated scalar potential, the other is the imperfect effective Hamiltonian where all parameters are renormalized by the Floquet driving.

# Bibliography

- [1] Y. Hatsugai and M. Kohmoto, “Energy spectrum and the quantum Hall effect on the square lattice with next-nearest-neighbor hopping,” *Phys. Rev. B*, vol. 42, pp. 8282–8294, Nov 1990.
- [2] D. J. Griffiths, *Introduction to quantum mechanics*. Cambridge University Press, 2016.
- [3] A. Aguiar Pinto, M. Nemes, J. Peixoto de Faria, and M. Thomaz, “Comment on the adiabatic condition,” *American Journal of Physics*, vol. 68, no. 10, pp. 955–958, 2000.
- [4] U. Schneider, L. Hackermuller, J. P. Ronzheimer, S. Will, S. Braun, T. Best, I. Bloch, E. Demler, S. Mandt, D. Rasch, and A. Rosch, “Fermionic transport and out-of-equilibrium dynamics in a homogeneous Hubbard model with ultracold atoms,” *Nature Physics*, vol. 8, pp. 213–218, Mar 2012.
- [5] S. De, D. Campbell, R. Price, A. Putra, B. M. Anderson, and I. Spielman, “Quenched binary Bose-Einstein condensates: Spin-domain formation and coarsening,” *Phys. Rev. A*, vol. 89, no. 3, p. 033631, 2014.
- [6] W. K. Hensinger, H. Haffner, A. Browaeys, N. R. Heckenberg, K. Helmerson, C. McKenzie, G. J. Milburn, W. D. Phillips, S. L. Rolston, H. Rubinsztein-Dunlop, and B. Upcroft, “Dynamical tunnelling of ultracold atoms,” *Nature*, vol. 412, pp. 52–55, Jul 2001.
- [7] H. Lignier, C. Sias, D. Ciampini, Y. Singh, A. Zenesini, O. Morsch, and E. Arimondo, “Dynamical control of matter-wave tunneling in periodic potentials,” *Phys. Rev. Lett.*, vol. 99, no. 22, p. 220403, 2007.

- [8] A. Zenesini, H. Lignier, G. Tayebirad, J. Radogostowicz, D. Ciampini, R. Mannella, S. Wimberger, O. Morsch, and E. Arimondo, “Time-resolved measurement of Landau-Zener tunneling in periodic potentials,” *Phys. Rev. Lett.*, vol. 103, no. 9, p. 090403, 2009.
- [9] R. Nandkishore and D. A. Huse, “Many-body localization and thermalization in quantum statistical mechanics,” *Annu. Rev. Condens. Matter Phys.*, vol. 6, no. 1, pp. 15–38, 2015.
- [10] M. Schreiber, S. S. Hodgman, P. Bordia, H. P. Lüschen, M. H. Fischer, R. Vosk, E. Altman, U. Schneider, and I. Bloch, “Observation of many-body localization of interacting fermions in a quasirandom optical lattice,” *Science*, vol. 349, no. 6250, pp. 842–845, 2015.
- [11] J. Eisert, M. Friesdorf, and C. Gogolin, “Quantum many-body systems out of equilibrium,” *Nature Physics*, vol. 11, no. 2, pp. 124–130, 2015.
- [12] M. S. Rudner, N. H. Lindner, E. Berg, and M. Levin, “Anomalous edge states and the bulk-edge correspondence for periodically driven two-dimensional systems,” *Phys. Rev. X*, vol. 3, no. 3, p. 031005, 2013.
- [13] D. R. Hofstadter, “Energy levels and wave functions of Bloch electrons in rational and irrational magnetic fields,” *Phys. Rev. B*, vol. 14, pp. 2239–2249, Sep 1976.
- [14] C. R. Dean, L. Wang, P. Maher, C. Forsythe, F. Ghahari, Y. Gao, J. Katoch, M. Ishigami, P. Moon, M. Koshino, T. Taniguchi, K. Watanabe, K. L. Shepard, J. Hone, and P. Kim, “Hofstadter’s butterfly and the fractal quantum Hall effect in moiré superlattices,” *Nature*, vol. 497, pp. 598–602, 2013.
- [15] D. Jaksch and P. Zoller, “Creation of effective magnetic fields in optical lattices: the Hofstadter butterfly for cold neutral atoms,” *New Journal of Physics*, vol. 5, p. 56, May 2003.
- [16] H. Miyake, G. A. Siviloglou, C. J. Kennedy, W. C. Burton, and W. Ketterle, “Realizing the Harper Hamiltonian with laser-assisted tunneling in optical lattices,” *Phys. Rev. Lett.*, vol. 111, p. 185302, Oct 2013.

- [17] L. Tarruell, D. Greif, T. Uehlinger, G. Jotzu, and T. Esslinger, “Creating, moving and merging dirac points with a Fermi gas in a tunable honeycomb lattice,” *Nature*, vol. 483, pp. 302–305, 2012.
- [18] F. Yılmaz, F. N. Ünal, and M. O. Oktel, “Evolution of the Hofstadter butterfly in a tunable optical lattice,” *Phys. Rev. A*, vol. 91, p. 063628, Jun 2015.
- [19] R. Peierls, “Zur theorie des diamagnetismus von leitungselektronen,” *Zeitschrift für Physik*, vol. 80, pp. 763–791, Nov 1933.
- [20] M. Aidelsburger, M. Atala, S. Nascimbène, S. Trotzky, Y.-A. Chen, and I. Bloch, “Experimental realization of strong effective magnetic fields in an optical lattice,” *Phys. Rev. Lett.*, vol. 107, p. 255301, Dec 2011.
- [21] N. W. Ashcroft and N. D. Mermin, *Solid State Physics*. Philadelphia: Saunders College, 1976.
- [22] C. L. Kane, R. Mukhopadhyay, and T. C. Lubensky, “Fractional quantum Hall effect in an array of quantum wires,” *Phys. Rev. Lett.*, vol. 88, p. 036401, Jan 2002.
- [23] J. Zak, “Magnetic translation group,” *Phys. Rev.*, vol. 134, pp. A1602–A1606, Jun 1964.
- [24] S. Kivelson, “Wannier functions in one-dimensional disordered systems: Application to fractionally charged solitons,” *Phys. Rev. B*, vol. 26, pp. 4269–4277, Oct 1982.
- [25] G. H. Wannier, “The structure of electronic excitation levels in insulating crystals,” *Phys. Rev.*, vol. 52, pp. 191–197, Aug 1937.
- [26] R. O. Umucalılar and M. O. Oktel, “ $p$  band in a rotating optical lattice,” *Phys. Rev. A*, vol. 78, p. 033602, Sep 2008.
- [27] Rammal, R., “Landau level spectrum of Bloch electrons in a honeycomb lattice,” *J. Phys. France*, vol. 46, no. 8, pp. 1345–1354, 1985.

- [28] W. G. Chambers, “Linear-network model for magnetic breakdown in two dimensions,” *Phys. Rev.*, vol. 140, pp. A135–A143, Oct 1965.
- [29] J. E. Avron, O. Kenneth, and G. Yehoshua, “A study of the ambiguity in the solutions to the Diophantine equation for Chern numbers,” *Journal of Physics A: Mathematical and Theoretical*, vol. 47, no. 18, p. 185202, 2014.
- [30] F. H. Claro and G. H. Wannier, “Magnetic subband structure of electrons in hexagonal lattices,” *Phys. Rev. B*, vol. 19, pp. 6068–6074, Jun 1979.
- [31] G. G. Naumis and F. J. Lopez-Rodriguez, “The electronic spectrum of a quasiperiodic potential: From the Hofstadter butterfly to the Fibonacci chain,” *Physica B: Condensed Matter*, vol. 403, no. 10–11, pp. 1755 – 1762, 2008.
- [32] D. J. Thouless, M. Kohmoto, M. P. Nightingale, and M. den Nijs, “Quantized Hall conductance in a two-dimensional periodic potential,” *Phys. Rev. Lett.*, vol. 49, pp. 405–408, Aug 1982.
- [33] R. O. Umucalılar, H. Zhai, and M. O. Oktel, “Trapped Fermi gases in rotating optical lattices: Realization and detection of the topological Hofstadter insulator,” *Phys. Rev. Lett.*, vol. 100, p. 070402, Feb 2008.
- [34] P. Štředa, “Theory of quantised Hall conductivity in two dimensions,” *Journal of Physics C: Solid State Physics*, vol. 15, no. 22, p. L717, 1982.
- [35] Y.-J. Lin, R. L. Compton, K. Jimenez-Garcia, J. V. Porto, and I. B. Spielman, “Synthetic magnetic fields for ultracold neutral atoms,” *Nature*, vol. 462, pp. 628–632, Dec 2009.
- [36] M. Aidelsburger, M. Atala, M. Lohse, J. T. Barreiro, B. Paredes, and I. Bloch, “Realization of the Hofstadter Hamiltonian with ultracold atoms in optical lattices,” *Phys. Rev. Lett.*, vol. 111, p. 185301, Oct 2013.
- [37] M. Aidelsburger, M. Lohse, C. Schweizer, J. T. Atala, M. and Barreiro, S. Nascimbène, N. R. Cooper, I. Bloch, and N. Goldman, “Measuring the Chern number of Hofstadter bands with ultracold bosonic atoms,” *Nature Physics*, vol. 11, pp. 162–166, 2015.

- [38] N. Goldman, J. Dalibard, A. Dauphin, F. Gerbier, M. Lewenstein, P. Zoller, and I. B. Spielman, “Direct imaging of topological edge states in cold-atom systems,” *Proceedings of the National Academy of Sciences*, vol. 110, no. 17, pp. 6736–6741, 2013.
- [39] G. Jotzu, M. Messer, R. Desbuquois, M. Lebrat, T. Uehlinger, D. Greif, and T. Esslinger, “Experimental realization of the topological Haldane model with ultracold fermions,” *Nature*, vol. 515, pp. 237–240, 2014.
- [40] N. Goldman, J. Budich, and P. Zoller, “Topological quantum matter with ultracold gases in optical lattices,” *Nature Physics*, vol. 12, no. 7, pp. 639–645, 2016.
- [41] L. J. LeBlanc, K. Jiménez-García, R. A. Williams, M. C. Beeler, A. R. Perry, W. D. Phillips, and I. B. Spielman, “Observation of a superfluid Hall effect,” *Proceedings of the National Academy of Sciences*, vol. 109, no. 27, pp. 10811–10814, 2012.
- [42] J.-R. Li, J. Lee, W. Huang, S. Burchesky, B. Shteynas, F. Ç. Top, A. O. Jamison, and W. Ketterle, “A stripe phase with supersolid properties in spin-orbit-coupled Bose-Einstein condensates,” *Nature*, vol. 543, no. 7643, pp. 91–94, 2017.
- [43] J. Léonard, A. Morales, P. Zupancic, T. Esslinger, and T. Donner, “Supersolid formation in a quantum gas breaking a continuous translational symmetry,” *Nature*, vol. 543, no. 7643, pp. 87–90, 2017.
- [44] J. Dalibard, F. Gerbier, G. Juzeliūnas, and P. Öhberg, “Colloquium: Artificial gauge potentials for neutral atoms,” *Reviews of Modern Physics*, vol. 83, pp. 1523–1543, Nov 2011.
- [45] A. Celi, P. Massignan, J. Ruseckas, N. Goldman, I. B. Spielman, G. Juzeliūnas, and M. Lewenstein, “Synthetic gauge fields in synthetic dimensions,” *Physical Review Letters*, vol. 112, p. 043001, Jan 2014.

- [46] M. Mancini, G. Pagano, G. Cappellini, L. Livi, M. Rider, J. Catani, C. Sias, P. Zoller, M. Inguscio, M. Dalmonte, and L. Fallani, “Observation of chiral edge states with neutral fermions in synthetic Hall ribbons,” *Science*, vol. 349, no. 6255, pp. 1510–1513, 2015.
- [47] B. K. Stuhl, H.-I. Lu, L. M. Ayccock, D. Genkina, and I. B. Spielman, “Visualizing edge states with an atomic Bose gas in the quantum hall regime,” *Science*, vol. 349, no. 6255, pp. 1514–1518, 2015.
- [48] C. J. Kennedy, W. C. Burton, W. C. Chung, and W. Ketterle, “Observation of Bose-Einstein condensation in a strong synthetic magnetic field,” *Nature Physics*, vol. 11, pp. 859–864, Oct 2015.
- [49] E. J. Mueller, “Artificial electromagnetism for neutral atoms: Escher staircase and Laughlin liquids,” *Physical Review A*, vol. 70, p. 041603, Oct 2004.
- [50] M. Atala, M. Aidelsburger, M. Lohse, J. T. Barreiro, B. Paredes, and I. Bloch, “Observation of chiral currents with ultracold atoms in bosonic ladders,” *Nature Physics*, vol. 10, pp. 588–593, Aug 2014.
- [51] H. M. Price, O. Zilberberg, T. Ozawa, I. Carusotto, and N. Goldman, “Measurement of Chern numbers through center-of-mass responses,” *Physical Review B*, vol. 93, p. 245113, Jun 2016.
- [52] C. Wang, P. Zhang, X. Chen, J. Yu, and H. Zhai, “Scheme to measure the topological number of a Chern insulator from quench dynamics,” *Physical Review Letters*, vol. 118, p. 185701, May 2017.
- [53] F. Grusdt, N. Y. Yao, D. Abanin, M. Fleischhauer, and E. Demler, “Interferometric measurements of many-body topological invariants using mobile impurities,” *Nature Communications*, vol. 7, p. 11994, Jun 2016.
- [54] G. N. Watson, *A treatise on the theory of Bessel functions*. Cambridge university press, 1995.
- [55] G. Montambaux, “Semiclassical quantization of skipping orbits,” *The European Physical Journal B*, vol. 79, pp. 215–224, Jan 2011.

- [56] R. B. Laughlin, “Anomalous quantum hall effect: An incompressible quantum fluid with fractionally charged excitations,” *Phys. Rev. Lett.*, vol. 50, pp. 1395–1398, May 1983.
- [57] K. Riley, M. Hobson, and S. Bence, “Mathematical methods for physics and engineering,” 1999.
- [58] W. Kohn, “Cyclotron resonance and de haas-van alphen oscillations of an interacting electron gas,” *Phys. Rev.*, vol. 123, pp. 1242–1244, Aug 1961.

# Appendix A

## Numerical Schrödinger Equation for an Arbitrary Lattice

We start with the eigenvalue equation,

$$\begin{aligned}
 \hat{H}|\Psi\rangle &= E|\Psi\rangle \\
 \langle x|\hat{H}|\Psi\rangle &= E\langle x|\Psi\rangle \\
 \left[ -\frac{\hbar^2}{2m}(\partial_x^2 + \partial_y^2) + V(x, y) \right] \psi(x, y) &= E\psi(x, y) \\
 \left[ -\frac{\hbar^2}{2m}(\partial_x^2 + \partial_y^2) - V_Y \cos(\vec{k}_1 \cdot \vec{x}) \right. \\
 \left. - V_X \cos(\vec{k}_2 \cdot \vec{x}) - 2 \cos \theta \sqrt{V_X V_Y} \cos((\vec{k}_1 - \vec{k}_2) \cdot \vec{x}) \right] \psi(x, y) &= E\psi(x, y) \\
 \left[ -\frac{\hbar^2}{2m}(\partial_x^2 + \partial_y^2) - V_Y \cos(q_1 y) - V_X \cos(q_2(-\sin \theta x + \cos \theta y)) \right. \\
 \left. - 2 \cos \theta \sqrt{V_X V_Y} \cos([q_2 \sin \theta x + (q_1 - q_2 \cos \theta)y]) \right] \psi(x, y) &= E\psi(x, y)
 \end{aligned}$$

The first task is to make the equation dimensionless by defining  $\tilde{x} = x/\lambda_1$ ,  $\tilde{y} = y/\lambda_1$ ,  $\tilde{q}_j = q_j \lambda_1 = 2\pi \frac{\lambda_1}{\lambda_j} \frac{1}{\sin \theta}$ ,  $\tilde{E} = \frac{E}{\hbar^2/2m\lambda_1^2} = E/E_R$  and  $V_{X,Y}^{\sim} = \frac{V_{X,Y}}{\hbar^2/2m\lambda_1^2} =$

$V_{X,Y}/E_R$ , where  $\lambda_1$  is one of the laser wavelength and  $E_R = \frac{\hbar^2}{2m\lambda_1^2}$  is the corresponding recoil energy. The eigenvalue equation becomes,

$$\begin{aligned} & - \left[ 2 \cos \theta \sqrt{\tilde{V}_Y \tilde{V}_X} \cos \left( 2\pi \lambda_1 \left[ \frac{\tilde{x}}{\lambda_2} + \left( \frac{1}{\lambda_1 \sin \theta} - \frac{\cot \theta}{\lambda_2} \right) \tilde{y} \right] \right) \right] \psi(\tilde{x}, \tilde{y}) \\ & = \tilde{E} \psi(\tilde{x}, \tilde{y}) \end{aligned}$$

In order to go further and solve the differential equation by a finite difference method, we need to make a change of variables. It is because the shape of the unit cell is parallelogram as a function of  $\theta$  and a proper discretization should be with respect to the overall geometry, so parallelogram. Define  $x_1$  and  $x_2$  along the primitive vectors,

$$\begin{aligned} x_1 &= \tilde{x} - \tilde{y} \cot \theta \\ x_2 &= \tilde{y} / \sin \theta. \end{aligned}$$

This transforms the parallelogram (specifically rhombus) into a square and the calculations become much easier. We need to keep in mind that the new coordinate system is a skew-coordinate, where the basis vectors are not orthogonal.

Moreover,  $\tilde{x} = x_1 + \cos \theta x_2$ ,  $\tilde{y} = \sin \theta x_2$ . We find the differential operators in new coordinates, keeping in mind the Jacobian determinant is  $\det[J(\tilde{x}, \tilde{y})] = \frac{1}{\sin \theta}$ ,

$$\begin{aligned} \partial / \partial \tilde{x} &= \frac{\partial}{\partial x_1} \\ \partial^2 / \partial \tilde{x}^2 &= \frac{\partial^2}{\partial x_1^2} \\ \partial / \partial \tilde{y} &= \frac{\partial x_1}{\partial \tilde{y}} \frac{\partial}{\partial x_1} + \frac{\partial x_2}{\partial \tilde{y}} \frac{\partial}{\partial x_2} = -\frac{\cos \theta}{\sin \theta} \frac{\partial}{\partial x_1} + \frac{1}{\sin \theta} \frac{\partial}{\partial x_2} \\ \partial^2 / \partial \tilde{y}^2 &= \frac{\cos^2 \theta}{\sin^2 \theta} \frac{\partial^2}{\partial x_1^2} - 2 \frac{\cos \theta}{\sin^2 \theta} \frac{\partial^2}{\partial x_1 \partial x_2} + \frac{1}{\sin^2 \theta} \frac{\partial^2}{\partial x_2^2}. \end{aligned}$$

The Schrödinger equation in the new coordinates becomes:

$$\tilde{E} \psi(x_1, x_2) = \left[ -\frac{1}{\sin^2 \theta} \left( \frac{\partial^2}{\partial x_1^2} - 2 \cos \theta \frac{\partial^2}{\partial x_1 \partial x_2} + \frac{\partial^2}{\partial x_2^2} \right) + V(x_1, x_2) \right] \psi(x_1, x_2).$$

The potential is evaluated to be,

$$V(x_1, x_2) = -\tilde{V}_X \cos \left( 2\pi \frac{\lambda_1}{\lambda_2} x_2 \right) - \tilde{V}_Y \cos(2\pi x_1) - 2 \cos \theta \sqrt{\tilde{V}_X \tilde{V}_Y} \cos \left( 2\pi \left[ \frac{x_1}{\lambda_1} + \frac{x_2}{\lambda_2} \right] \right).$$

The domain is the unit cell of the potential. We used periodic boundary conditions up to a complex phase or Bloch condition. In  $x_1 - x_2$  coordinates the boundary conditions become,

$$\begin{aligned}\psi(\vec{x} + \vec{a}_1) &= e^{i\vec{k}\cdot\vec{a}_1}\psi(\vec{x}) = e^{ik_x\lambda_1}\psi(x, y) = e^{ik_{x_1}\sin\theta}\psi(x_1, x_2) \\ \psi(\vec{x} + \vec{a}_2) &= e^{i\vec{k}\cdot\vec{a}_2}\psi(\vec{x}) = e^{i(k_x\lambda_2\cos\theta + k_y\lambda_2\sin\theta)}\psi(x, y) = e^{ik_{x_2}\frac{\lambda_2}{\lambda_1}\sin\theta}\psi(x_1, x_2).\end{aligned}$$

In order to solve the Schrödinger equation for the given potential and the corresponding Bloch boundary conditions, we will use the Finite Difference Method. For this purpose, we need to approximate the partial derivatives and discretize dimensionless equation. Defining,  $x_1 = n\Delta_1$ ,  $x_2 = m\Delta_2$ ,

$$\begin{aligned}\partial_{x_1}\psi(x_1, x_2) &\simeq \frac{\psi_{n+1/2,m} - \psi_{n-1/2,m}}{\Delta_1} \\ \partial_{x_1}^2\psi(x_1, x_2) &\simeq \frac{\psi_{n+1,m} - 2\psi_{n,m} + \psi_{n-1,m}}{\Delta_1^2} \\ \partial_{x_1,x_2}\psi &\simeq \frac{\psi_{n+1,m+1} - \psi_{n+1,m} - \psi_{n,m+1} + 2\psi_{n,m} - \psi_{n-1,m} - \psi_{n,m-1} + \psi_{n-1,m-1}}{2\Delta_1\Delta_2}\end{aligned}$$

or the same finite difference in both directions can be re-expressed as,

$$\partial_{x_1,x_2}\psi \simeq \frac{\psi_{n+1,m+1} - \psi_{n+1,m-1} - \psi_{n-1,m+1} + \psi_{n-1,m-1}}{4\Delta_1\Delta_2} \quad (\text{A.1})$$

We will use the 2nd expression in Eq.A.1 even if the 1st approximation is computationally more efficient. Rearranging and collecting all the terms and defining  $\Delta = 1/N$  where N is the number of points the dimensionless unit length is divided into and omit the tilde symbols, we get

$$\begin{aligned}E\psi_{n,m} &= \frac{-1}{\sin^2\theta} \left[ \left( -\frac{\cos\theta}{2\Delta_1\Delta_2} [\psi_{n-1,m-1} - \psi_{n+1,m-1}] + \frac{1}{\Delta_2^2}\psi_{n,m-1} \right) \right. \\ &+ \left( \frac{\psi_{n-1,m} - 2\psi_{n,m} + \psi_{n+1,m} - 2\psi_{n,m}}{\Delta_1^2} \right) \\ &+ \left. \left( -\frac{\cos\theta}{2\Delta_1\Delta_2} [\psi_{n+1,m+1} - \psi_{n-1,m+1}] + \frac{1}{\Delta_2^2}\psi_{n,m+1} \right) \right] - V_{n,m}\psi_{n,m},\end{aligned}$$

where  $V_{n,m}$  is discretized to be,

$$\begin{aligned}V_{n,m}(\theta) &= V_X \cos\left(2\pi\frac{l}{\lambda_1}\frac{m}{N}\right) + V_Y \cos\left(2\pi\frac{\lambda_1}{\lambda_2}\frac{n}{N}\right) \\ &+ 2\cos\theta\sqrt{V_X V_Y} \cos\left(2\pi\left[\frac{n}{\lambda_2 N} + \frac{m}{\lambda_1 N}\right]\right).\end{aligned}$$

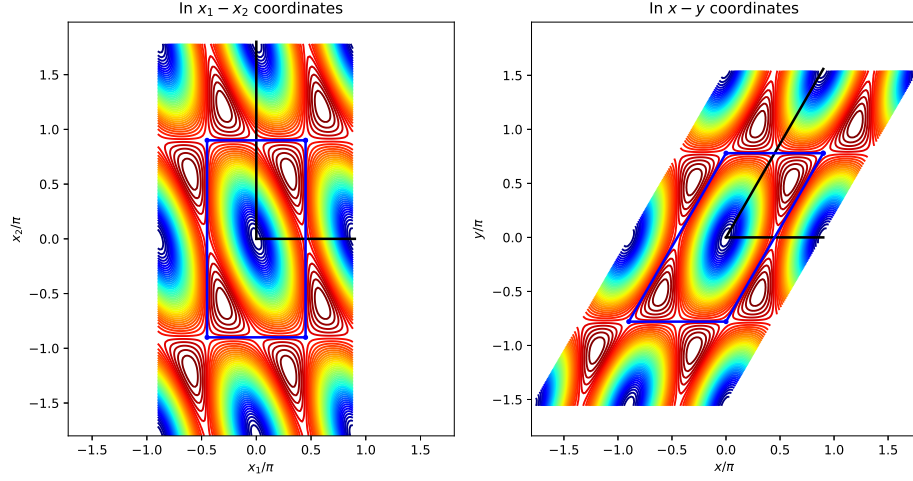


Figure A.1: Arbitrary unit cell is mapped into a rectangular zone in a curvilinear system. This mapping solves the complication coming from the boundary conditions for different lattice parameters and disconnects the possible contribution from both momentum variables.

We take the steps as equal,  $\Delta_1 = \Delta_2$ . This choice will alter the cell samples along primitive vectors, but the generic code handles possible problems.

The periodicity of the difference equation is imposed through the Bloch theorem and can be derived using the primitive vectors,  $\vec{a}_1 = \hat{x}_1$  and  $\vec{a}_2 = \frac{\lambda_2}{\lambda_1} \hat{x}_2$ .

$$\begin{aligned}\psi_{n+N,m} &= e^{ik_1} \psi_{n,m} \\ \psi_{n,m+N} &= e^{ik_2} \psi_{n,m},\end{aligned}$$

Also,  $k_1 = \vec{k} \cdot \vec{a}_1 = k_{x_1} \sin \theta$  and  $k_2 = \vec{k} \cdot \vec{a}_2 = k_{x_2} \frac{\lambda_2}{\lambda_1} \sin \theta$ .

# Appendix B

## Calculation of the Wannier Functions and the Tight Binding Hopping Parameters

The common description of Wannier functions (WFs) has indetermined phase for each Bloch state at each lattice momentum. Therefore the resulting Wannier functions can lead dramatically different densities which are not necessarily localized. It is also called the problem of gauge choice. The solution can be formulated as one requires the maximum localization, but the computational cost is so large [25]. There is another trivial definition for WFs, which was proposed by Kivelson[24]. He showed that the position operators projected on to the single band Hilbert space leads WFs as the eigenstates. The projected position operators an arbitrary ( $n^{th}$ ) band can be defined as,

$$\begin{aligned}\hat{x}_n &= \hat{P}_n \hat{x} \hat{P}_n, \\ \hat{y}_n &= \hat{P}_n \hat{y} \hat{P}_n,\end{aligned}$$

where

$$\hat{P}_n = \sum_k^{BZ} |n, k\rangle \langle n, k|, \tag{B.1}$$

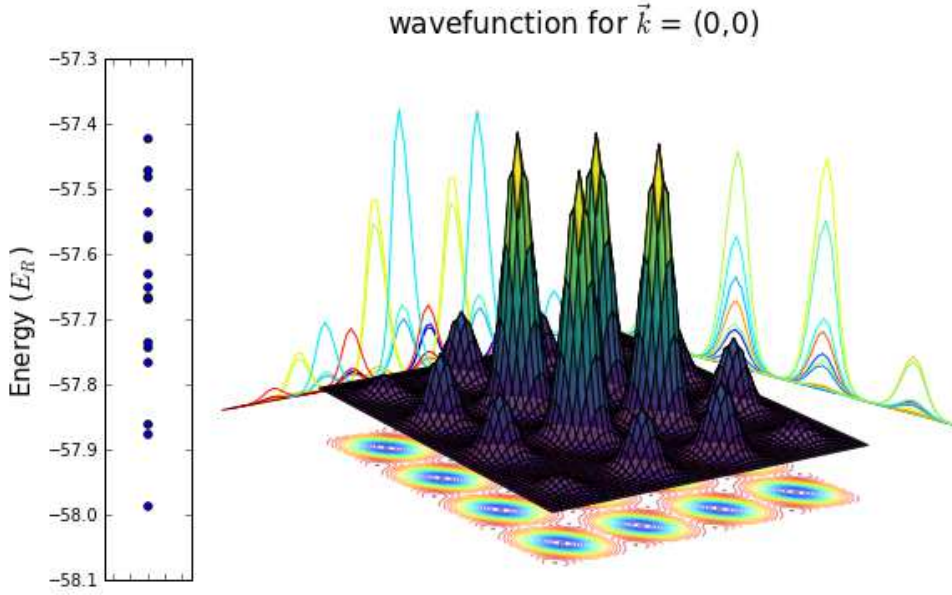


Figure B.1: Bloch-like density of the ground state of a 4-by-4 finite continuous system defined by the arbitrary optical potential. The form of the energy bands in the infinite lattice limit is not clear in the finite case. However, it is possible to observe that the first  $4 \times 4 = 16$  energy eigenvalues are isolated in the deep lattice limit where  $V_X, V_Y \gg E_R$ . These sixteen energies can be proposed as the representative states of the first band. The left plot shows these sixteen energies.

The eigenstates of  $\hat{x}_n, \hat{y}_n$  are the WFs and the eigenvalues are the corresponding Wannier centers,  $R$ ,

$$\hat{x}_n |W_n(r - R)\rangle = R |W_n(r - R)\rangle.$$

This definition reduces to the usual Fourier transform WFs definition, but is equally applicable to finite or disordered systems. Thus, we apply this theory for a finite portion of our optical lattice Schrödinger equation and form WFs to obtain the TB parameters.

We use a finite system with four unit cells along each primitive vector. The projection operator for the lowest band is formed by the first sixteen nearly degenerate eigenstates. Instead of separately diagonalizing  $\hat{x}_n, \hat{y}_n$  one after another, we diagonalize a linear combination, say  $\hat{O}_n = \hat{x}_n + \alpha \hat{y}_n$  for any  $\alpha \in \mathbb{C}$ . Quite surprise is to observe that a small finite system as 4-by-4 lattice is adequate to

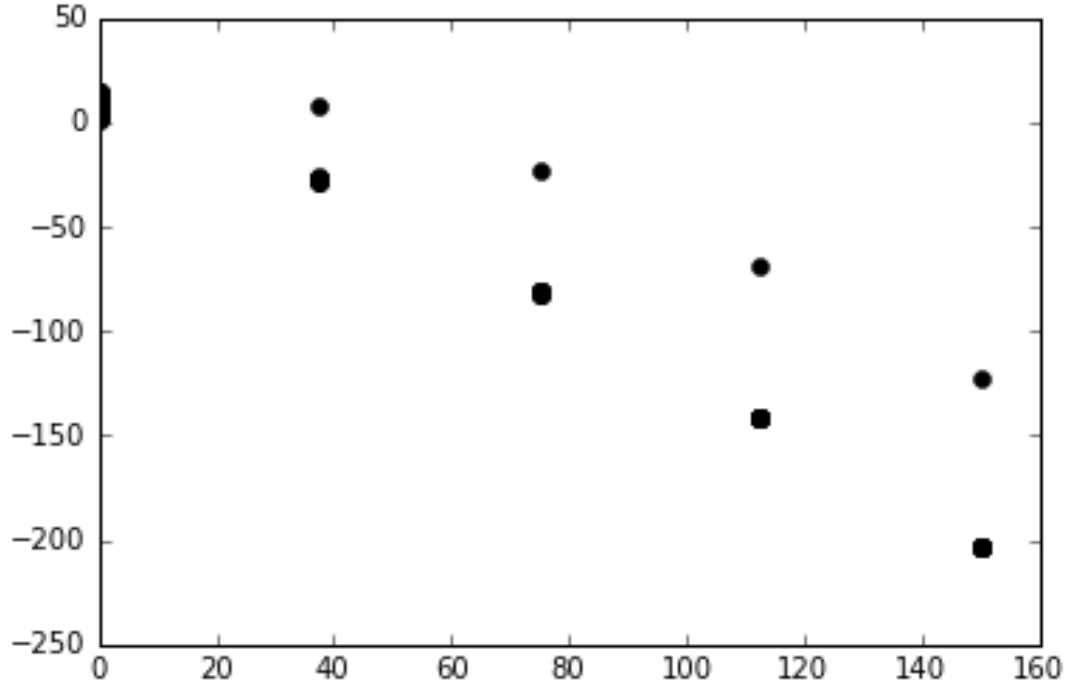


Figure B.2: The energy eigenvalues of the optical lattice system are plotted as a function of the lattice depths  $V_X = V_Y$ . In the deep lattice limit, the energies are clustered as they would form the energy bands in the infinite lattice limit. Therefore, one can use the isolated energies of the lowest cluster as the approximate Bloch functions of the lowest band.

capture the TB parameters of an infinite system within an error of one percent.

In the beginning, we solved the two-dimensional Schrödinger equation numerically for an arbitrary lattice of a 4-by-4 finite lattice. The lattice parameters for this calculation are arbitrarily chosen as  $V_x = V_y = 50$  (in units of  $E_R$ ),  $\Theta = 0.44\pi$ ,  $\lambda_2/\lambda_1 = 1$ . The numerical solution of the equation yields the energy eigenvalues and the corresponding Bloch-like wave functions at each energy.

In Fig.B.1, we plot the ground state density for this finite lattice. Even if there is no energy band formation due to the lack of translational symmetry, one can argue that the first  $4 \times 4 = 16$  energy states are the effective lowest band in the tight binding limit, where the lattice depth is much larger than the typical recoil energy of the system,  $V_X, V_Y \gg E_R$ . For this purpose, it is instructive to examine the separation of the energy eigenvalues for this optical potential as a

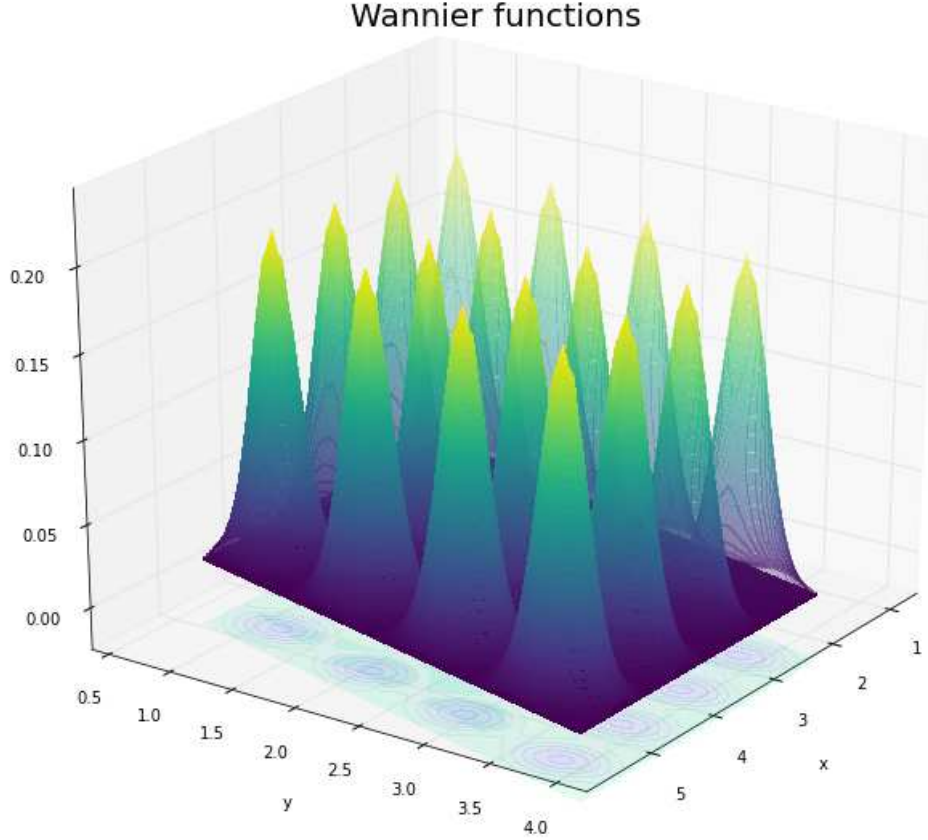


Figure B.3: The Wannier functions of the 4-by-4 lattice as the eigenstates of the weighted two dimensional projected operator,  $\hat{O}_n = \hat{x}_n + 0.1\hat{y}_n$ .

function of the lattice depth. In Fig. B.2, we plot the energy eigenvalues for the optical potential as a function of the lattice depth. We find that the energies are clustered in the deep lattice limit, and they would form the corresponding energy bands from these clustered energies in the infinite lattice limit.

Hence, we think it is logical to use the isolated lowest  $4 \times 4 = 16$  energy eigenstates as the approximate Bloch functions of the lowest band and form the projection operators in the position space representation,

$$\hat{P}_n = \sum_k^{BZ} |n, k\rangle \langle n, k|. \quad (\text{B.2})$$

Then we form the projected position operators,  $\hat{x}_n$  and  $\hat{y}_n$  in position space

representation. Note that the eigenstates of these operators yields the Wannier functions even in the finite or the disordered lattices. However, we do not desire neither Wannier functions localized only along  $x$  direction or only along  $y$  direction. The Wannier functions that we can use must be simultaneously localized in the two directions, and it is strictly speaking not possible. The operators  $\hat{x}_n$  and  $\hat{y}_n$  do not commute! Luckily, they are almost commuting operators and the non-commuting part decays to zero as the number of sites goes to infinity. Then, we choose a linear combination of these two operators, and instead of diagonalizing the them one of another, we simultaneously diagonalized the two operators as,  $\hat{O}_n = \hat{x}_n + \alpha\hat{y}_n$  for  $\alpha = 0.1$ . The resulting eigenvalues are not shown here, but they correspond to the weighted summation of the euclidean components of each Wannier center, and the eigenstates are the corresponding Wannier functions (see Fig.B.3).

We extend the eigenvalue equation for this system as,

$$\hat{O}_n|W_n(\vec{r} - \vec{R})\rangle = (R_x + \alpha R_y)|W_n(\vec{r} - \vec{R})\rangle.$$

The remaining part is to numerically calculate the tight binding hopping parameters and the on-site energies by sandwiching the Hamiltonian with the Wannier functions. For more accurate results, we use the bulk Wannier functions to reduce the edge effects for this small  $4 - by - 4$  system. The tight binding parameters are found as,

$$\begin{aligned} \epsilon_0 &= \langle W_1(\vec{r} - \vec{R}_{00}) | \hat{H} | \langle W_1(\vec{r} - \vec{R}_{00}) \rangle, \\ t_0 &= \langle W_1(\vec{r} - \vec{R}_{10}) | \hat{H} | \langle W_1(\vec{r} - \vec{R}_{00}) \rangle, \\ t_1 &= \langle W_1(\vec{r} - \vec{R}_{01}) | \hat{H} | \langle W_1(\vec{r} - \vec{R}_{00}) \rangle, \\ t_2 &= \langle W_1(\vec{r} - \vec{R}_{11}) | \hat{H} | \langle W_1(\vec{r} - \vec{R}_{00}) \rangle, \\ t_3 &= \langle W_1(\vec{r} - \vec{R}_{1-1}) | \hat{H} | \langle W_1(\vec{r} - \vec{R}_{00}) \rangle. \end{aligned}$$

Note that all the on-site energies,  $\epsilon_0$  are equal and dropped out in our model.

# Appendix C

## Calculation of General Peierls Hopping Phase

In this small section, we calculate the the hopping phase from one arbitrary lattice point to another arbitrary point,  $\vec{R}_{m_1, m_2} \rightarrow \vec{R}_{n_1, n_2}$ , in the Landau Gauge,  $\vec{A} = Bx\hat{y}$ .

$$t_{\mathbf{m}, \mathbf{n}} |\vec{R}_{\mathbf{n}}\rangle \langle \vec{R}_{\mathbf{m}}| \rightarrow e^{i\Theta_{\mathbf{m}, \mathbf{n}}} t_{\mathbf{m}, \mathbf{n}} |\vec{R}_{\mathbf{n}}\rangle \langle \vec{R}_{\mathbf{m}}|,$$

The Peierls phase[19] is calculated as follows,

$$\begin{aligned} \Theta_{m_1, m_2}^{n_1, n_2} &= -\frac{e}{\hbar} \int_{\vec{R}_{m_1, m_2}}^{\vec{R}_{n_1, n_2}} \vec{A} \cdot d\vec{\ell}, \\ &= -2\pi \frac{eB}{h} \int_{\vec{R}_{m_1, m_2}}^{\vec{R}_{n_1, n_2}} x\hat{y} \cdot d\vec{\ell}, \quad d\vec{\ell} = \hat{d}\ell \sqrt{d^2x + d^2y} = \hat{d}\ell dx \sqrt{1 + \left(\frac{dy}{dx}\right)^2}. \end{aligned}$$

We need to find the line equation or the classical path between the end points, since the end points are known, it is easily written as,

$$y - \vec{R}_{m_1, m_2} \cdot \hat{y} = \frac{\left(\vec{R}_{n_1, n_2} - \vec{R}_{m_1, m_2}\right) \cdot \hat{y}}{\left(\vec{R}_{n_1, n_2} - \vec{R}_{m_1, m_2}\right) \cdot \hat{x}} \left(x - \vec{R}_{m_1, m_2} \cdot \hat{x}\right). \quad (\text{C.1})$$

The unit vector along the integral path is  $\hat{d}\ell = \frac{\vec{R}_{n_1, n_2} - \vec{R}_{m_1, m_2}}{|\vec{R}_{n_1, n_2} - \vec{R}_{m_1, m_2}|}$ . Also, derivative of the line equation yields,

$$dy/dx = \frac{\left(\vec{R}_{n_1, n_2} - \vec{R}_{m_1, m_2}\right) \cdot \hat{y}}{\left(\vec{R}_{n_1, n_2} - \vec{R}_{m_1, m_2}\right) \cdot \hat{x}}$$

. Combining the expressions,

$$\begin{aligned} \Theta_{m_1, m_2}^{n_1, n_2} &= -2\pi \frac{eB}{h} \int_{\vec{R}_{m_1, m_2}}^{\vec{R}_{n_1, n_2}} x dx \sqrt{1 + \left(\frac{dy}{dx}\right)^2} \hat{y} \cdot \hat{d}\ell, \\ &= -2\pi \frac{eB}{h} \int_{\vec{R}_{m_1, m_2}}^{\vec{R}_{n_1, n_2}} x dx \sqrt{1 + \left(\frac{(\vec{R}_{n_1, n_2} - \vec{R}_{m_1, m_2}) \cdot \hat{y}}{(\vec{R}_{n_1, n_2} - \vec{R}_{m_1, m_2}) \cdot \hat{x}}\right)^2} \frac{(\vec{R}_{n_1, n_2} - \vec{R}_{m_1, m_2}) \cdot \hat{y}}{|\vec{R}_{n_1, n_2} - \vec{R}_{m_1, m_2}|}, \\ &= -2\pi \frac{eB}{h} \frac{(\vec{R}_{n_1, n_2} - \vec{R}_{m_1, m_2}) \cdot \hat{y}}{(\vec{R}_{n_1, n_2} - \vec{R}_{m_1, m_2}) \cdot \hat{x}} \frac{x^2}{2} \Big|_{\vec{R}_{m_1, m_2}}^{\vec{R}_{n_1, n_2}}, \\ &= -2\pi \frac{eB}{h} \left( [\vec{R}_{n_1, n_2} - \vec{R}_{m_1, m_2}] \cdot \hat{x} \right) \left( \frac{\vec{R}_{n_1, n_2} + \vec{R}_{m_1, m_2}}{2} \cdot \hat{y} \right). \end{aligned} \quad (\text{C.2})$$

Explicitly, the Bravais lattice vectors are,  $\vec{R}_{m_1, m_2} = \lambda_1 \left( m_1 + m_2 \frac{\lambda_2}{\lambda_1} \cos \theta, \frac{\lambda_2}{\lambda_1} \sin \theta \right)$ . For the eight neighbors, the Peierls phases are found,

$$\begin{aligned} \Theta_{m_1, m_2}^{m_1+1, m_2} &= -2\pi \phi (m_2 + 1/2) \\ \Theta_{m_1, m_2}^{m_1, m_2+1} &= -2\pi \phi \frac{\lambda_2}{\lambda_1} \cos \theta (m_2 + 1/2) \\ \Theta_{m_1, m_2}^{m_1-1, m_2+1} &= -2\pi \phi \left( -1 + \frac{\lambda_2}{\lambda_1} \cos \theta \right) (m_2 + 1/2) \\ \Theta_{m_1, m_2}^{m_1+1, m_2+1} &= -2\pi \phi \left( 1 + \frac{\lambda_2}{\lambda_1} \cos \theta \right) (m_2 + 1/2). \end{aligned} \quad (\text{C.3})$$

Parameter  $\phi$  is the magnetic flux within the smallest plaquette normalized by the magnetic flux quantum,  $\phi = \frac{B\lambda_1\lambda_2 \sin \theta}{h/e}$ . The area of the unit cell changes as a function of primitive lattice vectors and the angle between them.

# Appendix D

## N-Leg Ladder Packet Splitting After A Flux Quench

We consider a N leg ladder with the gauge choice,  $\vec{A}_{||}(\vec{x}) = B_0 y \hat{x}$ , the Hamiltonian is,

$$\hat{H}_{NL}^{||} = -J \sum_{m=-\infty}^{\infty} \left[ \sum_{r=0}^{n-1} (e^{-i2\pi\phi r} a_{m+1,r}^\dagger a_{m,r} + H.c) + \sum_{r=0}^{n-2} (a_{m,r+1}^\dagger a_{m,r} + H.c) \right] \quad (\text{D.1})$$

and the magnetic flux is  $\phi = a^2 B_0$ . Define the Fourier transform operators in the parallel direction,

$$\begin{aligned} a_{k,r}^\dagger &= \frac{1}{\sqrt{2\pi}} \sum_{m=-\infty}^{\infty} a_{m,r}^\dagger e^{-ikm}, \quad -\pi \leq k \leq \pi, \\ a_{m,r}^\dagger &= \int_{-\pi}^{\pi} \frac{dk}{\sqrt{2\pi}} a_{k,r}^\dagger e^{ikm}. \end{aligned} \quad (\text{D.2})$$

The operators,  $a_{m,r}^\dagger$  and  $a_{k,r}^\dagger$  are the algebraic creation operators of two reciprocal spaces,  $x - k$ . The Hamiltonian in Eq.D.1 in  $k$ -space is,

$$\hat{H}_{nL}^{||} = \int_{-\pi}^{\pi} dk \sum_{r_1, r_2=0}^{N-1} a_{k,r_1}^\dagger A_{r_1, r_2}(k) a_{k,r_2}, \quad (\text{D.3})$$

and the matrix elements are

$$A_{r_1, r_2}(k) = -J \begin{pmatrix} 2 \cos(2\pi\phi_0 - k) & 1 & 0 & \dots & 0 \\ 1 & 2 \cos(2\pi\phi_1 - k) & 1 & \dots & 0 \\ \vdots & \vdots & \vdots & \ddots & \vdots \\ 0 & 0 & 0 & \dots & 2 \cos(2\pi\phi(N-1) - k) \end{pmatrix}_{N \times N}$$

. In the diagonal basis,

$$a_{k,r} = \sum_{s=0}^{N-1} U_{r,s}(k) b_{k,s}, \quad (\text{D.4})$$

$$b_{k,r} = \sum_{s=0}^{N-1} U_{s,r}^*(k) a_{k,s}, \quad (\text{D.5})$$

$$(\text{D.6})$$

where  $U^\dagger U = I$ , the matrix  $A_{r_1, r_2}(k)$  is diagonalized as  $\sum_{r_1, r_2} U_{n_1, r_2}^*(k) A_{r_1, r_2}(k) U_{r_2, n}(k) = \varepsilon_{n_1}(k) \delta_{n_1, n}$ . The Hamiltonian in the parallel gauge is,

$$\hat{H}_{nL}^{\parallel} = -J \int_{-\pi}^{\pi} dk \sum_{n=0}^{N-1} \varepsilon_n(k) b_{k,n}^\dagger b_{k,n}. \quad (\text{D.7})$$

The only necessary condition for the initial state is to be an eigenstate of the discrete translation operator under zero field,

$$|\psi_{k_0}(0)\rangle = \sum_{r=0}^{N-1} \psi_r(k_0) a_{k_0, r}^\dagger |vac.\rangle. \quad (\text{D.8})$$

The coefficients  $\psi_r(k_0)$  are chosen arbitrarily ensuring the normalization. Using Eq.D.4, the initial is expanded in the new basis with magnetic flux  $\phi$ ,

$$|\psi_{k_0}(0)\rangle = \sum_{n=0}^{N-1} \left( \sum_{r=0}^{N-1} U_{n,r}^*(k_0) \psi_r(k_0) \right) b_{k_0, n}^\dagger |vac.\rangle = \sum_{n=0}^{N-1} W_n(k_0) b_{k_0, n}^\dagger |vac.\rangle. \quad (\text{D.9})$$

Note that  $W_n(k_0)$  can also be written as  $W_n(k_0) = \langle k, n; \phi | \psi_{k_0}(0) \rangle$ , where  $|k, n; \phi\rangle = b_{k_0, n}^\dagger |vac.\rangle$ . The time evolved form of this arbitrary wavefunction is,

$$|\psi_{k_0}^{\parallel}(t)\rangle = e^{-i\frac{t}{\hbar} \hat{H}_{nL}^{\parallel}} \sum_{n=0}^{N-1} W_n(k_0) b_{n, k_0}^\dagger |vac.\rangle, \quad (\text{D.10})$$

$$= \sum_{n=0}^{N-1} W_n(k_0) e^{i\frac{Jt}{\hbar} \varepsilon_n(k_0)} b_{n, k_0}^\dagger |vac.\rangle. \quad (\text{D.11})$$

Hence, an arbitrary wavefunction at lattice momentum  $k_0$  **splits into  $N$  packets** when it is quenched to  $\hat{H}_{NL}^{\parallel}$ , where each packet  $n$  has weight  $|W_n(k_0)|^2$ .

We can opt for a set of another gauge potentials leading the same physical situation for a static system. This gauge choice, the perpendicular gauge is  $\vec{A}_{\perp}(\vec{r}) = -B_0 x \hat{y}$ . The two vector potentials are related by a gauge transformation as follows,

$$\vec{A}_{\perp}(\vec{x}) = \vec{A}_{\parallel}(\vec{x}) - \vec{\nabla}\Lambda(\vec{x}), \quad \Lambda(\vec{x}) = B_0 xy = \phi mr, \quad (\text{D.12})$$

therefore, the equivalent lattice version is

$$U = e^{i2\pi\phi \sum_{m,r} mra_{m,r}^{\dagger} a_{m,r}}, \quad U^{\dagger}U = I. \quad (\text{D.13})$$

The corresponding form of  $H_{NL}^{\parallel}$  in the perpendicular static gauge is,

$$\begin{aligned} H_{NL}^{\perp} &= UH_{NL}^{\parallel}U^{\dagger}, \\ &= -J \sum_{m=-\infty}^{\infty} \left[ \sum_{r=0}^{n-1} (a_{m+1,r}^{\dagger} a_{m,r} + H.c.) + \sum_{r=0}^{n-2} (e^{i2\pi\phi m} a_{m,r+1}^{\dagger} a_{m,r} + H.c.) \right]. \end{aligned}$$

The same initial wavefunction in Eq.D.8 is time evolved with  $\hat{H}_{NL}^{\perp}$  as follows,

$$\begin{aligned} |\psi_{k_0}^{\perp}(t)\rangle &= e^{-i\frac{t}{\hbar}\hat{H}_{NL}^{\perp}}|\psi_{k_0}(0)\rangle, \\ &= Ue^{-i\frac{t}{\hbar}H_{NL}^{\parallel}}U^{\dagger}|\psi_{k_0}(0)\rangle. \end{aligned} \quad (\text{D.14})$$

The  $U$  term on the left most in Eq.D.14 does not modify the density, it only modifies the phase on each lattice site and it is cancelled in observables. Moreover, the resulting number of packets is  $N$  fold times the number of quasi-momentum states for  $U^{\dagger}|\psi_{k_0}(0)\rangle$ . Keep in mind that, the same explanation works for the parallel gauge case as in Eq.D.10. However, notice that  $U^{\dagger}|\psi_{k_0}(0)\rangle$  is not restricted

by a single quasi-momentum state. Analysing and expanding the term  $U^\dagger|\psi_{k_0}(0)\rangle$ ,

$$\begin{aligned}
U^\dagger|\psi_{k_0}(0)\rangle &= e^{-i2\pi\phi\sum_{m,r}mra_{m,r}^\dagger a_{m,r}} \sum_{r'=0}^{N-1} \psi_{r'}(k_0) a_{k_0,r'}^\dagger |vac.\rangle, \\
&= e^{-i2\pi\phi\sum_{m,r}mra_{m,r}^\dagger a_{m,r}} \sum_{r'=0}^{N-1} \sum_{m'=-\infty}^{\infty} \psi_{r'}(k_0) e^{-ik_0m'} a_{m',r'}^\dagger |vac.\rangle, \\
&= \sum_{r=0}^{N-1} \sum_{m'=-\infty}^{\infty} \psi_r(k_0) e^{-ik_0m'} e^{-i2\pi\phi m' r} a_{m',r}^\dagger |vac.\rangle, \\
&= \sum_{r=0}^{N-1} \psi_r(k_0) a_{k_0+2\pi\phi r,r}^\dagger |vac.\rangle. \tag{D.15}
\end{aligned}$$

We can expand each  $a_{k,r}^\dagger$  operator in  $b_{k,r}^\dagger$  basis using Eq.D.4 as,

$$\begin{aligned}
U^\dagger|\psi_{k_0}(0)\rangle &= \sum_{r=0}^{N-1} \psi_r(k_0) \left( \sum_{s=0}^{N-1} U_{s,r}^*(k_0 + 2\pi\phi r) b_{k_0+2\pi\phi r,s}^\dagger \right) |vac.\rangle, \\
&= \sum_{r=0}^{N-1} \sum_{s=0}^{N-1} c_{r,s}(k_0 + 2\pi\phi r) b_{k_0+2\pi\phi r,s}^\dagger |vac.\rangle, \tag{D.16}
\end{aligned}$$

and  $c_{r,s}(k) = \psi_r(k) U_{s,r}^*(k)$ .

Therefore, after the time evolution  $e^{-i\frac{t}{\hbar}H_{NL}^\dagger}$ , there are **at most**  $N^2$  packets with the probability  $|c_{r,s}(k)|^2$  and the corresponding velocity  $v_{s,r} = \left. \frac{\partial \varepsilon_s(k)}{\partial k} \right|_{k_0+2\pi\phi r}$  for each band  $s$  and the quasi-momentum  $k_0 + 2\pi\phi r$ . The only other restriction for the  $N$ -leg ladder quench scenario other than  $N^2$  post-quench packets is the natural limit for the total number of bands,  $Nq$ . For some cases,  $N^2 > Nq$ , and therefore even if the gauge transformation allows for  $N^2$  packets, the maximum number is limited by  $Nq$ .